[redacted]

NATIONAL AERONAUTICS AND SPACE ADMINISTRATION
CONTRACT NO. NAS 7-100

Space Programs Summary No. 37-16, Volume II

for the period May 1, 1962 to July 1, 1962

The Planetary — Interplanetary Program

[redacted]

Copy No. 00390

JET PROPULSION LABORATORY
CALIFORNIA INSTITUTE OF TECHNOLOGY
PASADENA, CALIFORNIA

July 31, 1962

[redacted]

Preface

The *Space Programs Summary* is a bimonthly publication designed to report on JPL space exploration programs and related supporting research and advanced development projects conducted under the sponsorship of the National Aeronautics and Space Administration.

Beginning with this issue the *Space Programs Summary* is divided into six volumes. All information formerly documented in the JPL *Research Summary*, together with reports on advanced development projects, will in the future be reported in Volumes IV and V of the *Space Programs Summary*. The subtitles of all volumes of the reorganized *Space Programs Summary* are:

Vol. I, The Lunar Program (Confidential)
Vol. II, The Planetary-Interplanetary Program (Confidential)
Vol. III, The Deep Space Instrumentation Facility (Unclassified)
Vol. IV, Supporting Research and Advanced Development (Unclassified)
Vol. V, Supporting Research and Advanced Development (Confidential)
Vol. VI, Space Exploration Programs and Space Sciences (Unclassified)

The new *Space Programs Summary*, Volume VI is an unclassified digest of appropriate material from Volumes I through V, plus the reports of the JPL Space Sciences Division.

W. H. Pickering, *Director*
Jet Propulsion Laboratory

This document contains information affecting the national defense of the United States, within the meaning of the Espionage Laws, Title 18, U.S.C., Sections 793 and 794, the transmission or revelation of which in any manner to an unauthorized person is prohibited by law.

Space Programs Summary No. 37-16

Volume II

Copyright © 1962
Jet Propulsion Laboratory
California Institute of Technology

Contents

I. Program Objectives 1

II. *Mariner* R Project 3

A. Systems Test and Operations 3
B. Spacecraft Design 8
C. Guidance and Control 10
D. Telecommunications 17
E. Space Sciences 18
F. Propulsion 19
G. Supporting Activities 20

III. *Mariner* B Project 23

A. Systems Operations 23
B. Spacecraft Design 31
C. Guidance and Control 40
D. Telecommunications 66
E. Space Sciences 67
F. Propulsion 87
G. Supporting Activities 90

IV. *Voyager* Project 93

I. Program Objectives

The primary long-range objective of the NASA Planetary–Interplanetary Program is the development of automatic, unmanned, interplanetary spacecraft technology and the use of this technology in the form of space probes to gather fundamental scientific knowledge concerning the planetary and interplanetary environments, the planets themselves, and solar phenomena, both out of and within the plane of the ecliptic.

The secondary long-range objective of the program is the development of technology and the collection of scientific data which will contribute to the successful manned exploration of the planets and interplanetary space.

The primary objective of the program by 1970 is to have rather completely demonstrated and, to some reasonable extent, exploited (in terms of acquired scientific data) spacecraft capable of (1) being put into orbit around and (2) landing on the surface of Mars and Venus.

A secondary objective during this period will be the initial effort toward extending the above capability toward the planets Mercury and Jupiter and space shots out of the plane of the ecliptic and in toward the Sun. The immediate objective of the program is the initial probing of Mars and Venus.

The Planetary–Interplanetary Program at present consists of three projects: *Mariner* R using the *Atlas–Agena* B vehicle, *Mariner* B using the *Atlas–Centaur* vehicle, and the *Voyager*, using the *Saturn* vehicle. The missions planned for these projects are obviously subject to change because of such influences as new scientific discoveries or unexpected developments in vehicle availabilities.

II. *Mariner* R Project

Mariner R-1 and -2 spacecraft completed the series of system and environmental tests scheduled to be performed at JPL. The set of spare spacecraft components was assembled and is now referred to as *Mariner* R-3. It is not, however, the intent to fly MR-3 unless necessary, but it will be cannibalized for spares whenever required. It is expected that after MR-1 and MR-2 are flown MR-3 will be subjected to an extended life test.

All three of the spacecraft plus the GSE were shipped from JPL to AMR on schedule at the end of May. Since arrival at Cape Canaveral, MR-1 and MR-2 have been undergoing pre-launch tests. MR-3 has completed subsystem and system tests.

Agena B, Serial Nos. 6901 and 6902 and *Atlas* D Serial Nos. 145 and 179 are at AMR and are in pre-launch testing. The scheduled delivery of the *Atlas* to AMR was in jeopardy for a few days due to the grounding of all USAF C-133's. Expeditious action on the part of the USAF resolved this in time, however, to keep the *Mariner* R operation on schedule. As of the close of this report period, all phases of the *Mariner* R operations are proceeding on schedule and no presently known or foreseen problems should affect the meeting of the first launch date.

A. Systems Test and Operations

1. Trajectory Analysis

a. Constraints. In order to choose the aiming point for the *Mariner* R mid-course maneuver, it is necessary to consider a number of constraints at the target. These constraints are imposed by the radiometer, magnetometer, and Earth sensor considerations and by the fact that probability of impact shall be less than 0.001. Specifically, these constraints are as follows:

(1) When the spacecraft passes through the terminator plane, the planet must subtend an angle between 10 and 45 deg; thus the radius should lie between 70,866 and 16,210 km, respectively (magnetometer and radiometer considerations).

(2) The angles measured at the spacecraft from the Earth–probe–Sun plane, normal to the probe–Sun direction, to both edges of Venus must not exceed 55 deg (radiometer scan considerations).

(3) The trajectory must be chosen in such a way that for all normally expected dispersions, the angular separation between the near limb of Venus and the

Sun is greater than 0 deg for the period of time that experiments are being performed at Venus.

(4) The angle between the Earth–probe–near limb of Venus must remain greater than (approximately) 60 deg until the radiometer scan goes off the planet (Earth sensor considerations). Actually this constraint is quite complicated, for the Earth sensor will lose the Earth for different values of the Earth–probe–near limb of Venus angles when the light intensity of Venus as seen from the spacecraft is altered. The 60-deg angle, however, is a good approximation of the constraint for most aiming points.

(5) The probability of the probe impacting the planet should remain less than one part in a thousand. This implies that the nominal aiming point measured from the center of Venus should be approximately 30,000 km, or greater.

b. Definition of the frame of reference. The target parameter **B** can be described by specifying its components. Let **S** be a unit vector in the direction of the incoming asymptote. Let **V** be a unit vector from Venus in the direction of the north pole of the ecliptic. Then

$$\mathbf{T} = \frac{\mathbf{S} \times \mathbf{V}}{\| \mathbf{S} \times \mathbf{V} \|}$$

Let **R** be a unit vector forming a right-hand system with **S**; i.e., $\mathbf{R} = \mathbf{S} \times \mathbf{T}$. Then **B** has two miss components: $\mathbf{B} \cdot \mathbf{T}$ and $\mathbf{B} \cdot \mathbf{R}$.

c. Aiming zones. Analysis of plots such as Figs. 1 and 2 for the entire *Mariner* R firing period reveals that the aiming zones do not change radically for *Mariner* R. Figures 1 and 2 represent constraints for the *Mariner* R encounter sequence for the first and last launch dates, respectively. It is to be noted that the curves lie in the *RT* plane of the trihedral defined in ***b*** above. Due to magnetometer and radiometer considerations the spacecraft must lie within the two areas bounded by $AD = 10$ deg and $AD = 45$ deg. Because of radiometer scan requirements aiming points must lie within the contour labeled $EV = 55$ deg. All aiming points outside the contour labeled $SPV = 0$ deg (Sun eclipsed before closest approach) satisfy the condition that the angular separation between the near limb of Venus and the Sun be greater than 0 deg for the period of interest.

The contour labeled $*EPV = 60$ deg represents (approximately) the constraint imposed by requiring that the Earth–probe–near limb of Venus angle be approxi-

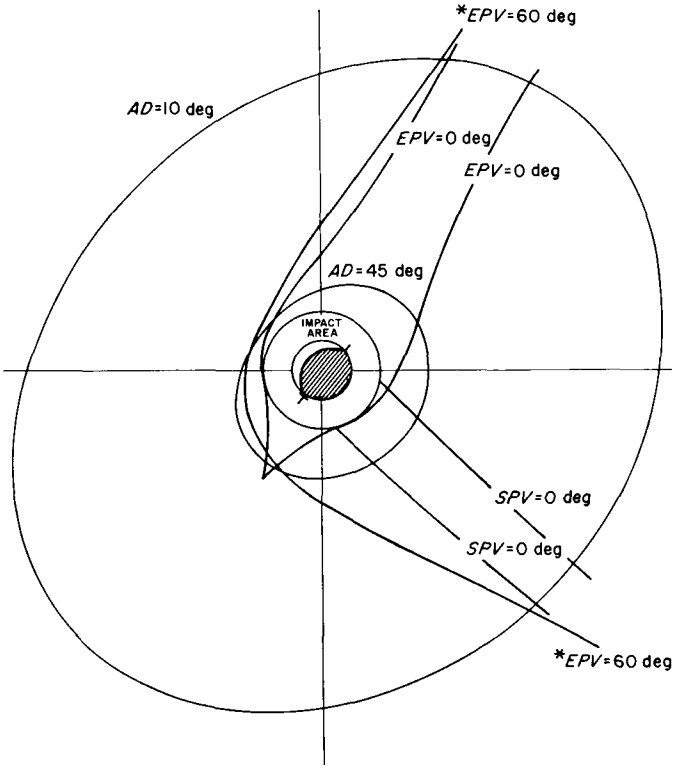

Fig. 1. Constraints for encounter sequence for first launch date

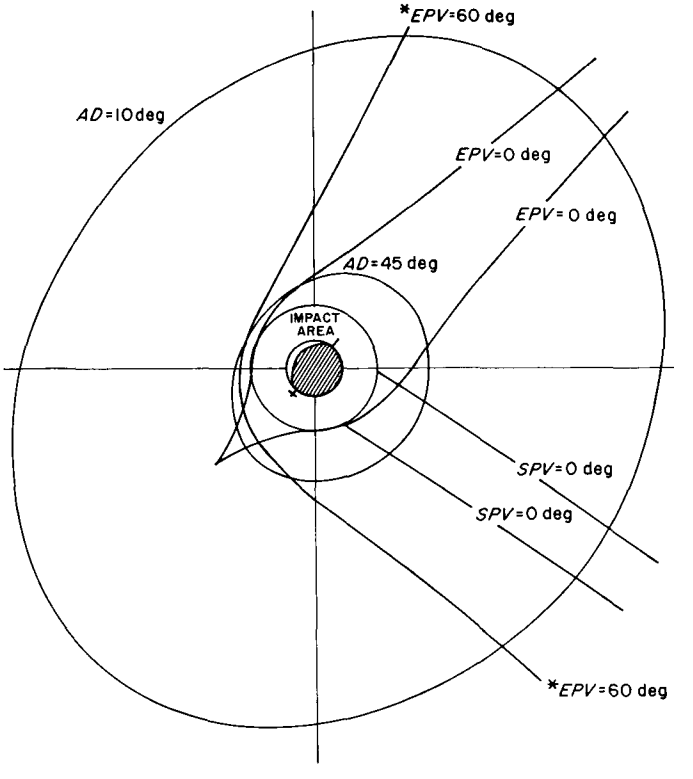

Fig. 2. Constraints for encounter sequence for second launch date

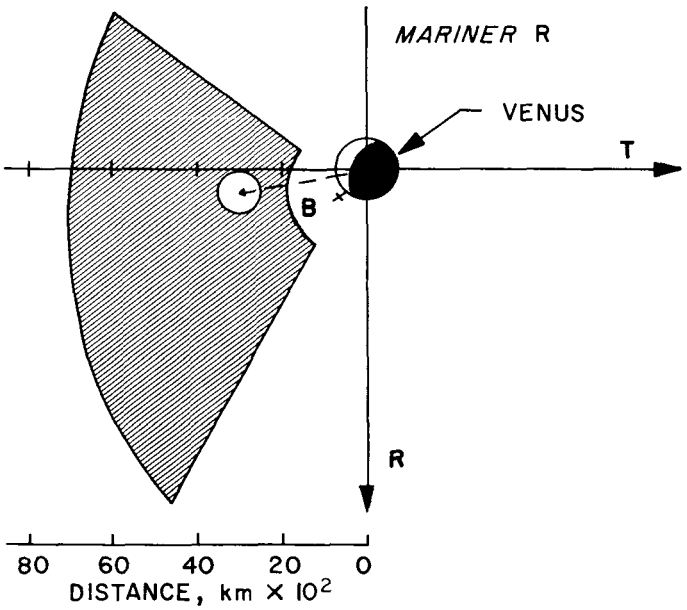

Fig. 3. Permissible aiming zone region

mately 60 deg until the radiometer scan goes off the planet. The contour $EPV = 0$ deg indicates the contour within which aiming points will occult the Earth after closest approach.

d. Resultant aiming zones. After eliminating those areas suppressed by the above considerations, one is left with the area indicated in Fig. 3. The frame of reference is again *RT*. The circle inside the shaded area represents the approximate 1-σ dispersion circle after mid-course maneuver and the center of the circle is the nominal aiming point. The vector **B** to this point has miss components $\mathbf{B}\cdot\mathbf{T} = -29545$ km, and $\mathbf{B}\cdot\mathbf{R} = 5210$ km.

2. Systems Test Operations

Since the last reporting period, the MR-1 and -2 were scheduled for testing of weight, cg determination, magnetometer mapping, and mechanical preparation for the dummy run and joint closed loop operations test. The dummy run was conducted to check out the JPL blockhouse and launch control equipment when operating with the spacecraft. Also, the countdown procedure was verified and operations personnel were trained in the use of launch complex type equipment, i.e., umbilical junction box, cables, plug, and receptacle. The dummy run was performed with shorter cables than are required at AMR, in lieu of using the umbilical plug and receptacle, since the operation is conducted without an *Agena–Mariner* R adapter. Both spacecraft performed successfully. Preshipment tests were conducted on both spacecraft. All outstanding ECR's were incorporated. The temperature-control paint patterns were completed. The final inspection was performed with microscopes to view the cable connections and electronic modules. All system test deficiencies were repaired or replaced. The spacecraft were then reassembled and wiring ground loop checks were performed. Final button-up procedure was used to have the spacecraft ready for launch if the test showed no discrepancies.

The flight spares were assembled as spacecraft MR-3, complete except for an attitude-control gas system, IR radiometer, and CC&S. There were other spares which were packaged individually and shipped. When time permits, MR-3 will be checked out electrically and placed in an operating condition to obtain as much time as possible on final flight configuration. This is deemed advisable since MR-1 and MR-2 testing has forced incorporation of more than 100 ECR's since delivery to SAF.

a. AMR operations summary. All spacecraft and GSE arrived safely June 4 at AMR. Unloading and inspection revealed that the ion chamber SN3 was damaged, and that the microwave antenna SN1 feed was broken. The System Test Complex (STC) installation was completed on June 5. No other damage was discovered. See Fig. 4 for schedule.

MR-1. On June 5 the STC installation was completed. The spacecraft was installed on the systems test fixture and the mid-course motor was removed for weight, cg determination, and pressurization. CC&S Module 5A8 capacitors were changed. The microwave radiometer was X-rayed to determine if there were breaks in the waveguide. The flight gyros were calibrated and released for installation on the spacecraft. The IR radiometer was received at AMR. The mid-course motor and flight gyros were installed. Spacecraft power was applied and all subsystems made preliminary checks. The solar plasma experiment SN2 did not function properly and a replacement (SN4) was installed which gave proper indication. Solar plasma experiment SN2 was reported to have a defective transistor. All other equipment checked out normally. Radiometer SN4, which showed no evidence of waveguide mechanical separation, was installed.

System Test No. 1 proceeded without difficulty until the "end of mid-course motor burn" signal, which did not occur. The sequence was repeated and failed again. Investigation proved that the CC&S GSE electromechanical counter had been connected for this test and was feeding into the entire spacecraft, causing the abnormalities.

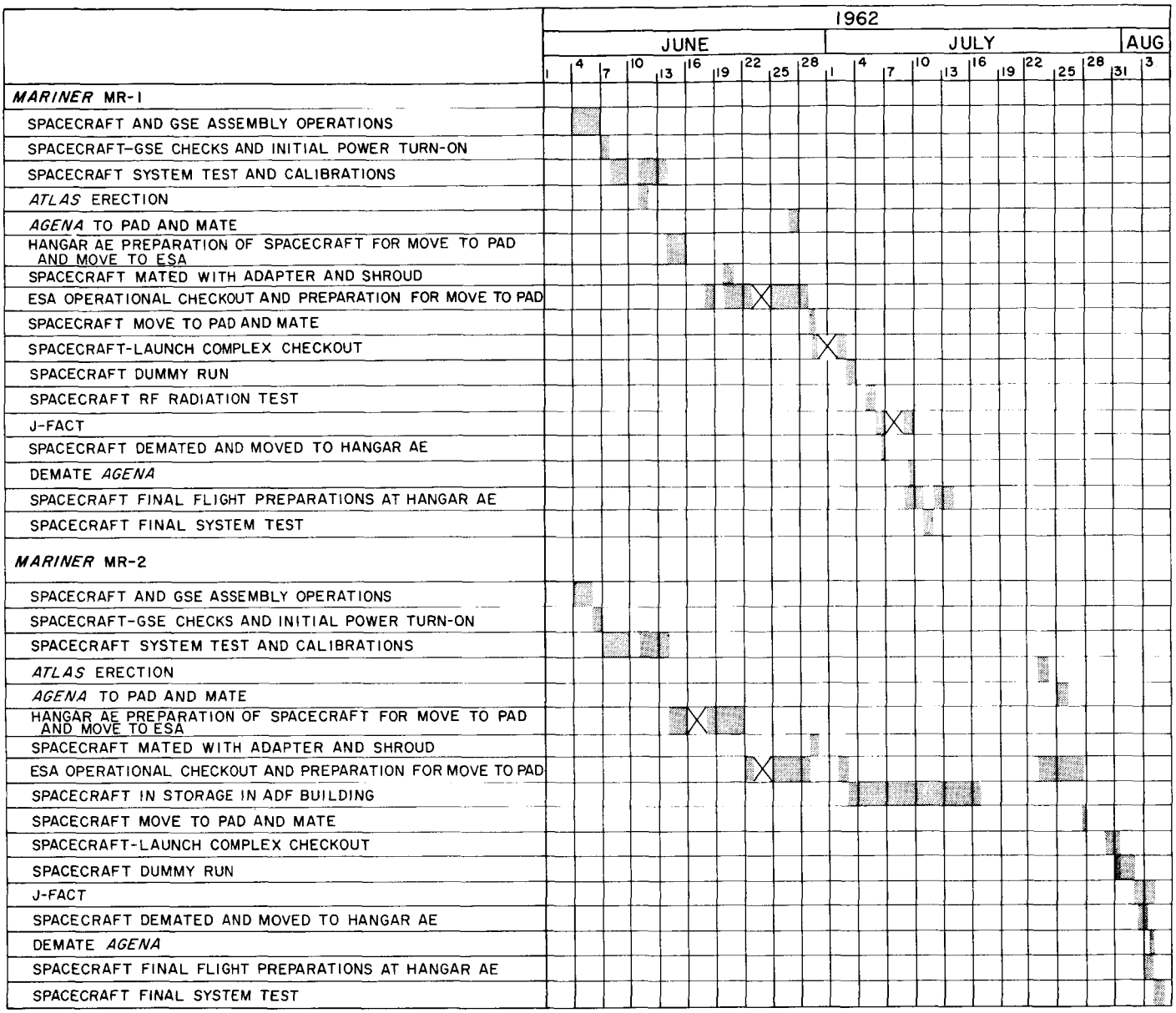

Fig. 4. Spacecraft launch base operation schedules

System Test No. 2 disclosed an improper CC&S GSE indication, which was corrected. An out-of-tolerance indication was noted in the encounter sequence, which was traced to a relay contact failure in the gyro module. A replacement corrected the failure.

System Test No. 3 revealed minor discrepancies in the radiometer calibrate sequences and the particle flux detector.

MR-2. After completing unloading operations, the capacitor change in CC&S Module 5A8 was accomplished, and ion chamber SN3 was replaced with SN2. Spacecraft power was applied to all systems, except for the microwave radiometer. Telemetry calibrations were good. The telemetry communications data loop was checked out to JPL satisfactorily. The spacecraft was removed from the test fixture and the new attitude-control gas system was installed and wired. The solar panels were assembled, cleaned, and reworked. Spacecraft was ready for compatibility checks. All attitude-control valves were checked for magnetic field strength interference with the magnetometer and were found acceptable. The flight solar panels were checked out satisfactorily with the space-

craft. The battery current and voltage telemetry channels were recalibrated and showed no change from previous calibrations. SN3 particle flux experiment was installed, and the low count rate seen on MR-1 was verified. The Explosive Safe Area test setup and dummy run trailer were checked out and ready for spacecraft. The blockhouse equipment was cabled and each rack checked out. The entire complex was checked out June 18.

3. Space Flight Operations

Space flight operational preparations for the *Mariner* R missions are continuing. A Joint Closed Loop Operations Test (J-CLOT) was conducted on May 10, 1962 using MR-1 as the test vehicle. The participants included the Spacecraft Assembly Facility (SAF), Space Flight Operations Center (SFOC), Spacecraft Data Analysis Team (SDAT), Scientific Analysis Group (SAG), Mid-course Command Group (MCG), Central Computing Facility (CCF), and the DSIF. The following problems were encountered during the J-CLOT:

(1) Delayed data processing and spacecraft performance analysis, due to unidentifiable data blocks and incomplete computer programs.

(2) Inaccurate pulse outputs from the time code generator and incorrect time coding on the data program tape used.

(3) Periodic loss of sync between the PDP-1 and teletype transmitter.

(4) Command message format errors.

The subsequent critiques indicated that:

(1) More training is required within the SDAT in identifying out-of-sync data, particularly since this problem may be expected to occur during the mission.

(2) It is advisable to have a complete telemetry data processing program available for this type of test.

(3) Synchronization of all timing devices is necessary.

(4) More extensive communications interface and equipment should be employed.

Spacecraft response during this test was not normal for an actual flight, due to the limitations of simulating space environment and the controlled spacecraft stimuli. However, since the purpose of the test was to establish initial compatibility between the SFO Complex and the spacecraft and to familiarize operations personnel with their duties, the test was a qualified success.

The Space Flight Operations Planning Document (SFOP) was released May 1, 1962 and the first revision published on June 18, 1962. Section VI, a detailed nonstandard sequence of events, will be included in the second revision, which is scheduled for completion by July 9, 1962.

Installation and checkout of audio and video equipment in the SFO Center is proceeding as planned. Completion of the facility modifications is anticipated by July 15, 1962. A digital time display system for the facility has been ordered and delivery is expected in time for the operations.

The spacecraft is currently undergoing extensive testing at AMR and the data are being received via TTY, processed by CCF, and analyzed by operations groups as a parallel effort to the spacecraft checkout teams. Preliminary personnel assignations and coverage requirements for the mission have been established. Two system integration tests are scheduled; one for July 16, 1962 and one for July 19, 1962, permitting evaluation of the completed operations system and allowing a suitable time frame in which any minor modifications may be made.

4. Launch Facility Improvements

The original launch control GSE (LC GSE) installation at AMR Pad 12 was based on the immediate and foreseeable requirements of the *Ranger* Project. Since then, several limitations have become evident and a noninterference improvement program has been started. To date, replacement of one catenary, tower, and pad cable has been completed to minimize voltage drop in critical power lines.

The tower J-box for *Rangers* 6 through 9 is being updated to allow all signals through the umbilical to be monitored by routing all catenary cables through the box. The box is also designed to minimize the effects of moisture and fungus and to allow circuit changes or complete wiring revisions with a minimum of rework.

To accommodate the needs of *Mariner* R, a hard-line conduit installation of 400-cps power has been added with outlets at the launch control shelter and at the top of the umbilical tower with control at the blockhouse. The generators are mobile units which could be made available for other applications when not required at the pad. A video pair installation to the top of the umbilical tower has been completed to allow direct connection from the output of critical signal conditioning modules via video pair to any required location served by the AMR communications installation.

Planned changes (on a noninterference basis) include: (1) replacement of one catenary cable with low capacity (temperature-stable type), (2) eventual elimination or enclosure of the presently exposed signal cable interface at the bottom of the umbilical tower, and (3) redesign of the blockhouse GSE area J-boxes to allow permanent connection of the hard lines.

Addition of a dummy run trailer for installation of launch control GSE at JPL is planned for RA-6 and others. The use of the trailer will minimize setup time and allow more flexibility to accommodate test location changes. Improved control and storage of the LC GSE between tests will also be possible.

A similar trailer will be available at the explosive safe area at AMR to allow tests in that area starting with *Ranger* 5.

B. Spacecraft Design

The principal activity during the report period was the transferring of the total *Mariner* R operation to AMR. This included final spacecraft cleanup and preparation for shipment. New shipping containers and shipping philosophies were tried and proven effective. A 10% increase in solar panel area was effected by bolting a new tip onto the existing panel.

1. Spacecraft Development

To satisfy the requirement for the increase in solar panel area, several approaches were investigated. A fixed panel on some sunlit portion of the spacecraft was rejected because of the difficulty of holding the cell temperatures within required bounds. A small articulated panel was rejected because all potential locations were plagued with interferences. Short bolt-on extensions to the tips of the existing panels were considered, but command antenna pattern disruption was feared.

The final choice was a single bolt-on extension to the solar panel without the antennas. The same structure as the main panel was used, to keep the physical and temperature characteristics of the panel tip the same as those of the basic panel already designed. By using the same width, the dense cell layout and cell wiring technique of the main panel were maintained. The Sun sensor, normally mounted on the panel corner, was moved to a new bracket on the extension, thus preserving its wide field of view.

The panel extension weighs 4.75 lb and is attached to a prototype panel (Figs. 5, 6). Extensive vibration tests have verified the adequacy of the panel and extension. Some minor reinforcement of the superstructure and the omnidirectional antenna was required as a consequence of the higher vibration levels caused by the panel extension.

A consequence of the single panel extension approach was that the unbalance in solar pressure on the spacecraft, acting for the entire flight, would use an excessive quantity of attitude-control gas. To balance the solar pressure without upsetting the command antenna pattern, an RF-

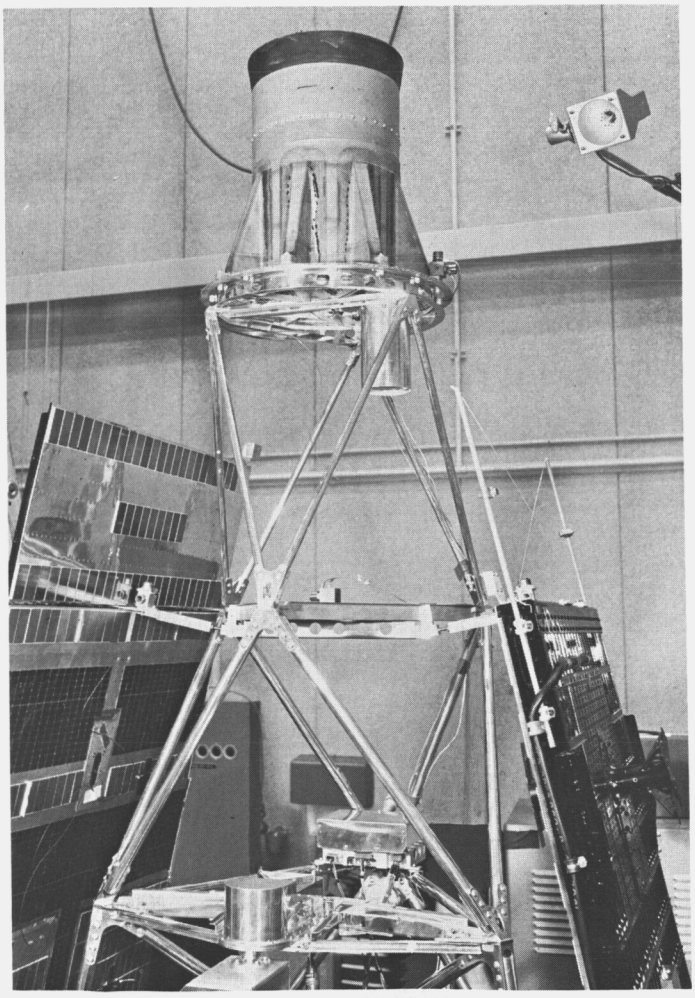

Fig. 5. Solar panel extension, front view

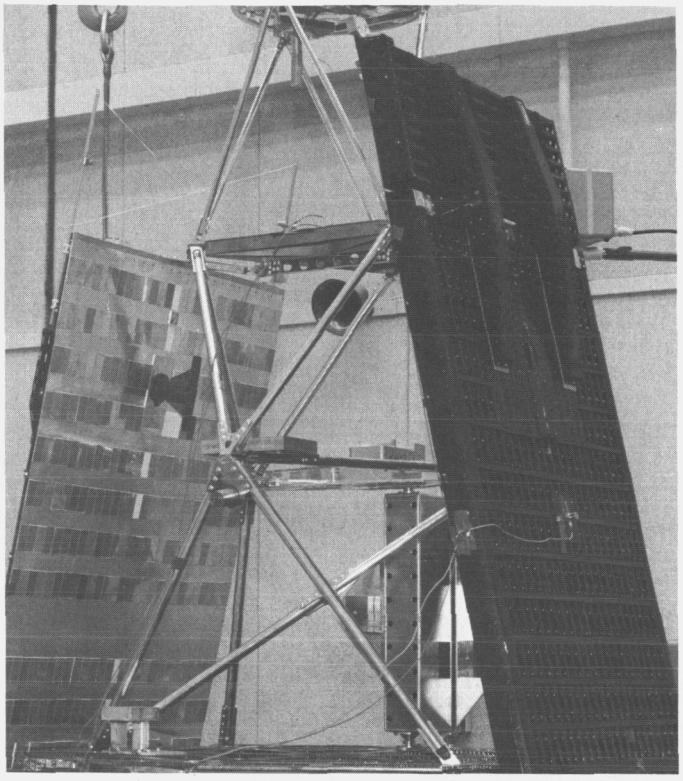

Fig. 6. Solar panel extension, back view

Fig. 8. Spacecraft mounted in transport van

Fig. 7. Solar sail fabrication

transparent solar sail was designed and fabricated. The sail has approximately the same area as the solar panel extension and is made of a silicone-rubber-impregnated Dacron cloth, supported by fiberglass rods. The sail weighs 0.2 lb complete with mounting brackets (Fig. 7).

2. Ground Handling Equipment

The shipment to AMR of the spacecraft and associated equipment demonstrated some simple approaches to the problem. Instead of shipping the spacecraft as disassembled units in many containers, all three spacecraft were shipped fully assembled, using the structure as a shipping container. The entire spacecraft, except solar panels, was hard-mounted to an electronics transport van to take advantage of its weight and soft springs. Previous tests had shown that the spacecraft experienced a much safer ride in this fashion than it would on the boost vehicle. The spacecraft mounted in a van is shown in Fig. 8. The solar panels were shipped in their specially designed, mobile containers as shown in Fig. 9.

To protect the spacecraft from the elements, sealed bags were used. These are fabricated from nylon net reinforced plastic with plastic zippers around the edges. Tape was used over the zippers to assure a hermetic seal. A light protective framework keeps the plastic bag from touching the spacecraft. A spacecraft inside a bag is shown in Fig. 10. The spacecraft in Fig. 8 is also inside one of these bags. Fig. 11 shows a solar panel on its support stand enclosed in a similar bag.

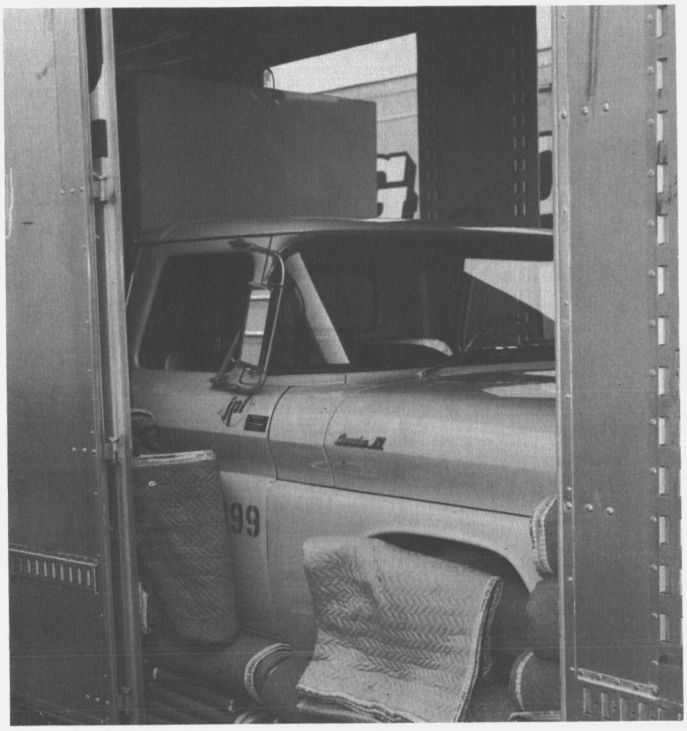

Fig. 9. Solar panel shipping container

Fig. 11. Solar panel in shipping bag

Fig. 10. Spacecraft in shipping bag

C. Guidance and Control

1. Spacecraft Power Subsystem

Both *Mariner* spacecraft have completed system testing at JPL. The flight unit and the spares have been defined and shipped to AMR. Both spacecraft have completed all testing there prior to the first move to the launching pad. All system tests at AMR have been conducted with no malfunction in the power subsystem.

a. Solar cell panels. The power deficiency reported in *SPS 37-15* has been corrected and six flight panels have been delivered to AMR. The area of the solar array was increased to permit the addition of 918 solar cells. This increased the total number of 1×2 cm cells from 9,792 to 10,710 (approximately 9%), thereby increasing the solar panel capability by 15 w at the maximum power point and 12 w at the battery sharing point. In addition, the series connected blocking diodes housed in the power switch and logic module were removed, eliminating a load of approximately 5 w. Modifications in the battery charging profile and a radio command capability over the cruise science electrical load are other provisions which ensure adequate margin for the power system to shift out of the sharing mode during the cruise periods.

b. Electrical converters. Life testing of the *Mariner* R power supply has been initiated. All the prototype modules are being utilized and have successfully completed 1500 hr of cruise mode operation.

Two power switch and logic modules are presently being constructed with a redesigned booster oscillator circuit in order to reduce power dissipation by approximately 3 w. The units will be flight-acceptance tested and delivered to AMR by July 15. The units will be used for MR-2 if data received from MR-1 indicates that a power shortage exists.

An engineering change request has been introduced into the spacecraft to correct for abnormal telemetry data of the battery current drain. The malfunction was traced to resistance variation of the contacts of the power transfer switch after switching to internal power. The change introduced causes the current transducer measurement to be independent of the switch contact resistance. In addition, the measuring range of the transducer was reduced from 20 to 10 amp, full scale, to increase the accuracy.

The malfunction witnessed during the operation of the 400-cps three-phase supply on MR-1 when the spacecraft was subjected to environmental tests was repeated on MR-1 during system test at AMR. The problem was originally attributed to an undetermined failure of the 400-cps three-phase module (*SPS 37-15*). Analysis of the data and tests has indicated that the malfunction must have been caused by an unknown load. When the malfunction reappeared at AMR, the problem was traced to a faulty relay in the gyro package which caused excessive loading of the single-phase output by the gyros.

c. Battery. The battery design (type approval) testing program described in *SPS 37-14* is continuing. The status of the three battery/charger systems being tested is as follows:

TA 1 (50°F) has completed the full test cycle. During the discharge period conducted at the end of 158 days of simulated flight the battery was able to deliver the required 40 w for 18 hr. However, when a pulse load of 160 w (peak value) was applied during this test in addition to the 40-w average, the battery terminal voltage was 0.5 v below the required minimum.

Cell voltage data indicated that one cell was responsible for approximately 60% of this decrease with the balance distributable among the other cells. A complete evaluation of this voltage condition will require disassembly and examination of all cell components. At the present time this battery (TA 1) is being subjected to an extended period of float charging beyond the original test period of 158 days in order to determine the limiting battery characteristics under this condition.

TA 2 (100°F) battery failed during the 10th week of testing. Disassembly and examination of the battery disclosed the following:

(1) All intercell walls broken.

(2) Epoxy seal on four cells broken.

(3) Outside wall of six cells broken.

(4) Two cells shorted.

(5) Seven cells contained positive electrodes with broken lead wires.

The broken seals and cell walls are the result of high cell pressures created by internal shorts. The cell shorts can result from a penetration of the separator system or a bypassing of the separator system by the formation of a zinc tree around the separators. A new potting procedure within the cell should prevent the latter type of failure in the flight batteries. The broken positive lead wires can be the result of a number of sequences. The basic step appears to be the weakening of the silver wire by oxidation. Vibration or shock could easily break those weakened leads. Movement of the cell pack due to the pressure can produce a shift capable of breaking the lead wires. A flexible epoxy coating is applied to the silver lead wires to prevent oxidation. Since broken wires previously examined appear to have parted in the interface area of the wire and the edge of the epoxy coating, this coating has been extended to include the plate area adjacent to the point where the silver lead wire joins the plate.

TA 3 (80°F) has completed 4 months of simulated flight and the data obtained to date indicates satisfactory performance. Approximately 2 weeks of the test schedule remains.

2. Gas Actuator Development

a. Gas system status. Three gas system assemblies for attitude control are being fabricated, and the fourth and last system is in process.

Before shipping the spacecraft to AMR, a 48-hr quantitative leak test was conducted on each gas system at the SAF. Each system and a leak test console, described

in *SPS 37-9*, was pressurized to 3500 psi during the test. The leak rates of gas systems designated No. 2 and No. 3 were within the maximum permissible leak rate specification of 30 standard cm^3/hr and have rates of approximately 22 and 4 cm^3/hr, respectively. However, System No. 1 indicated a gross leak rate of several hundred cm^3/hr. Investigation of System No. 1 revealed gross internal leakage from a pitch control valve. To investigate the possibility of contamination particles holding the poppet of the valve from fully engaging its seat, the valve was actuated several times with the system pressurized in an effort to blow the valve clear. The leakage rate diminished to approximately 22 cm^3/hr after repeated actuations confirming contamination and lack of mechanical damage or wear. Subsequently, this valve unit has been changed.

b. Contamination disclosure. Each *Mariner* R gas system is supplied with a series 5- and 2 μ-inlet filter assemblies. These filters have absolute ratings of 17 and 8 μ, respectively. The filter assemblies are not flight hardware, but provide a safety feature to reduce contamination potential during charging and operation assembly.

During spacecraft system tests and evaluation the filter assembly is at times removed (i.e., vibration environmental tests, cg and inertial testing, etc.) from the system. Possible mishandling of the filter assemblies, while they were removed, on gas system No. 1 and No. 2 resulted in questionable reliability of these two systems. This possibility arose at the time when the systems were in preparation for shipment to AMR. Investigation of gas system No. 1 was initiated by removing the pressure vessels and running filtration samples on the vessels and the high-pressure circuit. The vessels were found to contain a number of foreign particles in the 100- to 500-μ size. Filter samples taken at each bottle fitting, by flowing gas from the charging port to the fittings, revealed less contamination with low particle counts in the 10- to 50-μ size. After gas flushing the high-pressure circuit, filtration samples indicated particle size below 5 μ. The system was broken down further by eliminating each of the four jet valve assemblies from the system. Each jet valve assembly has a 10-μ inlet filter which was checked for contaminants. Three of the filters were found to be relatively clean with particles measuring 10 μ or less. The fourth filter had entrapped containments up to 60 μ in size and, in addition, a small piece of black string. After the low-pressure system was flushed with nitrogen gas, the system plumbing exhibited particle contamination below 5 μ.

Following this segment of the investigation, the pressure vessels were explored further to determine whether the contamination found in the vessels had been self-generated or introduced externally. The pressure vessels used on the *Mariner* R Project are of the uniweld construction type with an internal backup ring at the weld joint. The coupling to the vessel is accomplished with a special fitting and a crush metal seal. The inlet hole diameter is 0.152 in., making the cleaning operation of the vessels difficult. A syringe is used to inject cleaning solvent into the vessel and then a vacuum is used to withdraw the solvent from the vessel through a millipore filter. Repeated flushes and filter examinations are conducted until the cleanliness level of the vessel is 5 μ or less with attempts continuing to eliminate *all* contamination. If the vessels contained residual contaminants after cleaning, subsequent pressurizations and possibly vibration would loosen these contaminants and allow them to enter critical areas.

After cleaning the two vessels which were found to contain contaminants, the vessels were prepared for a shake test. One half pint of cleaning solvent was placed in the vessels, which were pressurized to 3000 psi during the test. One vessel was subject to 6.2 g and the second vessel to 10 g through the frequency range of 50 to 1000 cycles along the vessel axis. Following the shake test, the cleaning solvent from each vessel was examined and found to contain no contamination above the 5-μ level. This revelation substantiated the theory that the contamination was externally introduced and not self generated. This result further establishes the conclusion that the cleaning process used on these vessels, while in no way sophisticated, ensures retention of cleanliness levels after vibration environment.

c. Jet valve nozzle specification. The jet valve nozzles for the *Mariner* R spacecraft have been specified with the following nominal orifice size: $D_x = 0.0188$, $D_y = 0.0166$, $D_z = 0.0161$.

These values have been computed from a simplified formula involving the gas system parameters:

$$D^2 = \frac{I}{KPSE}$$

where

I = mass moment of inertia

α = angular acceleration required

$K = 1.43$ = constant involving π and the ratio of specific heats

P = characteristic regulation of the pressure regulator

S = moment arm

E = efficiency of the nozzles

E in the formula is the realizable efficiency of the nozzle which is influenced by the pressure P, orifice diameter D, and the contour of the flow path through the nozzle. For pressure levels of 14 to 15 psi and the nozzle contour selected, the efficiency E runs between 84 and 89%. These efficiencies have been analytically predicted and experimentally verified.

Because spacecraft angular acceleration is most critical at times of commanded turns, the nozzle orifice diameter is based on the inertias of the spacecraft configuration in the mid-course correction mode when the commanded turns are carried out. The nominal acceleration requirement at this time is 0.225 mrad/sec^2. The acceleration about the roll and yaw axis of the spacecraft is provided by pairs of jets whereas single jets are employed about the pitch axis for control. Therefore, each roll and pitch jet provides acceleration capability of one-half the nominal level.

The moment arms for the *Mariner* spacecraft are essentially the same as the *Ranger* spacecraft except for the pitch axis moment arm. The single pitch control jets have their thrust vector directed at an angle of 25 deg with respect to the roll axis. The center of gravity of the spacecraft lies approximately 1¼ ft down the positive roll axis from the cg position of *Ranger* spacecraft. This has reduced the pitch axis moment arm to 1.58 ft as compared to the *Ranger* pitch axis moment arm of 2.44 ft. The roll and yaw moment arms are 1.84 and 1.82 ft, respectively.

3. Long-Range Earth Sensor

The long-range Earth sensor (LRES), previously described in *SPS 37-14*, is now qualified and ready for flight (Fig. 12). A functional block diagram is shown in Fig. 13. Functional properties of the LRES are as follows:

Function	Property
Field of view	±2-deg roll and ±5-deg hinge
Radiant input range (bolometric at 6000°K)	5×10^{-11} w/cm^2 to approximately 5×10^{-7} w/cm^2
Power dissipation	6.5 w
Weight	6.2 lb
Null stability (absolute, with reference to external mounting pads)	0.1-deg 3 σ roll 0.25-deg 3 σ hinge

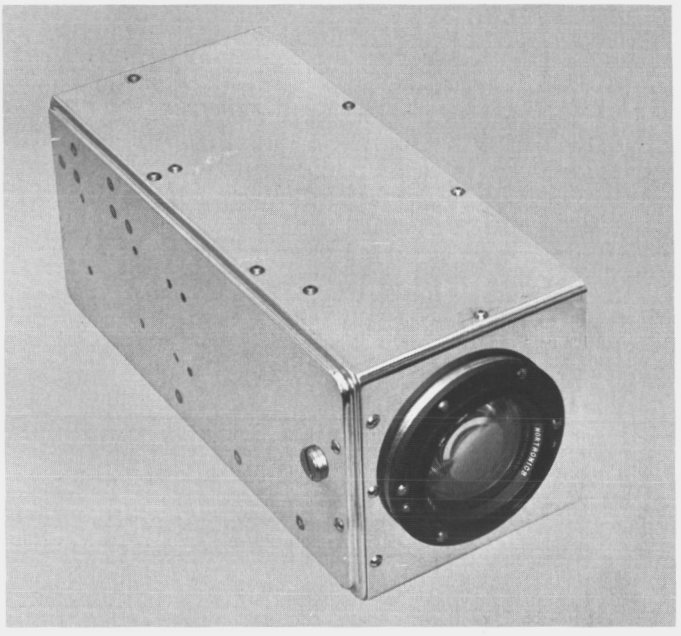

Fig. 12. Long-range Earth sensor

Function	Property
Null drift (expected in flight)	±0.02-deg roll ±0.05-deg hinge
Roll scale factor	4 v/deg ±10%
Hinge scale factor	2 v/deg ±10%
Roll saturation	4 v ±10%
Hinge saturation	4 v ±10%
Acquisition signal	7 ±1 v dc
Light intensity readout	0 to −3 v dc
Collecting optics	7 element f/1.2 2-in. focal length

The LRES is affected by off-axis disturbances to some degree. Extensive testing was performed to estimate and correct this defect. Results of the testing are shown in Figs. 14, 15, 16, 17, 18 and 19. During these tests, additional problems associated with properly simulating the space environment arose. Extraneous light was also reflected from test equipment, dark room walls, and operating personnel so that the results as shown should tend to be on the pessimistic side.

Testing of the LRES is done with an Earth–Moon simulator and a Griswold optical dividing head. The test setup and rack are shown in Fig. 20. During initial testing a problem arose due to the front surface of the vibrating reed being highly reflective. Light was reflected from

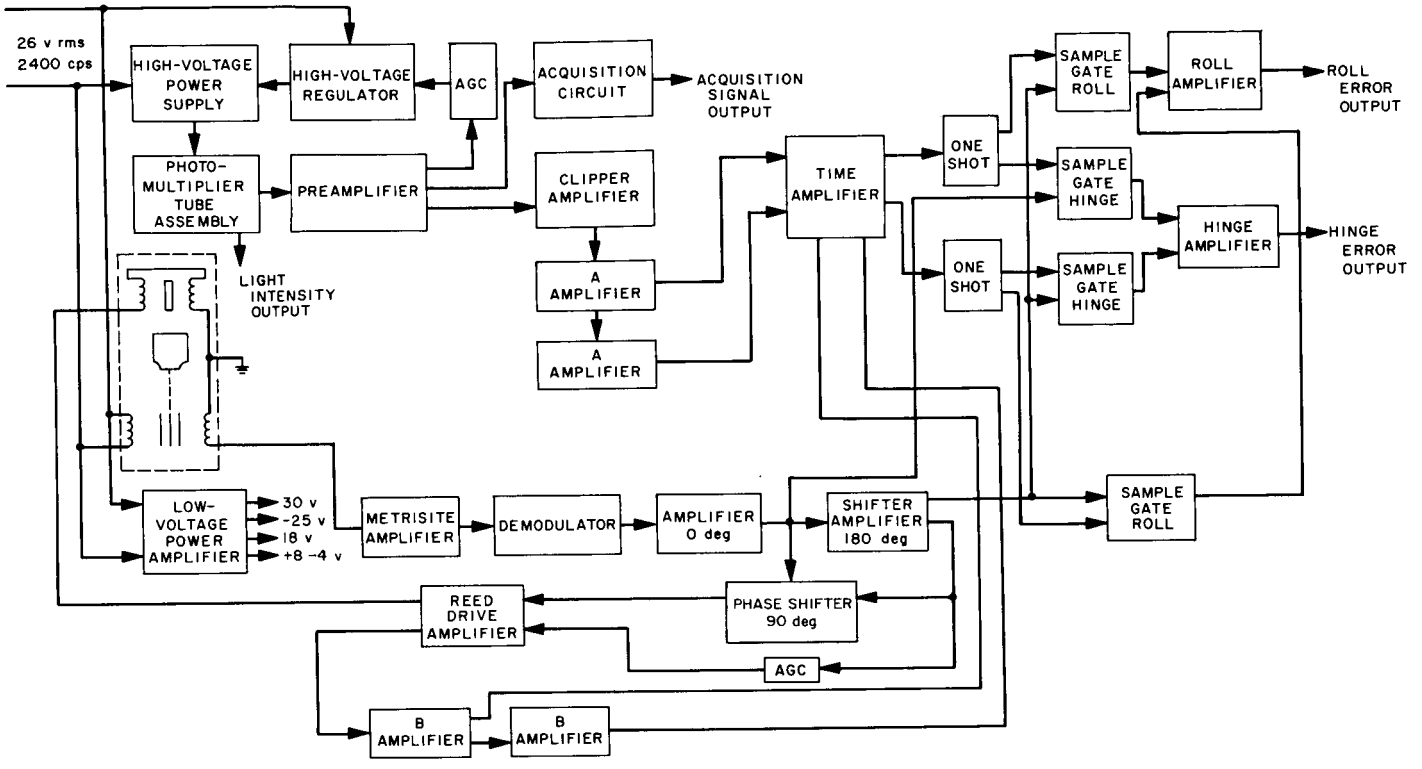

Fig. 13. Long-range Earth sensor functional block diagram

ROLL ANGLE, deg	LOSS OF ACQUISITION, w/cm^2	REGAINED ACQUISITION, w/cm^2
90	3.08×10^{-2}	2.52×10^{-2}
85	2.94×10^{-2}	2.38×10^{-2}
80	2.78×10^{-2}	2.09×10^{-2}
75	2.52×10^{-2}	1.82×10^{-2}
70	2.09×10^{-2}	1.40×10^{-2}
65	1.68×10^{-2}	1.12×10^{-2}
60	1.26×10^{-2}	9.60×10^{-3}
55	1.07×10^{-2}	7.00×10^{-3}
50	7.00×10^{-3}	4.49×10^{-3}
45	4.22×10^{-3}	1.82×10^{-3}
40	2.52×10^{-3}	1.68×10^{-3}

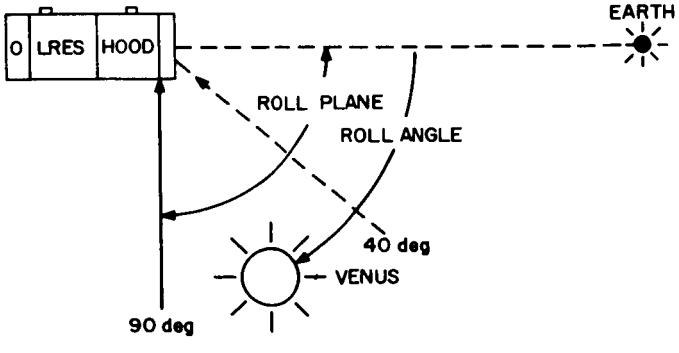

Fig. 14. Roll plane test

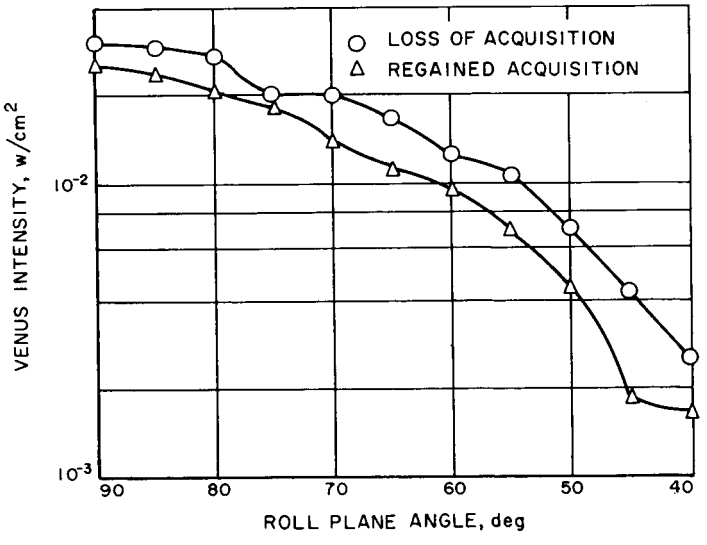

Fig. 15. Roll plane test, Part II

the reed 45-deg bevel to the black phototube housing and from there diffusely reflected to the photomultiplier. In simulated acquisition tests the Earth sensor would deliver an "acquisition" signal even though the Earth was as much as 20 deg out of the geometric field of view. The phase of the error signal at this time was also inverted so that Earth lock would have been prevented. This prob-

HINGE ANGLE, deg	LOSS OF ACQUISITION, w/cm^2	REGAINED ACQUISITION, w/cm^2
90	7.85×10^{-3}	6.25×10^{-3}
85	7.85×10^{-3}	6.25×10^{-3}
80	7.00×10^{-3}	5.05×10^{-3}
75	4.50×10^{-3}	3.36×10^{-3}
70	3.93×10^{-3}	3.22×10^{-3}
65	3.65×10^{-3}	2.52×10^{-3}
60	2.80×10^{-3}	1.68×10^{-3}

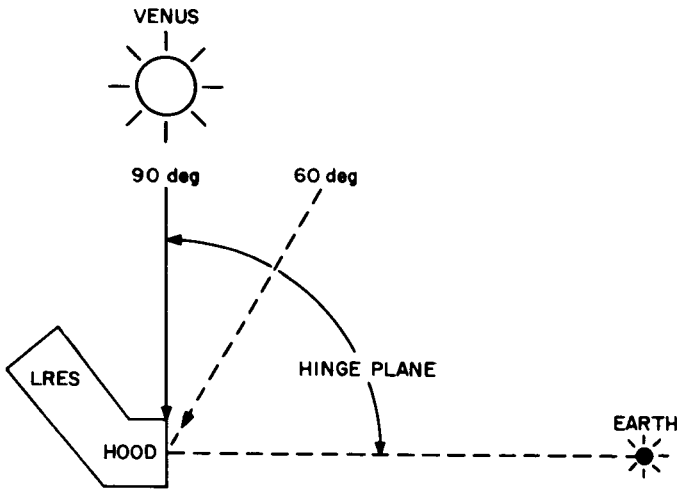

Fig. 16. Hinge plane test

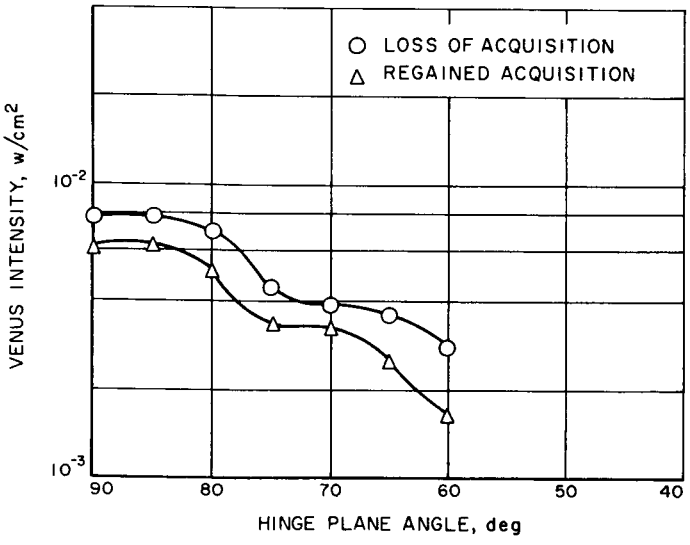

Fig. 17. Hinge plane test, Part II

lem was associated only with the high-intensity Earth. Solution was twofold:

(1) Blacken the reed, especially the 45-deg bevel.

45-deg PLANE DEVIATION, deg	LOSS OF ACQUISITION, w/cm^2	REGAINED ACQUISITION, w/cm^2
90	2.80×10^{-2}	2.11×10^{-2}
85	2.52×10^{-2}	1.54×10^{-2}
80	2.24×10^{-2}	1.40×10^{-2}
75	1.96×10^{-2}	1.40×10^{-2}
70	1.68×10^{-2}	1.08×10^{-2}
65	1.40×10^{-2}	1.08×10^{-2}
60	1.26×10^{-2}	9.62×10^{-3}
55	1.12×10^{-2}	7.53×10^{-3}
50	7.55×10^{-3}	6.18×10^{-3}
45	3.93×10^{-3}	3.08×10^{-3}
40	3.08×10^{-3}	2.52×10^{-3}

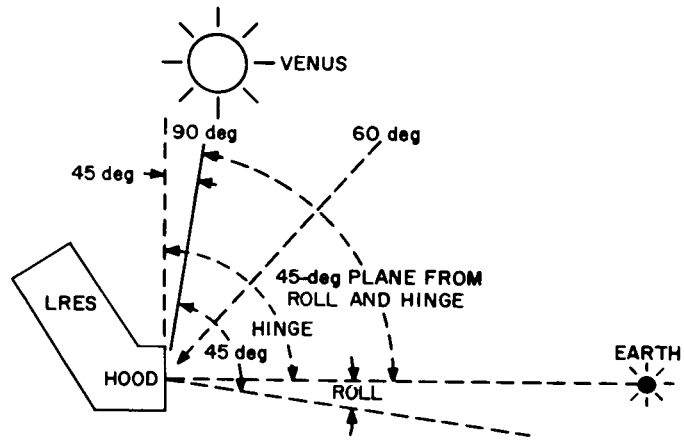

Fig. 18. 45 deg from both hinge and roll plane test

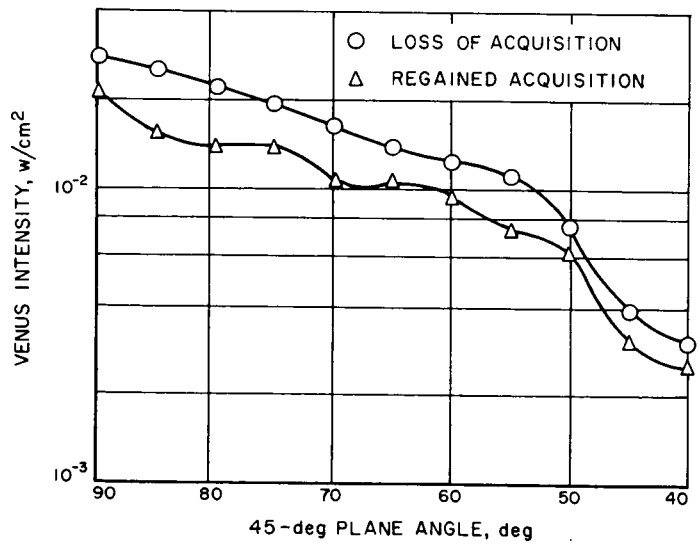

Fig. 19. 45 deg from both hinge and roll plane test, Part II

(2) Introduce wave-shape discrimination into the acquisition channel.

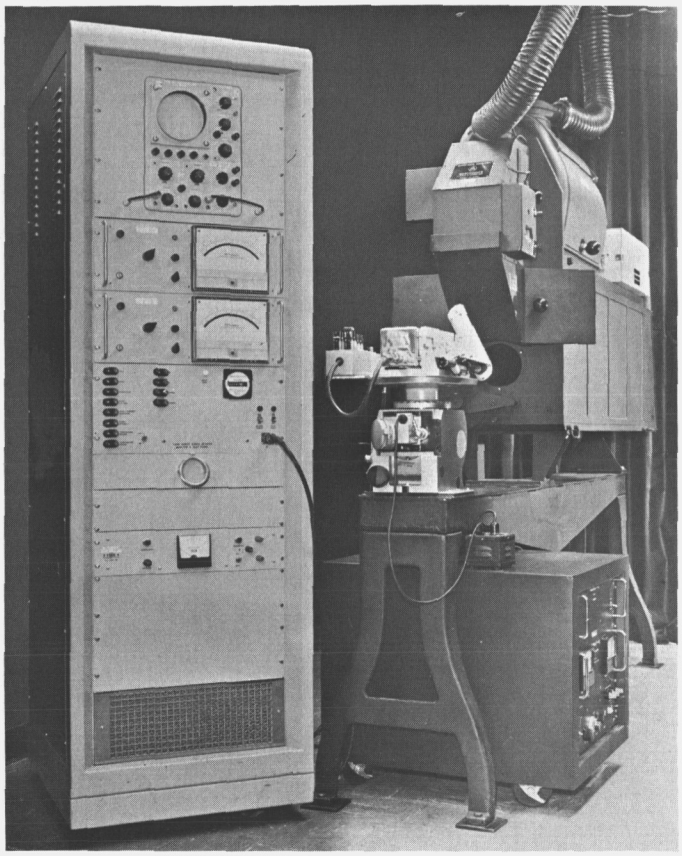

Fig. 20. LRES test equipment

An additional electronic problem was discovered. Electric motors operating in the vicinity of the Earth sensor caused erratic performance. This difficulty was traced to three fast-switching diodes in the reed drive loop. The three fast diodes (FD100) were changed to general purpose (IN457) to solve the difficulty.

4. *Earth–Moon Simulator*

The Earth–Moon simulator (Figs. 21, 22) is a device designed and fabricated by Nortronics to present a simulation of the Earth, Moon and Earth, or a star. The simulator provides the means with which to determine accuracy of alignment and flux level response. Continuous variable levels of irradiance are available for discrete distances from the Earth. There are provided five different Earth-phase positions for the larger size diameter Earth. The simulator provides a 5-in. diameter collimated light which is good to 5-sec-of-arc accuracy with reference to the point source. The integrated intensity of the flux density in the beam (per cm^2) from the simulator does not vary more than 5% over the center 3-in. diameter of the beam and not more than 10% over the entire 5-in. diameter. Earth diameters from 5.411 to 0.000452 deg can be simulated (in discrete steps). Color temperature between 0.35 and 0.8 μ approximates a 5200°K black body. Variations in flux are possible over a range of 159.7×10^{-6} w/cm^2 to 1.12×10^{-12} w/cm^2. The angular position of the Earth's geometric center is within 1 min of arc normal to the simulator external alignment surface. The outer edge of the simulated Earth is circular within 0.1% of the angular diameter plus 5 sec of arc.

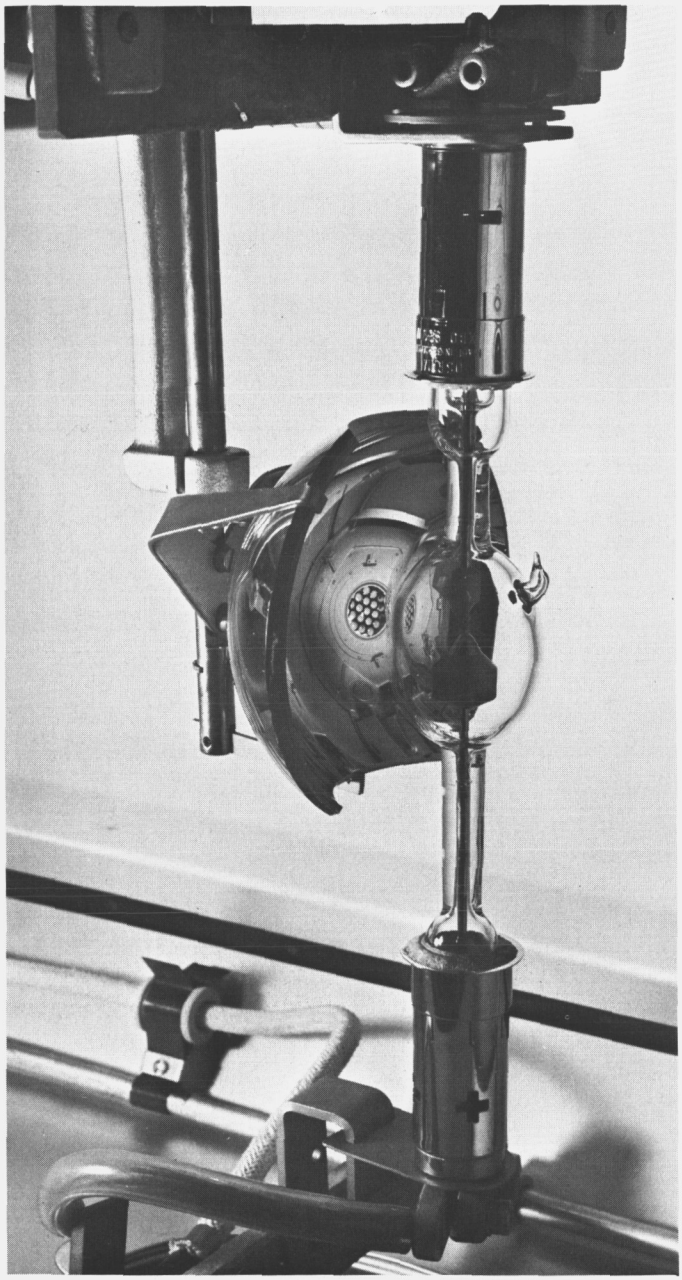

Fig. 21. Earth–Moon simulator light source and reflector

The light source is an Osram, 900-w xenon lamp, as shown in Fig. 21, with the parabola reflector mounted directly behind it. The light is projected through several lenses and reflected by three mirrors before it comes out of the simulator in the desired image. The intensity is varied with neutral density filters inserted in the upper sliding frame as shown in Fig. 22. Also in the same figure, the lower sliding frame is used to hold the different aperture plates which simulate the different sizes and configurations of the Earth and Moon. Swung out of the way from the front opening is a cover with a photocell mounted on it to measure the flux density which is present. The photocell is connected to the microammeter on the side of the simulator case and the reading is converted into flux density. The Earth–Moon simulator can also be made to simulate stars, such as Canopus, with some minor modifications.

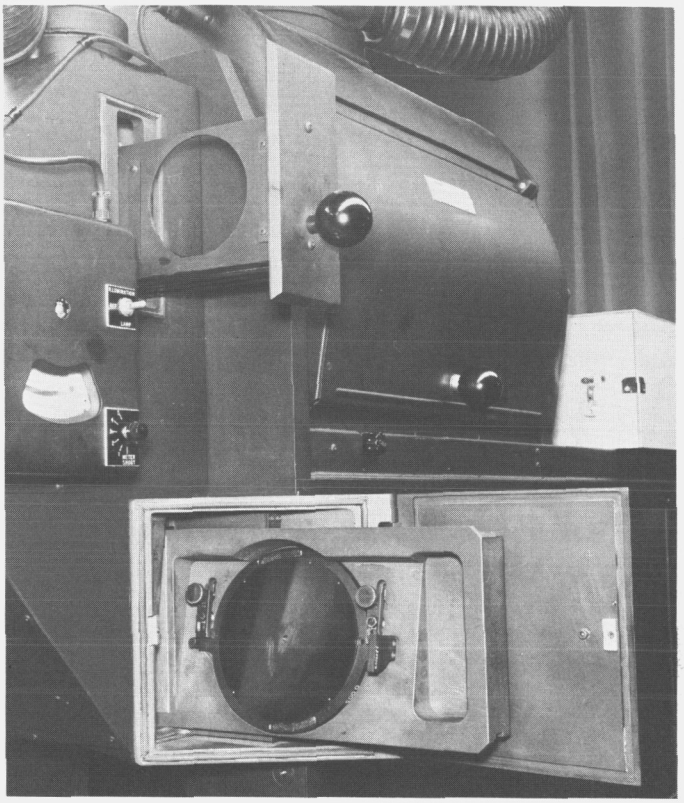

Fig. 22. Earth–Moon simulator

D. Telecommunications

1. *Antennas, RF Components and Couplers*

As reported in *SPS 37-15*, excessive RF coupler losses were encountered during the MR-1 and -2 match-mate test conducted at JPL during the period from March 20 through April 4, 1962. The source of this excessive loss was isolated to be in the flight shroud configuration. It has subsequently been determined that at the time of these tests the installation of the high-temperature RF cable in shrouds 6901 and 6901A was nonstandard.

On May 9 and 10 an additional match-mate test was performed between MR-1 spacecraft and the 6902 shroud and adapter. In this case the RF cable had been properly installed, the difference being that the 6902 RF cable snaked up the shroud cable trough from the quick disconnect to the top of the trough and then made a simple 180-deg turn into the coupler. On both the 6901 and 6901A shrouds the cable was laid in straight from the quick disconnect to the top of the trough and then made a double loop before being attached to the coupler.

For the May 9–10 RF coupler tests, the coupling loss from the communications pan through the omnidirectional antenna coupler system to the quick disconnect at 960 Mc was 9 db. The following table shows the coupling loss from the communications pan through the command antenna omni-coupler system to the quick disconnect:

Frequency, Mc	Coupling loss, db
905.7	51.2
900	37.2
895	28.2
891	26.3
890	29.3
889	29.2
885	29.0
880	28.7

It is to be noted that the high loss is at 905.7 Mc in this configuration, with another minor dip at 900 Mc. The loss did not exceed 32 db at any frequency from 899 to 875 Mc. It is apparent from this test that the high-command antenna-coupler losses encountered during the MR-1 and -2 RF match-mate tests at 890 Mc were caused by the looped high-temperature cable.

Based on results of the first MR-1 and -2 match-mate tests, JPL requested that a triangular perforated aluminum sheet be installed on top of the omni-coupler support frame. Identical coupler loss tests were performed on the MR-1/6902 shroud with this reflecting surface

installed. The omnidirectional antenna-coupler system loss at 960 Mc was measured to be 9.2 db. A frequency run on the command antenna-coupler system showed the following:

Frequency, Mc	Coupling loss, db
900	27.4
896	46 (unstable)
895	25.4
891	25.3
890	28.3
889	27.7
885	27.8
880	27.6

This test shows that the reflecting surface effected about a 1- to 2-db improvement in the coupling loss from 895 to 880 Mc; however, it also lowered the high loss frequency to 896 Mc.

Due to the fact that with the high-temperature cable correctly routed the command antenna-coupler system loss at 890 Mc is satisfactory with or without the special reflecting surface, LSMC was directed to delete the reflecting surface from the shrouds.

a. Omnidirectional antenna. As a result of the requirement for increased solar power on the spacecraft, the solar panels were increased in size. During a routine spacecraft type-approval vibration test which was run with the new solar panels, considerably higher accelerations than expected were noted on the structure supporting the omnidirectional antenna and the ends of the solar panels. As a result the omnidirectional antenna was being subjected to loads in excess of 50 *g*, and suffered a series of failures. The first failure resulted when the feet of the supporting buttresses broke. The feet were then strengthened and the tests repeated. The second failure resulted when one of the buttresses was torn away from the antenna support cylinder. The feet and buttresses were both strengthened on another antenna and the test repeated. The antenna then survived the tests successfully. The modifications required are minor and are being done to all flight antennas.

b. Omnidirectional antenna patterns. Radiation patterns of the forward omnidirectional antenna on *Mariner* R have been completed. A circularly polarized illuminating antenna is presently being mounted on the spacecraft antenna range. When this is completed, radiation patterns of the command antennas and the high-gain antenna will also be taken.

c. Radio-frequency interference. System tests at AMR revealed that 960-Mc signals radiated from the spacecraft high-gain antenna would saturate the spacecraft radiometer under certain test conditions. A test was run at JPL to evaluate this problem. In order to simulate flight and free space conditions, a working radiometer was mounted on a *Mariner* R full-scale mock-up, which was in turn mounted on the spacecraft rotator tower on the JPL Mesa facility antenna range. RF power at 960 Mc and at approximately the spacecraft transmitter power level was applied to the spacecraft high-gain antenna. Tests were then conducted to determine whether enough signal was coupled to the radiometer from the high-gain antenna to interfere with its operation. The worst case found during the test was at a high-gain antenna look angle of approximately 150 deg. For this position the radiometer output changed approximately 0.5 v when the 960-Mc power was turned on. Thus, it appears that an RFI problem does exist and a solution is being investigated.

E. Space Sciences

1. Solar Plasma Analyzer

During March and April four plasma analyzers were completed and integrated into the spacecraft system. Also, during this period an operating history was being accumulated on each of the analyzers.

a. Spacecraft integration. Although some interface problems with the spacecraft had been solved previously (*SPS 37-14, Mariner* R Solar Plasma Analyzer), the spacecraft had been operating on external (GSE) power and some subsystems were not in the spacecraft during the testing. When the spacecraft assembly was completed and operated on internal power, low-frequency ripple and 2400-cps spikes were observed on the electrometer output. The 2400-cps spikes were reduced considerably by isolating the plasma chassis from the spacecraft frame. The effects of the low-frequency ripple were reduced within tolerable limits by regulating the +12 B voltage to the first two stages of the ac amplifier triplet. The power for both stages was supplied by the existing preamplifier regulator, making the change relatively simple.

b. Operating history. Although the plasma analyzers met design specifications and worked well with the other related spacecraft subsystems, two additional problems became evident after the units had accumulated some operating time. First, the voltage across the reference diodes in the discriminators began changing. The sharp knees observed during the preinstallation component inspection deteriorated after the diodes were operated in the circuit. A new diode, designed to operate at lower currents, replaced the original diode. Additional protection was provided by increasing the current through the diode from 25 to 65 μa, thus moving the operating point further from the knee. Second, the 2N1118A demodulator transistor in the electrometer amplifier was replaced by a 2N329A after several mysterious failures. Although the 2N1118A was being operated well within the manufacturer's specifications, the thin etched base construction permitted punch-through with low-power voltage spikes. This damage has been attributed to voltage transients introduced by external measurement equipment at the demodulator test point. The 2N329A has a more rugged junction and, while not quite as good a switch as the 2N1118A, is satisfactory in this application. There have been no recurrences of either failure since the modifications were made.

c. Calibration. Each of the four plasma analyzers will be calibrated in a vacuum chamber prior to the final system test at AMR. Figure 23 shows the portable vacuum chamber and the test rack containing the calibration fixture.

d. Conclusion. The plasma analyzers have been working reliably in the spacecraft system. Examination of the history of each plasma analyzer subsystem has produced confidence in the long-term stability and reliability of the system. Documentation in the form of drawings, specifications, photographs, and motion pictures is completed. Support equipment is being prepared for shipment to AMR along with the plasma analyzers.

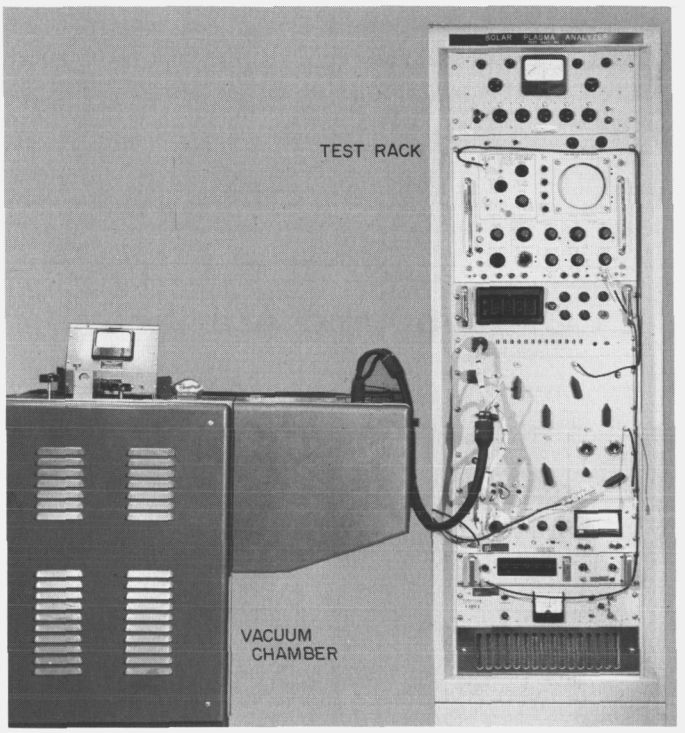

Fig. 23. Plasma analyzer calibration equipment

F. Propulsion

The function of the *Mariner* R mid-course propulsion system is to remove or reduce *Agena* B injection dispersion errors so that a Venus flyby with a sufficiently small miss distance can be reasonably assured. This function is performed during a single spacecraft mid-course maneuver (executed approximately 8 days after launch) during which time the spacecraft turns to a prescribed position in space and imparts a corrective impulse by means of the mid-course propulsion system. A description of the *Mariner* R mid-course propulsion system was presented in *SPS 37-12.*

The development program to date has been covered in *SPS 37-12* through *-15.* Since the last reporting period, project activities have centered around generation of specifications and procedures to be used in pre-launch and launch activities.

The MR-1, -2, and -3 mid-course propulsion systems have been delivered to AMR in preparation for launch. Immediately after their arrival at AMR, the three propulsion systems were subjected to a leak test of all fittings. The MR-1 and -2 propulsion systems successfully passed the leak test. Several leaks were noted in the MR-3 nitrogen tank fitting to which is attached the nitrogen tank, nitrogen tank pressure transducer, and the nitrogen tank explosive valves. The high-pressure circuit was disassembled, and the fittings were examined in detail. Several scratches were noted on the faces of fittings against which O-rings must seal. The fittings were

polished and the propulsion system was reassembled. Another leak check of the propulsion system revealed no leakage, and the propulsion system was considered flight-worthy.

G. Supporting Activities

1. Planetary Environmental Test Program

During May and June a total of 35 experimental, 22 type-approval, and 73 flight-acceptance environmental tests associated with the *Mariner* R Program were handled by the JPL Environmental Test Laboratory (Table 1).

2. Vibration Testing

a. **Mariner *R*.** The *Mariner* R structural test model was vibration-tested during the month of June to determine the amount of additional dynamic load on the superstructure imposed by lengthening one solar panel (Fig. 24). The Calidyne L-249, 30,000-lb force shake table and the Ling 175-kw power amplifier were used. Three tests were run in each of three orthogonal directions: (1) low-frequency sinusoidal test (1 to 40 cps), (2) high-frequency sinusoidal test (30 to 200 cps), and (3) high-frequency random vibration test (15 to 1500 cps), and combined random vibration–sinusoidal test.

In addition, several vibration tests were run with actual superstructure-mounted flight hardware to assure equipment operation in this more severe environment.

Table 1. *Mariner* R usage of ETL facilities during May and June 1962

Facility	No. of tests
Space simulator, 6-ft	5
Vacuum	13
Vacuum–temperature	30
Vibration	56
Low-frequency vibration	6
Centrifuge	6
Shock	3
Temperature	8
Temperature–humidity	2
Explosive atmosphere	1
Total	130

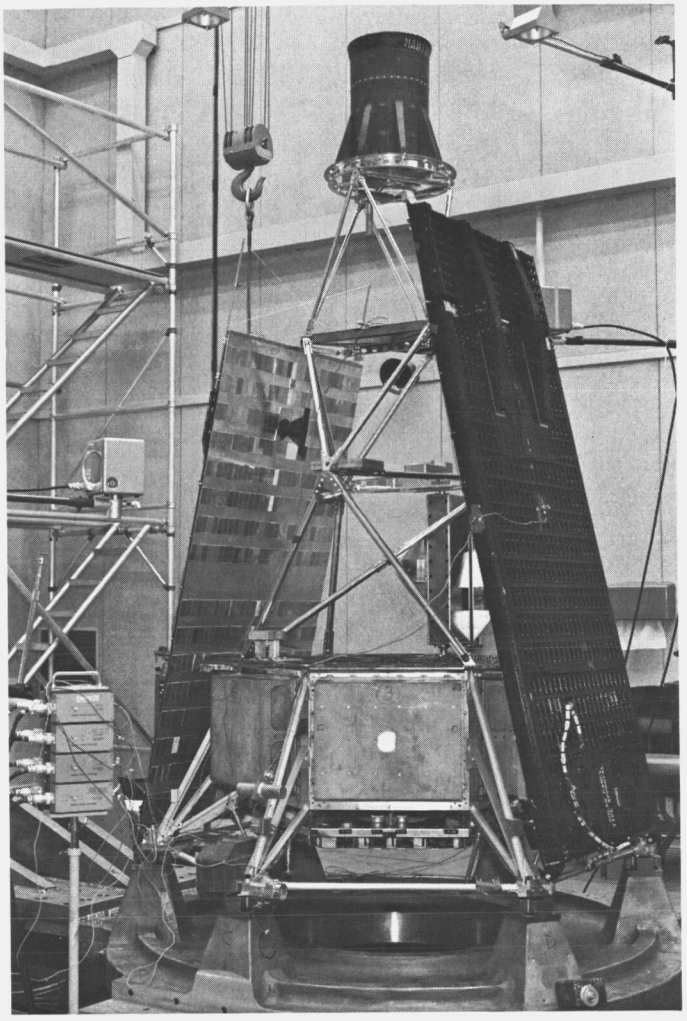

Fig. 24. *Mariner* R modified dynamic structural test model

3. Space Simulation Testing

a. **Mariner *R*-2.** Early in May, MR-2 (hex portion) was tested in the 6-ft space simulator. The telemetry system was calibrated at different temperatures and the spacecraft life-tested at predicted flight temperature for 228 consecutive hours. The environment during steady state was: vacuum, 5×10^{-6} mm Hg; shroud temperature, $-300°$F. Resistance heaters mounted on the spacecraft controlled the bus temperature.

b. **Mariner *R temperature control model* (*TCM*).** Four tests were conducted on the hex portion of the TCM in the 6-ft space simulator to establish the paint pattern based on the latest internal power information. The

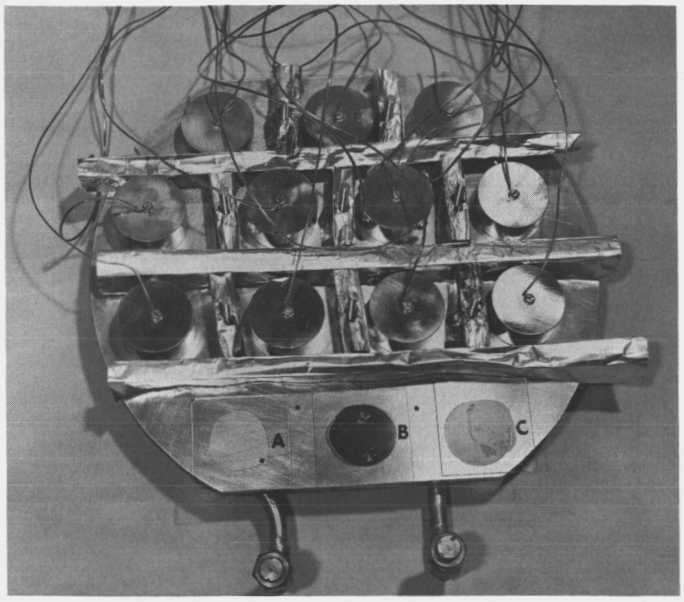

Fig. 25. Disc assembly for vacuum grease testing

cumulative test time was 6 days. Four modes[a] of operation were simulated during each test. Solar simulation was provided by heating pads mounted on the spacecraft. The simulator's carbon arc lamps were also used during part of the tests.

c. Vacuum grease temperature conductivity tests. Greases are needed that will efficiently transfer heat to components being vacuum-tested under space thermal conditions. A program is underway to develop a grease that will satisfy the heat conductivity requirements and simultaneously maintain stability over the wide range of space test environmental conditions. Figure 25 shows the test equipment. The sample is smeared on a copper disc which is then placed in contact with a copper temperature-control plate. The test assembly is evacuated and the heat-transfer characteristics of the sample are determined at various temperatures of the control plate. Preliminary tests made with silver powder mixed with selected vacuum greases did not indicate any substantial improvement in the heat-transfer properties of the greases.

[a]Modes of operation refers to a particular combination of operating conditions of internal electronic equipment and external heat inputs to the spacecraft.

4. Acoustical Testing

Environmental testing has been concerned mainly with using vibration generators to mechanically simulate the vibration levels to which equipment will be subjected. Spacecraft performance records have shown that, up until now, this seems to be a successful technique. However, the advent in the foreseeable future of rocket thrusts measured in the millions of pounds, compared with present-day thrusts of less than 500,000 lb will considerably increase the sound pressure level at the spacecraft. Light, large surface area equipment, such as panels and antennas, will be particularly vulnerable to increased acoustical excitation. Acoustical testing will then become increasingly important.

The Environmental Test Laboratory has designed and built an acoustical chamber. The chamber is now in operation, using two mid-range (300 to 8000 cps) speakers, each driven by a 65-w amplifier. A frequency response survey of the test area of the chamber was made to determine the input spectrum. Preliminary tests have been conducted to determine the mechanical properties of vibration fixtures (Fig. 26) and to determine general acoustical test requirements for future environmental testing.

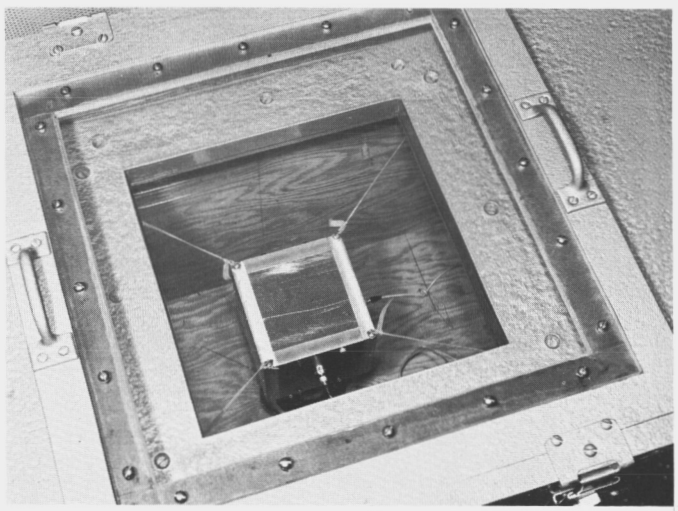

Fig. 26. Test article for vibration fixture analysis in acoustic chamber

III. *Mariner* B Project

The primary purpose of the *Mariner* B Project is to permit scientific investigations of the planet Venus during the periods of availability in 1965 through 1967 and Mars during the periods of availability in 1964 through 1967. Secondary purposes in order of priority are (1) to make interplanetary scientific investigations in the regions between Earth and Mars, (2) to develop experience in the design of a spacecraft that has considerable flexibility with regard to the specific missions it is basically capable of covering, (3) to provide experience and knowledge which will permit a quality and efficient design of the later *Voyager* spacecraft. To these ends, the spacecraft will be designed for a precision flyby mission and will incorporate the capability of either carrying or not carrying a small landing capsule. The *Mariner* spacecraft will be injected by the *Centaur* launch vehicle. It is expected to launch two identical probes at each of the planet launching opportunities. Deep space probes, to be launched in between periods of Mars and Venus availability, are included in the *Mariner* B Project.

The preliminary design phase of *Mariner* B has been completed. Mission objectives, design characteristics and restraints, and functional specifications have been finalized and published. The Project Development Plan has been revised and is being prepared for re-issue. The detail design phase, including prototype fabrication, is proceeding on schedule.

A. Systems Operations

1. Spacecraft System Design Verification

During the reporting period, effort was directed toward improving and refining the content of the Design Characteristics and Restraints Specification for the *Mariner* B System Test Complex (STC). Information copies were distributed to cognizant personnel of the various subsystem groups for review and comment. A meeting was held at which the comments were presented for consideration. After appropriate discussion by the attendees the suggestions were either accepted or rejected. The percentage of the recommendations accepted far exceeded the rejections, which is an indication of the quality of the ideas presented.

It appears that the STC for *Mariner* B will be an appreciable improvement over those on previous projects. For example, when it was necessary in the past to diagnose a subsystem, the subsystems with which it had an interface also had to be turned on, and test set operators had to stand by and be ready to provide inputs and output loads to the subsystem under investigation. Subsystem interface simulation will now be a requirement and, insofar as practicable, each subsystem test set shall have the capability of independently simulating the output loading and the inputs which the subsystem experiences during spacecraft operation so that the subsystem can be operated independent of the rest of the spacecraft and STC. Another improvement is the require-

ment that the input power to each test console be isolated. The ac power distribution lines will, therefore, be protected from the transient effects of power switching normally performed by the subsystem test sets. Tentatively, the isolation specified is to be not less than 40 db over the frequency range of 50 kc to 1.0 Mc. It is anticipated that the use of a triple or quadruple shielded isolation transformer will evidence compliance with this requirement.

The Systems Division has devoted considerable thought and effort toward improving spacecraft system testing as a means of demonstrating that the spacecraft is capable of attaining the mission objectives. A necessary prerequisite to performing system tests which will provide a maximum of data for analysis and evaluation is a spacecraft which is relatively free of symptomatic failures during test. It has been proposed that this be accomplished by extensive life-testing at the piece part, assembly, and subsystem level, during design and prior to delivery of the spacecraft to the system test area. Past system test programs have been somewhat subsystem-oriented. The objective was that the spacecraft survive these tests rather than demonstrate a substantial performance margin.

Current planning requires the early preparation of a spacecraft System Design Verification Specification which will delineate specific technical requirements of the system test. The test requirements will be based on the spacecraft design criteria, characteristics, and design restraints. Additional emphasis will be placed on establishing performance trends, checking the redundancy provisions in all modes of operation, checking performance margins of the various system loops as a function of varying stimuli and varying operational modes.

2. *Mars–Venus Capsule Study*

A scientific objective of the *Mariner* Project is to investigate the planetary atmospheres of Mars and Venus. In the case of Mars, studies have been performed and reported, beginning with *SPS 37-7*, on various aspects of the problem of sending instrumented capsules through the atmosphere for survival landing on the surface. A 4-month study subcontract has been awarded to General Electric Co. by JPL to examine, from an over-all system aspect, the feasibility of performing capsule missions to Venus. The survival of the capsule is not a requirement, and the study results are to be related to future capsule missions to Venus and Mars. In addition, suggestions and recommendations will be made for supporting research and development in the outlined critical areas (Table 1) where appropriate.

Table 1. Areas critical to the general feasibility of the Venus mission

Area	Problem
Communications	Signal acquisition after entry
	Automatic phase-lock system for capsule-to-spacecraft communication
	Type of system and antenna configuration
	Effects of Venus atmosphere sheath characteristics and effect on design
Power	Effect of long lifetime requirements on efficiency and reliability
Instrumentation	Data acquisition during entry flight regime
Thermal control	Control during transit
	Control during entry heating phase
	Effect of ambient temperature in atmosphere
Sterilization	Effects of requirements
Entry design (payload and data retrieval capability)	Effects of parameters: ballistic coefficient, arrival velocity, entry angle, atmospheric model
Equipment survival and reliability	Effects of temperature, pressure, thermal and dynamic shock
Capsule mission reliability and capability	Utilization of changes in spacecraft capability, e.g., effects of change in approach guidance on subsystems

Within this period General Electric Co. will conduct parametric analyses of the problems associated with the systems and subsystems design of a capsule, including consideration of the transit phase, separation from the spacecraft, and planetary encounter and descent into the atmosphere of the planet Venus. Potential capsule designs will be considered in order to demonstrate solutions to the problems encountered during the study.

The study is to consider the feasibility of performing the Venus capsule mission within the constraints of (1) schedule requirements and (2) the spacecraft interfaces. The objective is not necessarily to establish one particular configuration but to investigate and establish the primary controlling performance and capability parameters as they affect capsule design. This will involve a system analysis based on the examination of the effect of the various parameters, which will include but not be limited to: (1) the capsule gross weight; (2) total amount of returned data, and (3) complexity and reliability with respect to any of the areas listed in Table 1.

In order to ascertain the feasibility of accomplishing the Venus capsule mission from injection through entry into the planetary atmosphere, the study is to include:

(1) a detailed listing of the problem areas, (2) a detailed listing of the methods of problem solution, and (3) the solution of such problems within the time allowed with respect to the present and anticipated technical state-of-the-art and with sufficient reliability to achieve the mission.

Examination of the feasible capsule performance and capability is to be made in terms of the instrumentation capacity, information rate, and lifetime at the planet.

3. Planetary Entry Capsule Altimeter

A feasibility study has been completed by Wiley Electronics Co. for a short-pulse radar altimeter for application in the *Mariner* B planetary entry capsule. Altitude data obtained in the planetary near-approach and entry phase of capsule missions will be used to determine atmospheric entry angle of the capsule, to correlate scientific measurements with altitude, and to provide a fusing signal for deploying the parachute.

Entry-angle determination, lower atmospheric altitude measurements, and fusing are independent requirements. The more difficult, from a feasibility standpoint, is entry-angle determination due to maximum range requirements and motion of the capsule at atmospheric entry. If this objective is obtained, the lower atmospheric measurements and fusing requirements would be met. The feasibility study is therefore predicated on an entry-angle determination basis. Altimetry to perform only lower atmospheric measurements and fusing would not be limited to the same restraints as entry-angle determination.

Major design parameters which have dictated the radar configuration for study are the capsule's motion at entry and a high order of range resolution. The capsule at time of atmospheric entry will have a random spatial orientation, and will have angular rates of 4 deg/sec or less. Under these conditions, isotropic radiation is required to ensure radar returns from the planetary surface. The constraint of isotropic radiation, maximum range (300 km), and altitude resolution (15 m), immediately infers high altimeter–transmitter peak power. Transmitter peak power for the conventional pulsed-radar using experimental extrapolated data is 50 kw. The feasibility of an altimeter for the intended mission is based on the possibilities of reducing this power to some practical value. Two means provide transmitter peak power reduction to 2.5 kw: (1) the use of a low transmitting frequency, and (2) chirp techniques. The following is a description of the study without comment on its feasibility for any specific capsule application.

a. Transmitter power requirements. Since an omnidirectional antenna is required, due to random motion of the capsule at entry, the size of the target area illuminated on the planetary surface will be limited only by the duration of the transmitted pulse and not by antenna beamwidth. The equations for a pulse-width-limited radar are derived for isotropic scattering and pure specular reflection of the incident energy on the planetary surface. It is shown for isotropic scattering

$$\frac{P_r}{P_T} = \frac{K^2 G^2 \lambda^2 C\tau}{32\pi^2 h^3} \tag{1}$$

and for pure specular reflection

$$\frac{P_r}{P_T} = \frac{G^2 \lambda^2}{64\pi^2 h^2} \tag{2}$$

For definition of terms see glossary at end of this section. The minimum detectable power is related to altitude for isotropic scatter by $1/h^3$, and for pure specular by $1/h^2$. If all of the power is reflected by isotropic scattering, the required transmitter power from Eq. (1) would be 250 kw, and by pure specular reflection from Eq. (2) would be 50 w. Calculations assume $K^2 = 0.1$, $f = 100$ mc, $\tau = 0.1$ μsec, $h = 10^6$ ft, and $P_r = 8 \times 10^{-13}$ w. In experimental work it has been found that true specular reflection and complete isotropic scattering are rare occurrences. The actual received power is an admixture of specular and scattered components. The relative proportions of each are complex functions of wavelength, pulse width, altitude, angle of incidence, and surface condition.

Transmitter peak power requirements in this study have been based on experimental work conducted at the Sandia Corporation and the University of New Mexico. Table 2 is a result of experimental data which has been extrapolated to 10^6 ft for several grades of terrain. In the process of extrapolation, isotropic scattering was assumed. The total path attenuation is defined by

$$A = 10 \log \frac{G^2 P_T}{P_r}, \text{ db} \tag{3}$$

which groups the many complex factors affecting power return into a single quantity.

Table 2. Extrapolated path attenuation for pulse-width limited altimeter with $f = 415$ Mc, $\tau = 0.2$ μsec, $h = 10^6$ ft

Location and type of terrain	$A = 10 \log \left(\frac{G^2 P_T}{P_r}\right)$, db
Farmland, near Wahpeton, N. D. (summer)	169
Woods at Pine Island, Minn. (summer)	180
Residential area, Kansas City, Mo.	164
Residential area, Minneapolis, Minn.	170
Yucca Lake bed (smooth and moist)	155
Sandy desert near Yucca Lake	162
Rough desert near Salton Sea	172
Fresh water (calm), Elephant Butte Reservoir	158
Fresh water (rough), Lake Bemidji	156
Salt water, Salton Sea	156

The minimum detectable received power P_r is based on a signal-to-noise ratio of 13 db to obtain a false triggering probability of 1 in 100, a receiver bandwidth of 10 Mc to maintain good pulse response, and a receiver noise figure of 3 db, the minimum received power is calculated by

$$P_r = (S/N)\, FkTB$$
$$P_r = 16 \times 10^{-13} \text{ w} \qquad (4)$$

From the experimental data shown in Table 2, the most likely condition assumed for Mars is an average between sandy desert and rough desert. The total path attenuation for this condition is 167 db. This data was obtained at an operating frequency of 415 Mc, and with a pulse width of 0.2 μsec. Through the relationships shown in Eq. (1), it is noted that a decrease in pulse width to 0.1 μsec doubles the power ratio, and a decrease in frequency to 104 Mc, increases the power ratio by a factor of 16. Losses in the antenna for two-way transmission, and in the duplexer were estimated at 7 db. Summing up the total path attenuation in the following manner gives

$$\text{total path attenuation} = 167 \text{ db} + 3 \text{ db} - 12 \text{ db} + 7 \text{ db}$$
$$= 165 \text{ db}$$

The transmitter peak power required is calculated by using Eq. (3) and (4).

$$P_T = (16 \times 10^{-13})\,(10^{16.5}) \text{ w}$$

$$P_T = 50 \text{ kw}$$

b. Power reduction techniques.

Low operating frequency. The only system parameter which is subject to some choice is λ, the operating wavelength. By choosing the lowest operating frequency consistent with an efficient capsule antenna design, an increase in received power is obtained. The lowest operating frequency which could be chosen was approximately 100 Mc. From Eq. (1) it is noted that received power varies exponentially to the second power with operating wavelength. The choice of 104 Mc as the operating frequency provides the maximum obtainable power reduction by wavelength selection.

Chirp technique. Chirping, or pulse compression, techniques are introduced to reduce further the transmitter peak power requirements while retaining high-range resolution. This is done by transmitting a long rectangular FM pulse in which frequency varies linearly with time, from a low frequency at the beginning of the pulse to a high frequency at the end. The returning signal is amplified in the usual way and then passed through a dispersive network in which the delay is a linearly decreasing function of frequency. Thus, the low frequencies at the beginning of the pulse are delayed just enough to emerge on top of the later high frequencies. The net result is that the long pulse is collapsed into a short pulse of $\sin x/x$ shape, but with increased peak amplitude.

Referring to Fig. 1, if the long transmitted pulse has duration T sec, during which frequency varies linearly over the range Δf then the collapsed pulse has a duration $T = 1/\Delta f$ sec between 4-db points. The peak power has been increased by the collapse ratio $T\Delta f$. In the case considered here the required altimeter transmitting peak power can be reduced by the collapse ratio by a factor of 20 to 2.5 kw.

c. Antenna design. An omnidirectional antenna is required due to the random motion of the capsule. The most promising antenna design which was investigated is shown in Fig. 2. The antenna consists of a metallic shell with $\lambda/4$ wave slots, spaced at intervals of 90 deg on the base. Each slot is excited at its high-impedance point close to the open end by a balanced 300-ohm line. Slots 1 and 3 are fed in phase while 2 and 4 are in phase, but in quadrature with 1 and 3. This configuration gives circular polarization along the axis of symmetry.

The inner brass shell shown in Fig. 2 simulates the capsule payload structure. The close proximity of the structure reflects power from the rear side of the slots which drastically changes the impedance characteristics

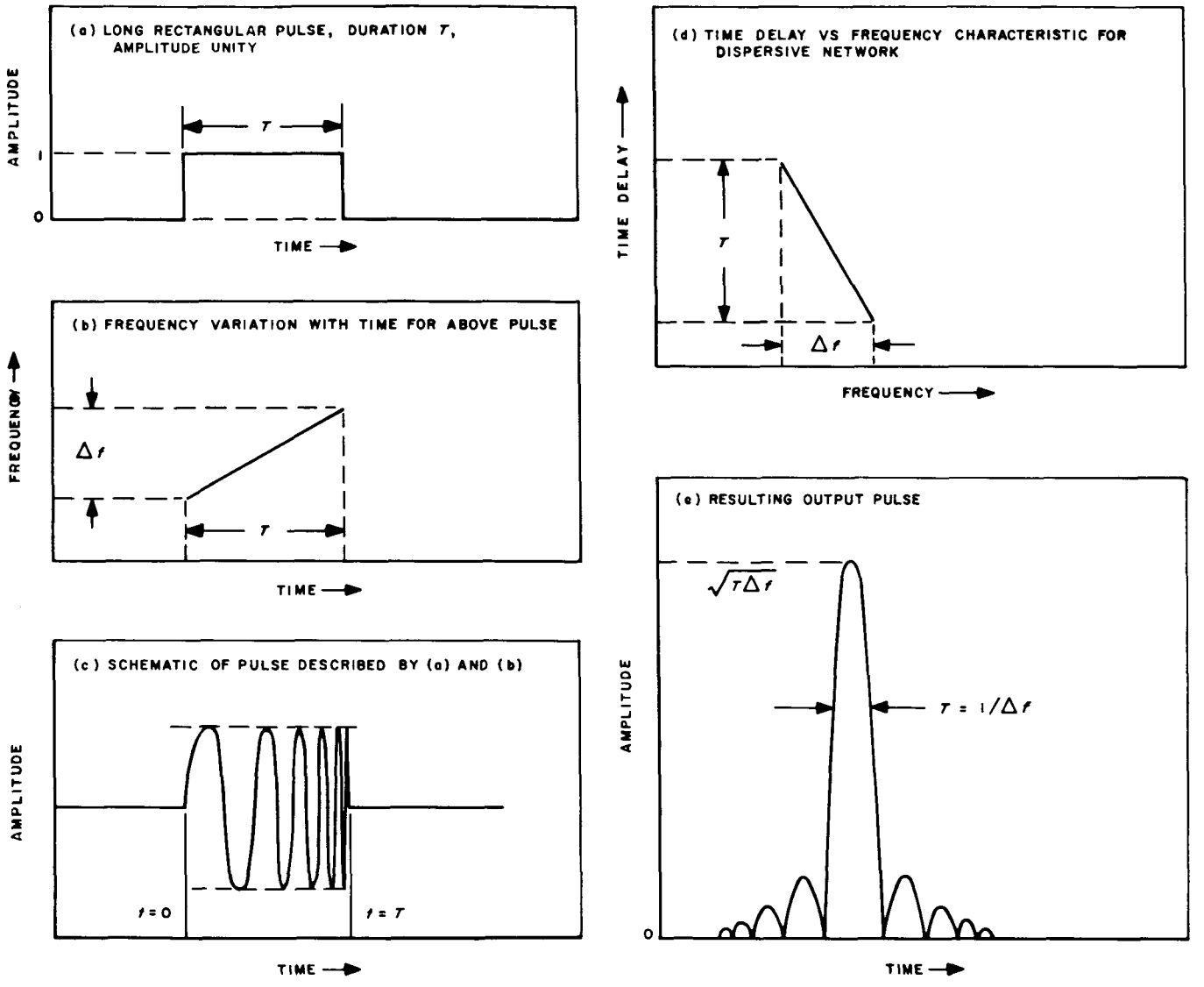

Fig. 1. Chirp signal characteristics

of the slots. In order to evaluate the feasibility of the antenna, it was necessary to load the slots. This was done by placing $\lambda/4$ wave shorted stubs along the slots which served to isolate the slots. Figure 3 illustrates the antenna pattern in the azimuthal direction which was obtained by tests on a ¼-scale model of this configuration.

While this technique is completely feasible for isolating the rear of the slots, a more attractive method would use triplate strip line technique for exciting the slots.

d. Accuracy analysis. An altitude accuracy of 50 ft is desired. A list of expected altitude errors and their causes appears in the next column. The second and third items would be expected to vary as a function of altitude.

Cause	RMS error, ft
Crystal oscillator drift, 0.005%/°C and 50°C temperature range	10
Deviation of illuminated terrain area from a plane due to spherical shape of planet (Venus)	10
Movement of vehicle during flight of pulse (Venus)	10
Magnetic pulser jitter using 25-Mc first stage	10
Register quantization error	20
Trigger jitter (No AGC can be used to set trigger level due to the low PRF)	30
Calibration	10
Transmitter jitter due to delay and slope variations	10
Unaccounted	20

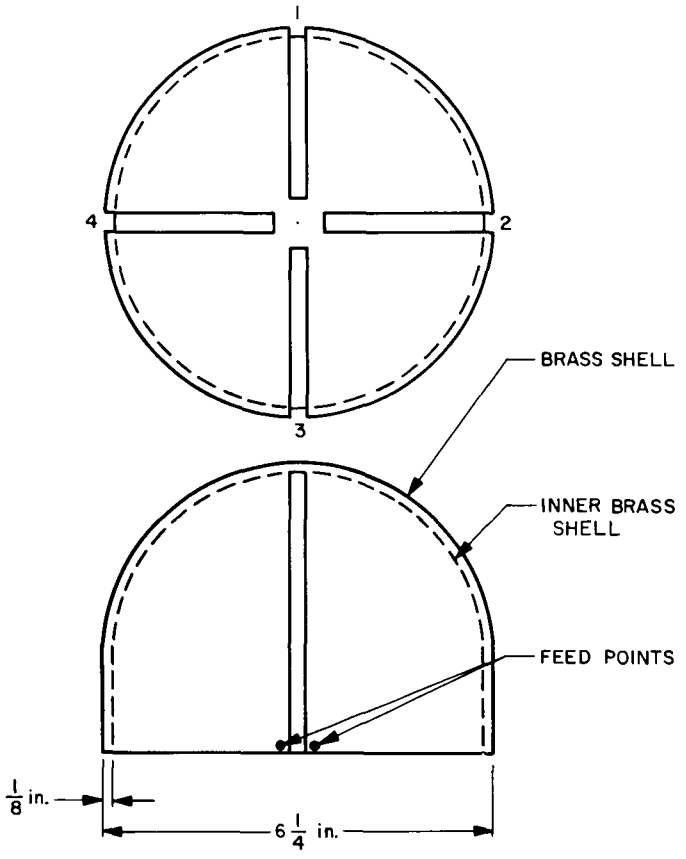

Fig. 2. Antenna edge or notch slots

Although not all of these errors are completely random, the best estimate of the total error is perhaps the rms sum, which is 48 ft.

e. Weight, volume, and power consumption. The total weight of the altimeter electronics, battery, and antenna is 18 lb. The electronics power dissipation is 19.2 w. Weight, volume, and power consumption for all components of the altimeter are itemized in Tables 3, 4, and 5.

f. Altimeter circuits and mode of operation. The time-measuring system shown in the block diagram (Fig. 4) is essentially a solid-state time-interval meter. The 25-Mc oscillator is used as the clock. The quantization error due to the lack of synchronization between the clock and the transmitted and received pulses is plus or minus one count, or 20 ft of range. The counting is carried out by three basic circuits. The first, for the very high speeds, is a ring counter. The use of ring counters makes it possible to count reliably at these high clock frequencies without excessive complexity or power consumption. The second

Table 3. Altimeter electronics package

Item	Weight lb	Weight oz	Power, w	Volume, in.^{3}
Chirp network, 45 sections, 20.1 collapse ratio	3		0	90
Duplexer		6	0	4
Transmitter, PRF = 100 pps		8	5.7 filament 1.5 plate, 30% efficiency	10
Transmitter driver		8	0.1	6
Receiver		6	1.0	6
Crystal oscillator and register	1	8	3.0	32
Video amplifier and fuzing unit		12	1.0	15
Magnetic pulse modulator		12	1.5, 50% efficiency	12
Power supply	1		4.4	20
Mixer–SSB modulator module		4	1.0	6
Structure and miscellaneous	2		0	200
Total	11		19.2	401

Table 4. Battery supply to operate for 5 hr

Item	Weight lb	Weight oz
Sintered electrode Ni-Cd batteries, 60 w-hr/lb, 96 w/hr required	1	10
Case and interconnections		6
	2	

Table 5. 104-Mc turnstile slot antenna behind ablation shield

Item	Weight lb	Weight oz	Volume, in.^{3}
½-in. thick honeycomb cap, 4 lb/ft^3	1	10	686
4-mil inner and outer Al cap skins		14	
4-mil Al sheets to form backing cavities	1		
264-in. RG62 AU 93, cable ½ oz/ft		11	10
Four twin-Ax T's		4	6
Four series tuned matching circuits and mounts		4	4
Miscellaneous		5	
	5		—[a]

[a]Volumes are not totaled, since some of this volume is outside the capsule dome and some inside.

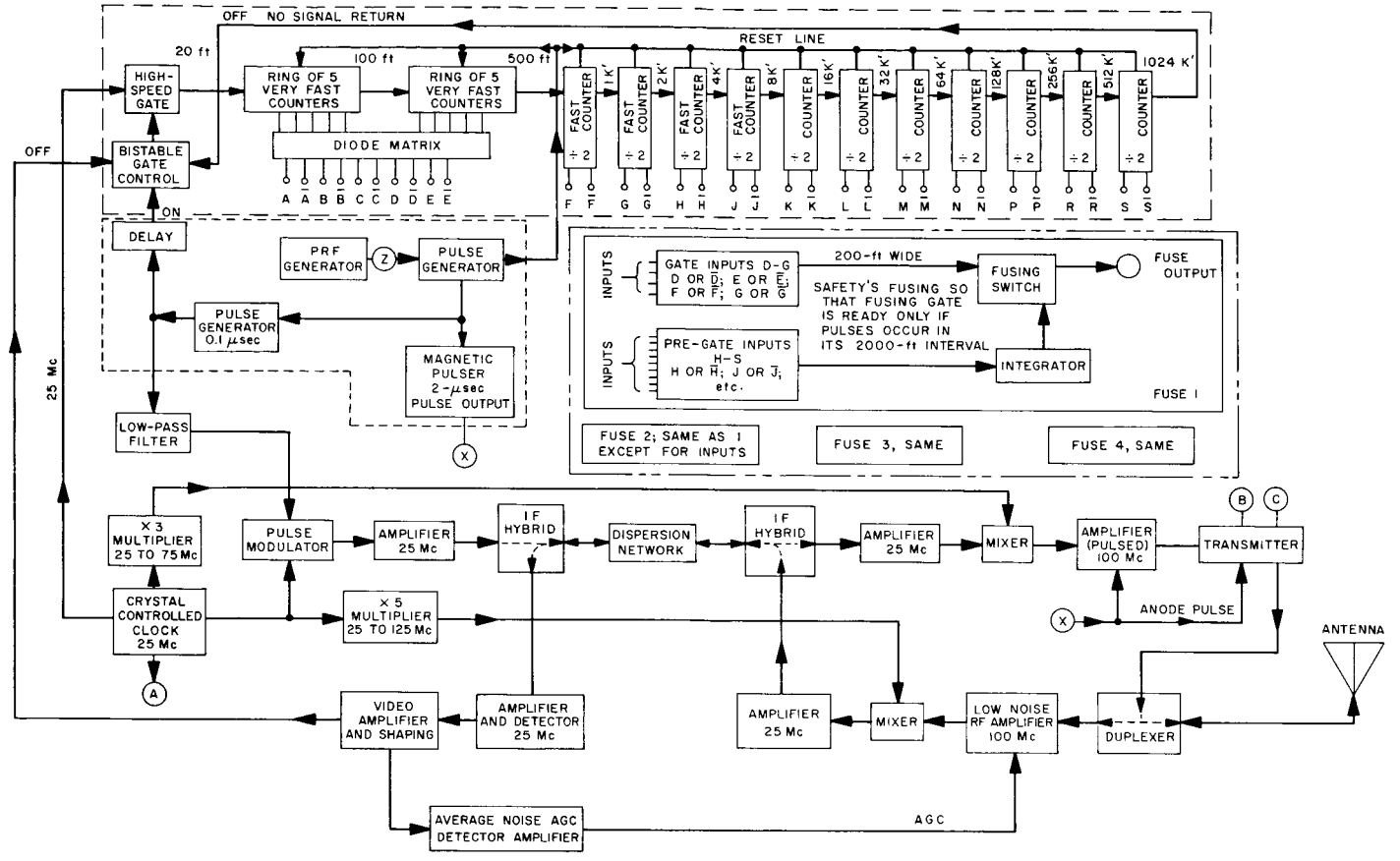

Fig. 3. Azimuthal pattern for notch slots with stubs

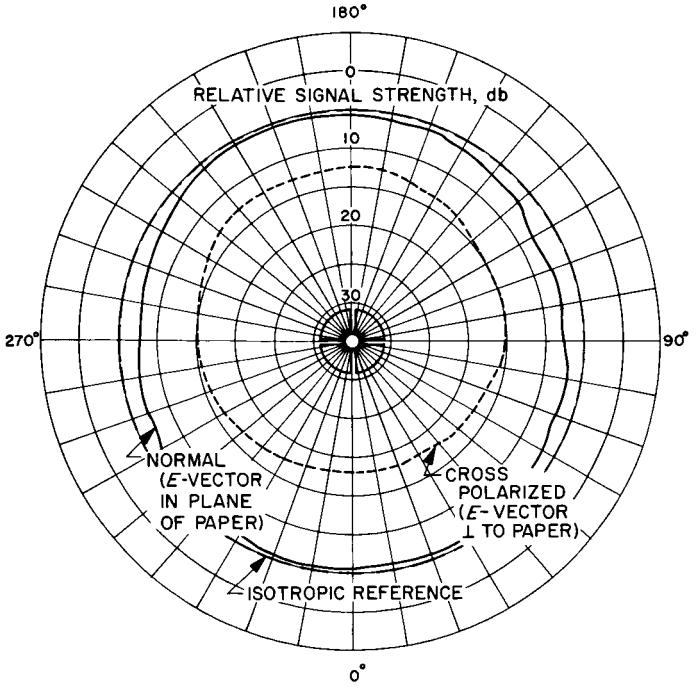

Fig. 4. Capsule altimeter block diagram

type of circuit comprises high-speed binary counters to operate from 1 Mc to below 100 kc. The third basic circuit consists of low-speed binary counters to operate from 100 kc on down. These can be integrated package units, such as those made by Fairchild and others, where the complete counter stage consists of one TO-15 or TO-18 transistor case.

A diode matrix is used to convert the 25-count output of the ring counters to five binary (or other) code outputs, so that the number of transmission channels is reduced. To complete the counting for ranges up to 10^6 ft requires eleven binary stages, resulting in a 16-bit numeric to denote the altitude.

The fuzing circuits consist of diode *and* gates using as inputs the output numeric from the time measuring section. The diode gate can be preset to any range measurement desired by selecting the proper phase of the counter outputs. The width of the fuzing gate is set by the number of inputs used. As an example, if the inputs from S to J inclusive are used, the width of the fuzing gate is

4,000 ft. If inputs from S to F inclusive are used, the width of the fuzing gate is 500 ft. The limit on the minimum width of the fuzing gate is set by the capsule velocity and the pulse recurrence frequency (PRF). With a 100-cps pulse repetition rate and a capsule velocity of 20,000 ft/sec, the minimum width of the fuzing gate will be 200 ft, since the capsule is moving 200 ft between each transmitter pulse.

For additional protection against false fuzing, the fuze *and* circuits are split into two sections: one the accurate fuzing gate, the second a less accurate pre-gate.

The pre-gate width can be substantially longer than the fuzing gate, allowing a number of transmitter pulses while the capsule is traversing its range interval. The pre-gate then opens for each pulse during this time interval. The output of the pre-gate is applied to an integrator, either analog or digital, which requires a number of input samples to reach a level sufficient to ready the fuzing gate. With fuzing gate readied, the pulse return that occurs at the fuzing altitude operates the fuze.

The additional complexity required to use a pre-gate is slight, and appears to be substantially outweighed by the advantages. Without the pre-gate, the possible false fuze time of the fuze link is the time required for the vehicle to reach fuzing altitude from altimeter turn-on. This time may be hours. With the pre-gate, the possible false fuze time interval is the time from operation of the pre-gate until the capsule reaches the fuzing altitude. This time may be as low as 1 msec. This is a false fuze time reduction of 10^7. The pre-gate width and integration time constant must be selected to give the maximum probability of operating when the capsule is in its range interval, with a minimum possibility of operating on a sequence of noise bursts. As an example, let us set the pre-gate width at 4000 ft and assume the vehicle is traveling 200 ft for every transmitter pulse. It is then possible to receive 20 samples during the pre-gate time interval. If the pre-gate integrator time constant is such that 10 pulses are required for operation of the ready line, adequate provisions have been made for missing pulses and scintillation. The probability of false signals reaching the pre-gate is determined by the threshold level of the video shaping, and is the same as the probability of false reading of any range in this time interval. The probability of 10 out of any 20 range measurements being false, and also occurring at the pre-gate selected time interval, is extremely low.

The optimum time interval integration time constant, and probability of false operation of the pre-gate, can be determined without much difficulty as part of the detail design problem when final system parameters are known.

The PRF generator is a 100-cps free running oscillator. Its output is shaped by the pulse generator and applied to the pulser (either magnetic or avalanche diode switched) and to the short-pulse generator. The short-pulse generator puts out a 0.1-μsec-wide pulse, which is shaped by the filter, and applied to the pulse modulator. The short-pulse generator output is also delayed and applied as the start input to the timer gate control. The pulser output is a high-power 2-μsec pulse which is applied to the pulsed power amplifier and output stage of the transmitter.

The output of the pulse modulator is a 0.1-sec pulse of the 25-Mc carrier. This signal passes through the IF hybrid and to the dispersion network. The output of the dispersion network is a 2-μsec pulse whose carrier is FM-modulated from 20 to 30 Mc. This signal passes through the second IF hybrid to the mixer amplifier. The other signal to the mixer amplifier is a 5/1 multiplied signal from the 25-Mc oscillator. The lower side band of the beat between the 125-Mc signal and the 20- to 30-Mc signal is amplified and goes to the 100-Mc driver amplifier. The 2-μsec-wide pulse output of the driver amplifier is applied to the grid of the transmitter tube. The transmitter output is a 2-μsec-wide pulse with 95- to 105-Mc FM carrier at a peak power of 2.5 kw. The transmitter output goes through the duplexer to the antenna.

The received signal from the antenna is directed by the duplexer to a low-noise 100-Mc RF amplifier. The output of the RF amplifier goes to a mixer where it is beat with a local oscillator signal derived by multiplying the 25-Mc oscillator signal by three. The lower side band of the mixer output is selected, giving a 25-Mc signal which is 2 μsec wide and FM modulated from 30 to 20 Mc. This signal is amplified and then goes through an IF hybrid and through the dispersion network. The dispersion network collapses the 2-μsec pulse to 0.1-μsec pulse length. The output of the dispersion network goes through an IF hybrid to the 25-Mc amplifier and detector. The output of the amplifier and detector is a 0.1-μsec-wide video pulse which is applied to the video amplifier and shaping circuits and the noise output from the detector goes to the automatic gain control (AGC) amplifier where an AGC is derived that sets the receiver gain for a constant average noise level. The video amplifier and shaper contain bandwidth limiting circuits and a threshold detector. A standard output pulse is generated. The standard pulse is used to close the fast-switching gate control resulting in a counter setting that denotes the altitude.

Glossary of terms:

- A path attenuation
- B receiver bandwidth
- C 3×10^8
- F receiver noise figure
- G antenna gain
- K planetary reflection coefficient
- P_r minimum detectable receiver power
- P_T transmitter peak power
- S/N signal-to-noise ratio
- T absolute temperature, °K
- h planetary altitude
- k Boltzmann's constant 1.38×10^{-23}
- λ operating wavelength
- τ pulse width

B. Spacecraft Design

Hard design of the *Mariner* B structure, temperature-control system, mechanisms, electronic packaging, hardware and cabling are proceeding. In addition, the study of the suitability of the *Discoverer* and *Nerv* as Mars entry capsules has been completed by the General Electric Co., Missiles and Space Vehicles Division. The following discussion summarizes the significant achievements in all of these areas.

It should be borne in mind that the first anticipated flight of *Mariner* B is a Mars opportunity and, while a primary design restraint is dual planet capability, emphasis has been on Mars requirements. Many design review seminars have been held during this period for the purpose of critically reviewing the design for functional adequacy, as well as reliability and dual planet capability.

1. Configuration

The *Mariner* B configuration drawing has been completed and released. Around this configuration (Fig. 5), the basic design is progressing. The drawing reflects most of the basic mechanical, structural, and dynamic interrelation between the spacecraft subsystems and serves as a building block for the design to follow.

The full-scale configuration mockup is continually being updated to reflect the spacecraft design as far as possible. Studies and tests are being conducted on operation requirements in areas such as: mid-course propulsion, attitude-control system installation, fixed and foldout solar panel handling techniques, and others. Preliminary cabling schemes are also being installed and studied on this mockup.

Most of the work on the 0.3 scale model has been completed. This model will serve for making antenna pattern measurements, planetary horizontal platform (PHP), and high-gain antenna look-angle studies. It will also be used to work out assembly, handling, and operational problems and serve as a design tool in general.

A study has been initiated to develop a more judicious use of the present telemetry system, whereby a more diagnostic analysis of the articulating members can be conducted. The number of measurements in conjunction with several actuation sequencing systems is being investigated.

2. Mechanisms

The design and analysis of the antenna gimbal system has progressed to a point where the final layout is nearing completion. Teflon sleeve bearings will be used for both pivots in either of two forms: (1) a reinforced Teflon liner which is comparatively rigid requiring initial clearance to allow for temperature differentials and manufacturing tolerances or, (2) a pure Teflon "zero slop" bushing of sufficient thickness to provide compliance to shaft and housing diameter changes without producing excessive rotation torques. Test hardware is being fabricated to determine which bearing concept should be used. Tests will determine required drive torque with temperature, load, and vacuum versus ambient pressure as variables.

The eccentric mass of the antenna elevation actuator about the azimuth axis will produce dynamic loads during launch in excess of the actuator and the antenna support and dish load capability. Since the elevation axis does not need to be latched, the present design provides a mechanical interlock so that the release of the azimuth axis is accomplished by a rotation of the elevation axis. However, another latch scheme is being sought to eliminate this azimuth dependence on elevation since com-

munication is possible with azimuth only (and spacecraft roll) over a large portion of the mission.

A turntable/torque meter with a ±150-deg rotation range has been fabricated and instrumentated for the cabling group to determine the cable bundle resistance torques at rotary joints for the expected flight environment.

The Mars PHP configuration has not been completely defined. However, most of the conceptual decisions on the design have been made. The instrument support structure will be a closed box which will provide a hard-mount single-surface interface for each instrument. Any provision for thermal or mechanical isolation of instruments will be part of the instruments. The swivel axis and the scan axis will be coaxial, providing better space utilization in the PHP bay and a greater possibility of uniformity between Mars and Venus missions. The launch latching scheme will be nonredundant with a minimum number of pin pullers (probably three) that will be released immediately after injection. The release of the A frame at planet encounter will be accomplished by the initial rotation of the hinge axis, which will release a mechanical latch. Deployment of the A frame through an angle of less than 90 deg is being considered to take advantage of possible improvements of the view window with respect to the spacecraft.

A single direct-operating linear actuator has been chosen to deploy each of the solar panels and the antenna as a result of layouts and analysis of several competitive arrangements. The type of dampening device has not been chosen. An oil dampener would be the simplest, although the possible contamination of other spacecraft items due to an oil leak is being investigated.

The launch latch releases are being designed on the basis of using *Ranger*-type pyrotechnic pin pullers of a larger size (since the loads are beyond the capability of the *Ranger* puller). The prototype for an alternate latch that is triggered by the change in ambient pressure after launch will be developed as a backup. A work statement has been issued to several vendors to bid on furnishing the design, fabrication, and testing of such a latch.

3. Structural Design

Detail structural design is progressing with some components now in early stages of fabrication. The basic spaceframe structure components are nearing design completion. The basic structure is to be fabricated from aluminum alloy. The first billet, from which the large center ring will be machined, has been forged and is in inspection.

As the spaceframe design nears completion, more detailed layouts are being made of the interfaces with the equipment to be attached to it. The spoke detail, including the fixed solar panel attachment, must be insulated from the primary structure. These details, utilizing fiberglass, are being designed and will be structurally tested as soon as possible.

The end of the spoke to which the fixed and foldout solar panels attach is a busy corner. Fitting attachments, an attitude-control jet and the panel-hinge fitting meet at this point. A layout to work out the details of clearances and assembly is now in progress. Completion of this work will permit the general outrigger design to continue. Figure 6 shows a model of this area. Cabling will be mocked up on this model to help solve the problem of getting cables across the solar panel hinge interface.

The layout for the upper support for the solar panel has been completed and the parts are being detailed. The latch structure is being designed with interchangeability of pyrotechnic pin pullers and vacuum-actuated pin pullers in mind. The low pulling capability of the latter type presents a problem. Calculations of loads due to possible thermal conditions show the pins to be more highly loaded than permissible at actuation. A device is being designed which will permit the thermal displacements to take place, but which will maintain the truss rigidity for dynamic loading. The success of this, or a similar device, is required to maintain this desired interchangeability of pin-puller devices.

Two 4-ft-diameter high-gain antenna reflector contracts have been processed. The basic configuration of each design is the same. The materials and fabrication techniques are different. The first is a bonded aluminum sandwich. The reflector surface will consist of a vacuum-formed aluminum foil. The core is to be machined from ¼-in. aluminum core. The second is an all-fiberglass sandwich, and the reflector surface will be vapor-deposited aluminum.

An explosion-formed and chem-milled aluminum dish is being supported by a separate process contract. It is expected that these dishes will be available for comparison with the above two reflectors. Structural, thermal, electrical, and space environment tests will be conducted on these designs to select one for use on the vehicle.

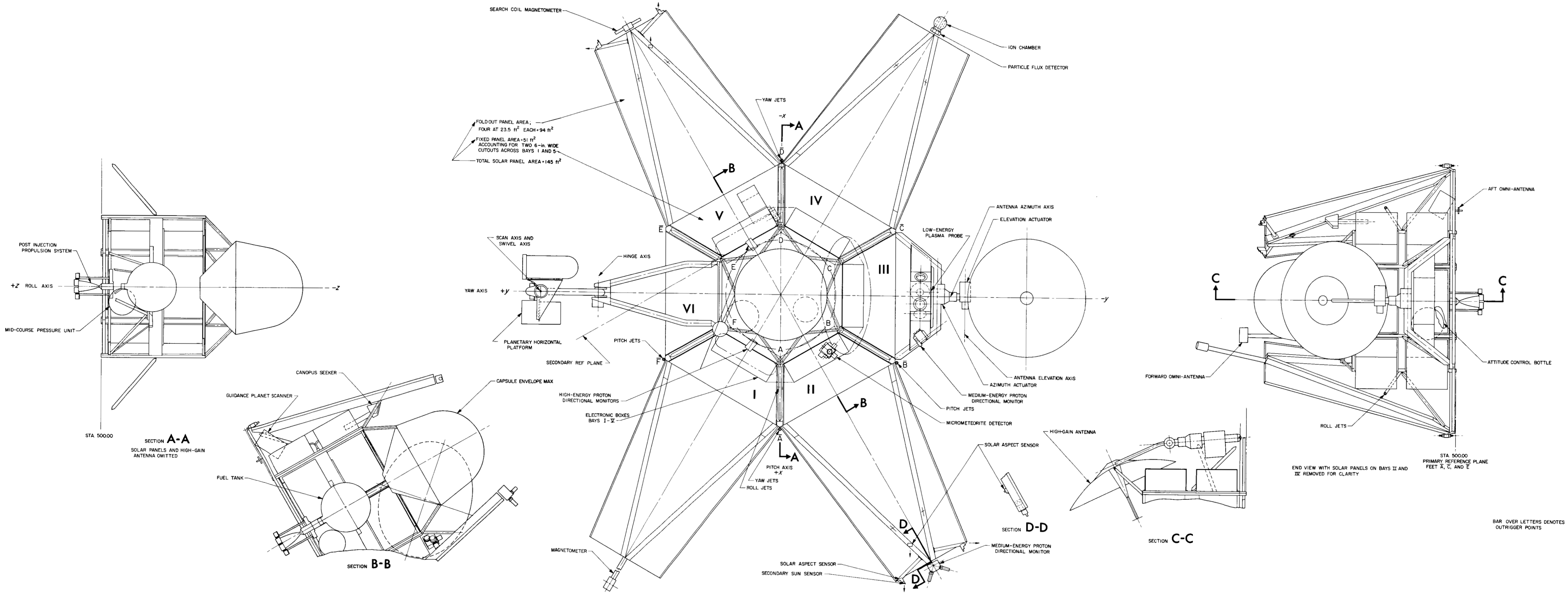

Fig. 5. *Mariner* B spacecraft configuration

The solar panel structural design is nearing completion. A full foldout panel is to be delivered in late summer for testing.

Two test modules having the same geometry as the lower module of full panel have been fabricated and tested. Results of the testing of the first module were reported in *SPS 37-15*. This module was failed during dynamic testing. A second module with 0.008 strips added to the corrugation caps was tested both statically and dynamically. Solar cells were bonded on the rest of the panel. Ultimate static bending moment was applied to the beam without buckling the skin. The bonded cells stabilize the skin at the ultimate load (Figs. 7, 8, and 9).

A modal analysis on the second module showed the frequencies and mode shapes to agree with the analysis.

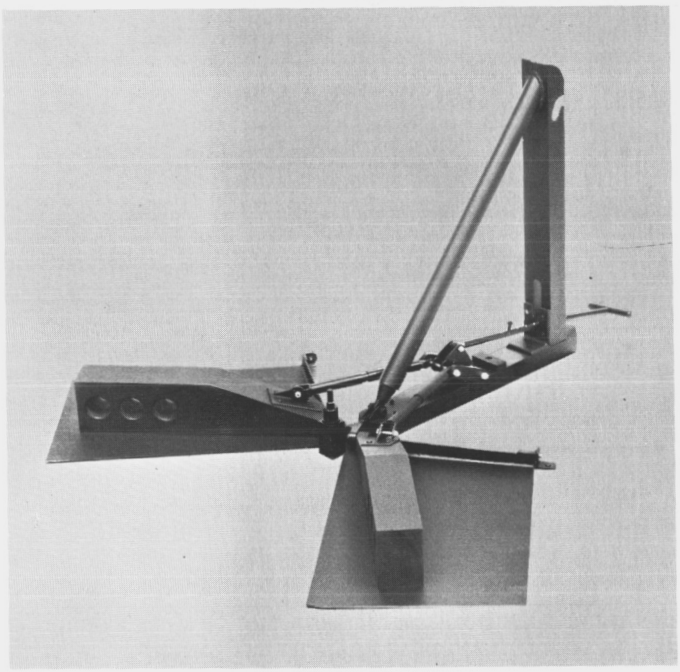

Fig. 6. Solar panel hinge model

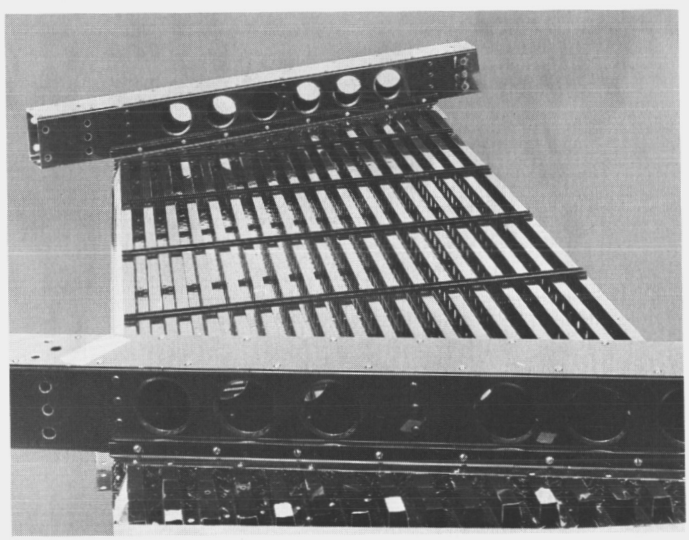

Fig. 8. Solar panel test module, bottom view

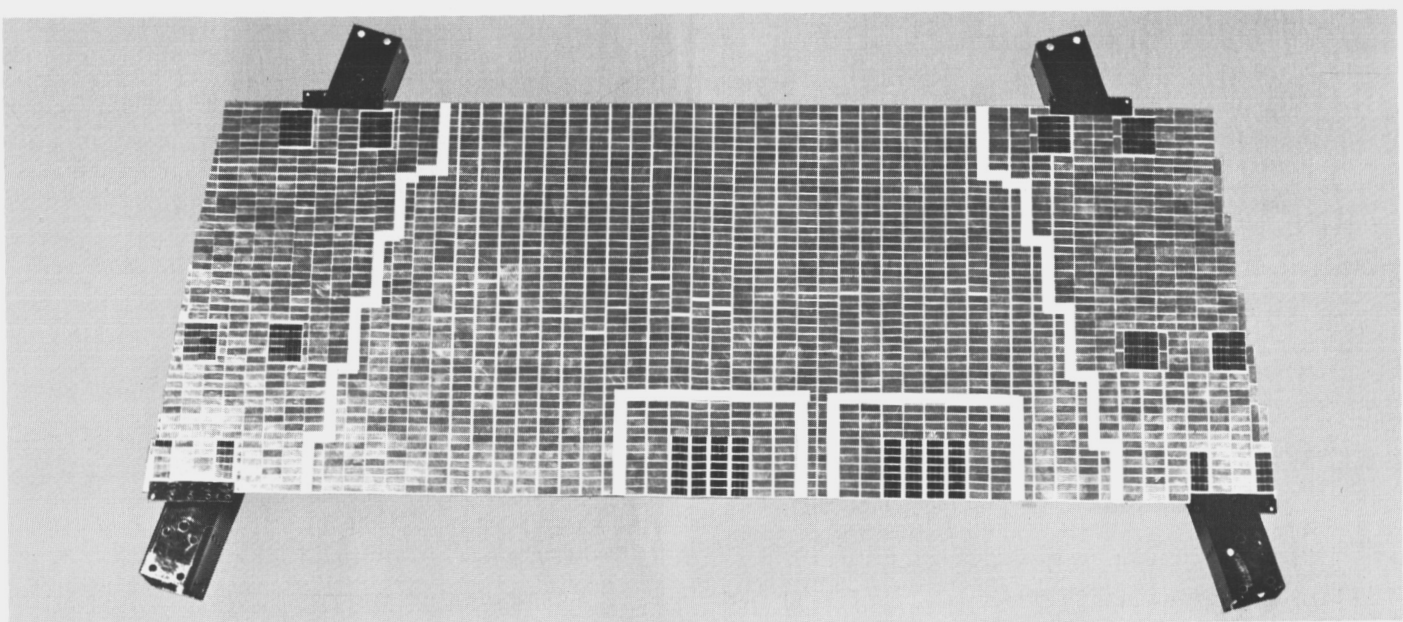

Fig. 7. Solar panel test model

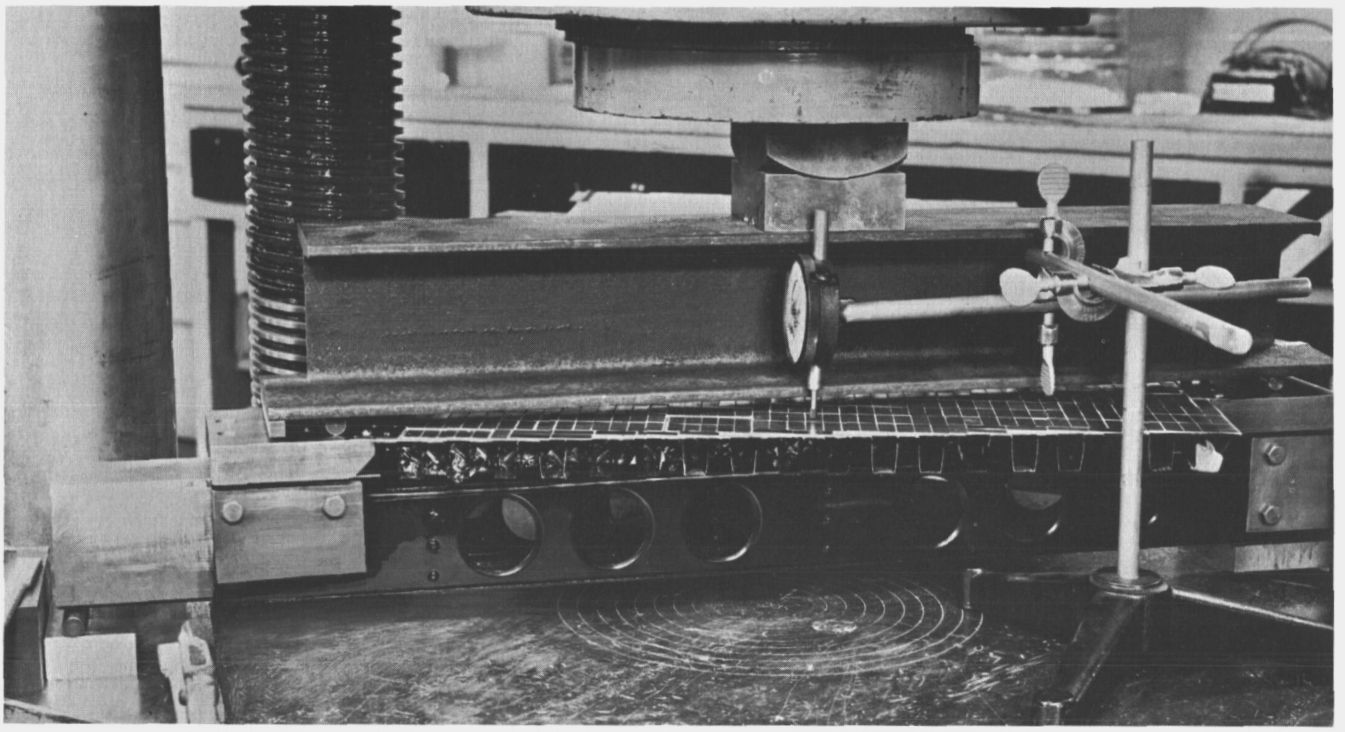

Fig. 9. Solar panel beam static test

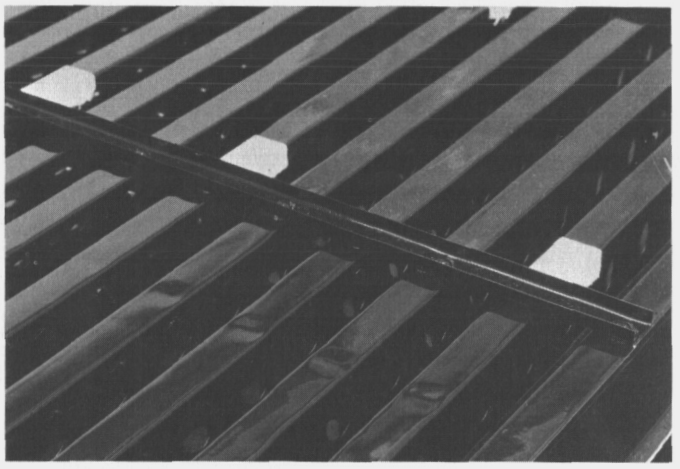

Fig. 10. Solar panel buckled corrugation

The damping coefficient was measured to be 1.06%.

The module was vibration tested with the loading input being increased in each test run until the point of failure was reached. At 1.5-*g* rms input to the fixture, the corrugation buckled at the end of the cap stiffener (Fig. 10). At this input, a transmissibility of 43 was measured at the critical point on the module when simply supported. Calculations which compare the module to the full panel show that this input of 1.5 *g* rms is equivalent to 3.68-*g* rms input to the full panel assuming the same damping coefficient of 1.06% as measured in the modal analysis.

These static and dynamic tests show that the solar panel design is adequate; fabrication of a full panel has begun.

The fixed-panel design has been started. These panels attach directly to the spaceframe spokes and to the lower spaceframe ring through a fiberglass attach angle. The panels are of sandwich construction and use the same corrugation as on the foldout panels. Tests will be conducted on the first panels which are to be delivered in late summer.

4. Temperature Control

a. Bus. Primary emphasis on the bus-associated equipment has recently been focused on the following areas:

(1) Parametric study on a representative electronic package (still in process).

(2) Definition of temperature extremes for miscellaneous external actuators, supports, pin pullers, and antenna structures (still in process).

(3) Generation of an integrated flight temperature telemetry plan.

(4) Analytical investigations on the space science equipment.

(5) Definition of the aerodynamic heating effects.

On previous spacecraft, flight temperature telemetry has always been inadequate to allow proper evaluation of spacecraft temperatures during flight, especially nonstandard flight. To this end, 60 temperature sensors will be flown on *Mariner* B. These 60 will be so placed as to provide a minimum of four sensors per hex bay and direct monitoring of all critical power, guidance, communications, and science instruments. The sample rates are so chosen as to allow complete coverage of all maneuvers and acquisitions at sample intervals well within the time constant of the particular component. It is felt that this number of temperature measurements represents the minimum number to allow required in-flight calibrations, subsystem performance evaluations, and failure analyses when necessary.

b. Science instruments 21–33. Table 1 contains current estimates of mean operating temperatures for science instruments 21 through 33. These estimates represent steady-state temperatures of the instruments when the spacecraft is in the sun-oriented, cruise mode. The range covers temperatures from Earth through Mars and is based on the 1964 Mars mission. The range is for average temperatures and does not include uncertainties in radiating area, surface properties, etc. Except for instruments 21, 24, 30 and 32, the temperature values are the results of a detailed study on an IBM 7090 computer.

To date, no serious thermal problems of a general nature are expected when the spacecraft is in the Sun-oriented cruise mode, unless the thermal-control solutions for the steady-state and the transient periods are irreconcilable. However, some detail problems do exist. The sensitivity detectors on instruments 27 and 29 can be drastically affected by the choice of surface treatment and, to date, no entirely compatible surface treatment has been found. Instruments 28 and 29 tend to operate near their lower temperature limits because of their low internal power dissipation density and physical configuration, and therefore may exceed their limits when uncertainties are considered.

Currently, temperature transients produced by non–Sun-oriented spacecraft maneuvers are being investigated; however, it is too early to report any conclusive results. Investigations of shroud heating effects during boost, from liftoff to shroud jettison, indicate that aerodynamic heating of the shroud has little effect on the instruments. It is expected that shroud heating will not produce more than a 20°F temperature rise.

c. Heating of science instruments during the period between shroud jettison and second Centaur *firing.* To determine if the science instruments mounted on the solar panel (Units 26, 27, 29 and 33) will thermally survive during the period between shroud jettison and the end of second *Centaur* firing, a theoretical study was performed. In this respect the maximum temperatures which the instruments will attain due to aerodynamic, direct solar, reflected solar, and terrestrial heat inputs have been estimated and are reported in Table 6.

The results for this preliminary study indicate that Unit 26 will probably survive, Unit 27 will be marginal, and the remaining instruments, especially the detectors, will experience temperatures which will be greater than the respective permissible values.

Two alternatives were proposed in order to eliminate the overheating. First, a time delay in shroud jettison

Table 6. Temperature estimates

Unit	Cruise mode		Shroud jettison through injection		
	Mean operating temperature range, °F	Operating temperature spec. °F	Computed maximum temperature, °F	Storage temperature specified, °F	Remarks
21	0 to 50	−40 to 121			
23	−5 to 60	−58 to 77			
24	50 to 150	−40 to 194			
25	35 to 160	−4 to 212			
26	−25 to 160	−58 to 256	210	302	O.K.
27	−5 to 110	−22 to 167	205	212	Marginal
27, Detector			320[a]	212	–[b]
28	−20 to 95	−22 to 149			
29	−20 to 80	−22 to 149	256	212	–[b]
29, Detector A			360[a]	212	–[b]
29, Detector B			752[a]	212	–[b]
30	50 to 100	−22 to 149			
32	50 to 100	−22 to 185			
33	−15 to 130	−99 to 185	257	212	–[b]

[a] Only aerodynamic heating was considered; direct solar, reflected solar, and terrestrial heat inputs were neglected.
[b] Exceed temperature limit.

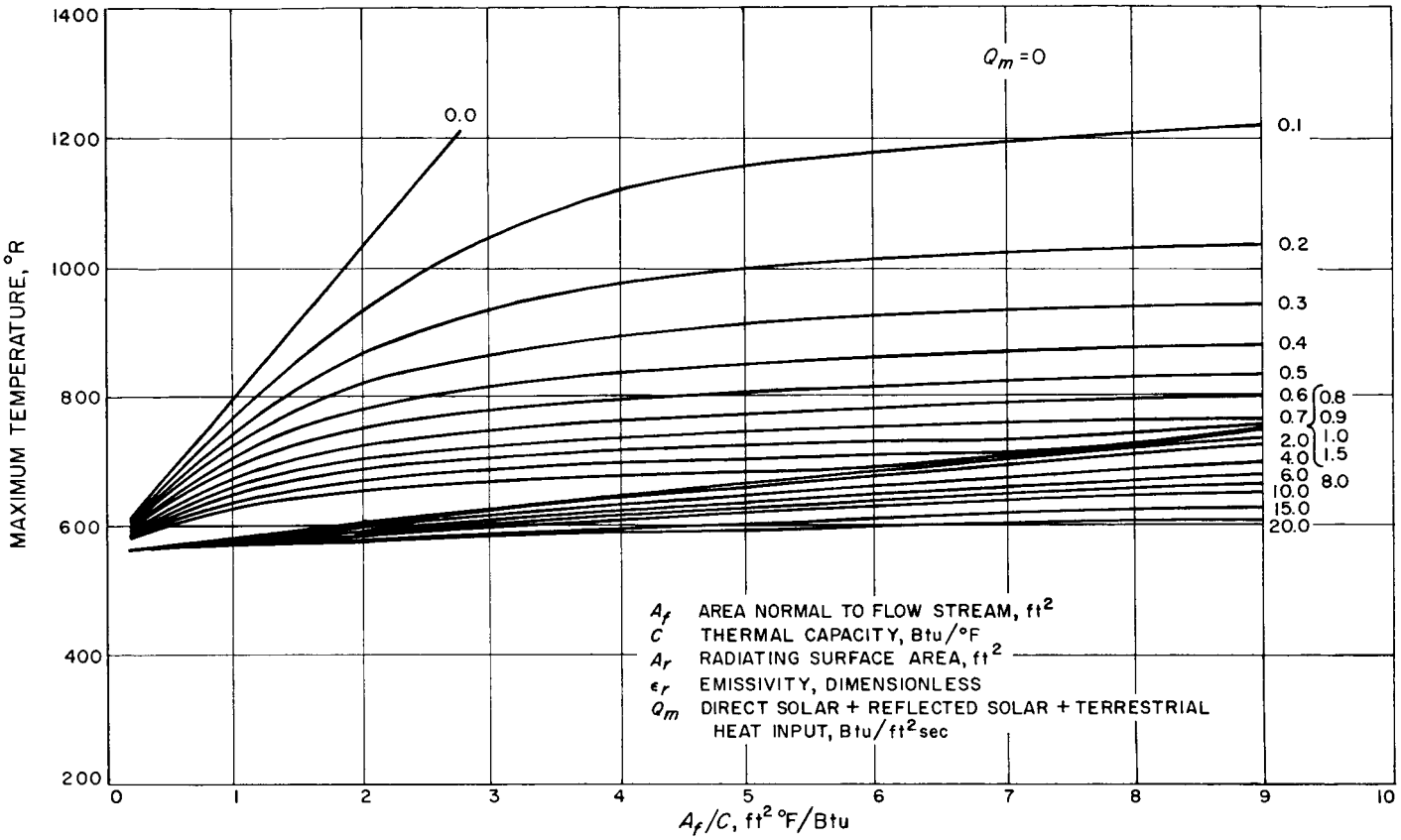

Fig. 11. Maximum temperature versus A_f/C

was considered. The investigation disclosed that the temperatures would not be sufficiently reduced within the allowable time limits on shroud jettison. The second alternative was to provide thermal protection, such as thermal shielding to reduce heat inputs, increasing the thermal time constant by altering surface radiation characteristics, increasing the thermal capacity, etc. This technique is proposed to be more expedient and, perhaps, more assuring in resolving the overheat problem. However, the design difficulties imposed by the various types of thermal modifications, as yet, have not been investigated. The effects of altering the surface radiation characteristics in order to reduce the maximum temperatures are presently being studied.

For the analysis, the instruments were treated as a single lumped capacity with no heat exchange with the spacecraft proper. The aerodynamic heat input was based on inertial velocity (nominal) and on a trajectory which is 12 km lower than nominal in altitude. The remaining inputs were time-averaged and assumed constant for the entire flight period under consideration. The instrument temperature at the time of shroud jettison (220 sec from launch) was assumed to be 560°F.

The study was performed parametrically, in order to facilitate computations and to provide some insight on the temperature response of the instruments for the heat inputs considered. Five graphs similar to that shown as Fig. 11 were formulated and with these graphs the temperatures in Table 6 were estimated.

5. Materials and Methods

Present thermal control requirements dictate the use of a low thermal conductance material to tie the solar panel radial spokes to the vertical columns of the *Mariner* B bus. Structurally, these fittings must have a tensile strength of about 25,000 psi.

Available materials fall into two classes: (1) laminated reinforced plastics, and (2) molded, randomly oriented reinforced plastics. The former can develop tensile strengths of 50,000 psi, but are not suitable because of the complex geometry of the fitting, while the latter normally develop tensile strengths of 5,000 to 10,000 psi.

Therefore a need exists, not only for this *Mariner* B fitting, but also for future applications for a process which will bridge the gap between the low-strength

molded and the high-strength laminated products. A search of manufacturer's literature uncovered a few materials that promised the required strength in a molded product. However, a careful reading of the footnotes revealed that the tests were run on molded plates and are presumed to be very unconservative.

Two approaches will be taken by the materials and methods group to develop a high-strength molded fitting:

(1) A suitable matched-metal mold will be fabricated and several test parts will be produced by high-pressure molding techniques, using randomly oriented material.

(2) A preform made from laminates cut to specific patterns will be constructed and finish-molded under high pressure in the mold described in approach (1).

6. Capsule

General Electric Co.'s Missile and Space Vehicle Department has completed its study on the Suitability of the *Discoverer* and *Nerv* Entry Vehicle for Mars Atmospheric Entry. The assumptions used in the study were furnished by JPL and were based on the use of such vehicles in combination with the *Mariner* B spacecraft, and on the best known characteristics of the Martian atmosphere. The general conclusion was that the *Discoverer* and *Nerv* vehicles would, with a minimum of modification, meet the performance requirements for the Mars entry vehicle.

The following table describes a few of the gross characteristics of the vehicles studied, and succeeding paragraphs briefly discuss the areas investigated and the modifications required.

Characteristic	*Discoverer*	*Nerv*
Gross weight, lb	198	66
Payload, lb	70	20
Diameter, in.	32.7	19
Mach No. for initial parachute deployment	2.2	2.2
Final parachute deployment altitude, ft		
Atmosphere A[a]	13,000 to 50,000	13,000 to 50,000
Atmosphere C[a]	45,000 to 60,000	45,000 to 60,000
Parachute descent time, min.		
Atmosphere A	3.7 to 16	3.7 to 16
Atmosphere C	18 to 27	18 to 27

[a] Atmosphere A refers to that combination of possible atmospheric characteristics which gives the lower bound for parachute deployment. Atmosphere C similarly provides the trajectory which yields peak heating rate.

The aerodynamic performance of the *Discoverer* shape was analyzed as to force coefficients, pressure and load distributions, stability at angles of attack from 0 to 180 deg, and so on. A spherical segment afterbody had to be added to the study vehicles to ensure backward instability. Although the dynamic stability of the modified configuration appears marginal at near-zero angle of attack, the 6-deg-of-freedom trajectories, where density effects are included, show no divergence of oscillations.

Both point mass and 6-deg-of-freedom trajectories were studied to determine the time histories of axial deceleration, velocity, and altitude and the resultant aerodynamic effects on the *Discoverer* shape. Various entry conditions were used to describe some of the more pertinent situations. Spin rates of 0 to 10 rpm, tumbling rates up to 4 deg/sec, angles of attack up to 180 deg, and entry path angles from minimum capture to direct entry, were the parameters and their ranges. For these initial conditions, large angles of attack are not likely to be a problem. The worst structural loads occurred with direct entry where, at zero angle of attack, the axial loads approached 125 Earth g. On direct entry, with an angle of attack of 180 deg and small pitch rate, maximum combination of loads occurs with 106 Earth g axially and 94 Earth g transverse.

The deceleration system presently used on the *Discoverer* and *Nerv* capsules cannot meet the mission requirements. A detailed analysis of the modifications required and of possible deployment sensing systems was therefore presented. State of the art for parachute deployment was set at Mach 2.2. Various parachute types, configurations, and stages were investigated with the following scheme ultimately proposed. The aft heat shield cover of the capsule is ejected backward through the wake. This extracts a small pilot chute, which in turn extracts the supersonic first-stage parachute of the Fist Ribbon type and Equiflo or Hemisflo design. After 3 sec, the first stage is released from the capsule and extracts the main parachute in a reefed condition. After 2 sec, the main chute, which is of Ring Sail design, opens fully. The sensing scheme utilized both a baroswitch and a G-switch. Inputs are required from both sensors before the programmer will provide the start command.

The temperature control scheme must be compatible with four different flight conditions. These would be: (1) the initial boost and flight phase with the capsule on the spacecraft, then (2) a coasting period of up to 180

days, (3) the entry phase into the Martian atmosphere, and lastly (4) the period of parachute descent. An α/e coating system was employed in conjunction with solar cells. The latter are used during the coasting phase where a low power input is required to maintain battery temperature. From consideration of the thermal shield temperature gradient, the inside of this shield will have a 0.020-in. thick magnesium liner bonded to it. To prevent too low a shield temperature, a high emissivity coating ($e \approx 0.9$) on the inside of the shield is desirable. The capsule temperature should be maintained between 14 and 160°F. To do this, an α/e coating on the outside of the vehicle is necessary. The ratio will vary over different parts of the surface from 1.86 to 2.46 and will be achieved by use of a rhodium coating with patches of black paint. Upon consideration of the thermal pulse during entry, an emissivity of this coating of 0.05 or less is necessary.

The heat shield of the *Discoverer* consists of an outer shell of phenolic nylon bonded to an inner layer of laminated phenolic glass. The aft end of the structure is a fiberglass dome. The shield is supported internally by four reinforcing rings. The capsule assembly which fits inside this shield is an aluminum spun shell with intermediate ring stiffeners. The present *Discoverer* vehicle appears to be structurally sound for the proposed mission. The system was analyzed as to all loading conditions, thermal, vibration, shock, bus separation, and the margins of safety indicate adequacy for the design requirements.

Other areas covered briefly were an antenna design, sterilization, weight and balance, component and system testing. The general conclusion drawn from the investigation is that the *Discoverer* with some modification is suitable for a Mars atmospheric entry.

C. Guidance and Control

1. Secondary Power

a. Mars solar cell electrical power supply. The solar cell electrical power supply for the Mars *Mariner* B spacecraft is presently designed to utilize 141 ft² of solar-panel area. Approximately 57,000 1- by 2-cm silicon solar cells can be mounted on such an array. Approximately 37,000 cells will be mounted on the four foldout panels; the remainder are mounted on the body-fixed panels. Cells mounted on the foldout panels will operate at a lower temperature than those on the body-fixed panels. The effect of the temperature mismatch on the electrical matrix has been investigated.

b. The effect of temperature on matching. The temperature difference between body-fixed and foldout panels requires that a greater number of cells be used in series on the body-fixed panels than on the foldout panels. A mismatch in maximum power voltages of the two types of panels at Mars where power is critical would cause a reduction in the vehicle's power capability.

Figure 12 shows the panel temperatures as a function of solar intensity for four different sets of thermal parameters. These curves were calculated assuming maximum power point operation and no degradation. (Previous analyses have shown that there would be about a 4°C increase in panel temperature in going from full load operation to half load. The error in operating temperatures due to these two assumptions should be less than 4°C at Mars encounter.) Figure 13 gives the ratio of the maximum power voltage per cell on a foldout panel to that on a fixed panel as a function of time for the two extremes of thermal parameters (i.e., cases 3 and 4 of Fig. 12). In order for the maximum power voltages of the two types of panels to match at Mars, the ratio of the number of cells on the body-fixed panel to that on the foldout panel should be between 1.12 and 1.19. The loss in power from assuming a ratio of 1.12 when it should have been 1.19 is less than 1%.

c. Panel voltage characteristics. Even though the power capability of the Mars solar panels varies greatly during transit due to intensity, temperature, and radiation effects, the voltage characteristics of the panels are reasonably stable. Figure 14 shows these characteristics. The maximum power voltage of the panels can be expected to vary ±10% during cruise. The operating voltage of the panel for the relative constant power cruise mode should only vary about ±7%. It does not now appear that there will be any problem in dissipating excess power in the panel shunt regulators (i.e., zener diodes). The shunt regulators would only be required to dissipate power after injection and mid-course maneuvers when the solar panels are very cold.

d. Temperature-intensity test. A testing facility is being set up to study the characteristics of solar cells over a temperature range −100 to 150°C and up to intensities of greater than five Suns. For the low-temperature tests the cells will be mounted in a vacuum chamber to prevent frosting. A 1.6-kw xenon light source system will be used

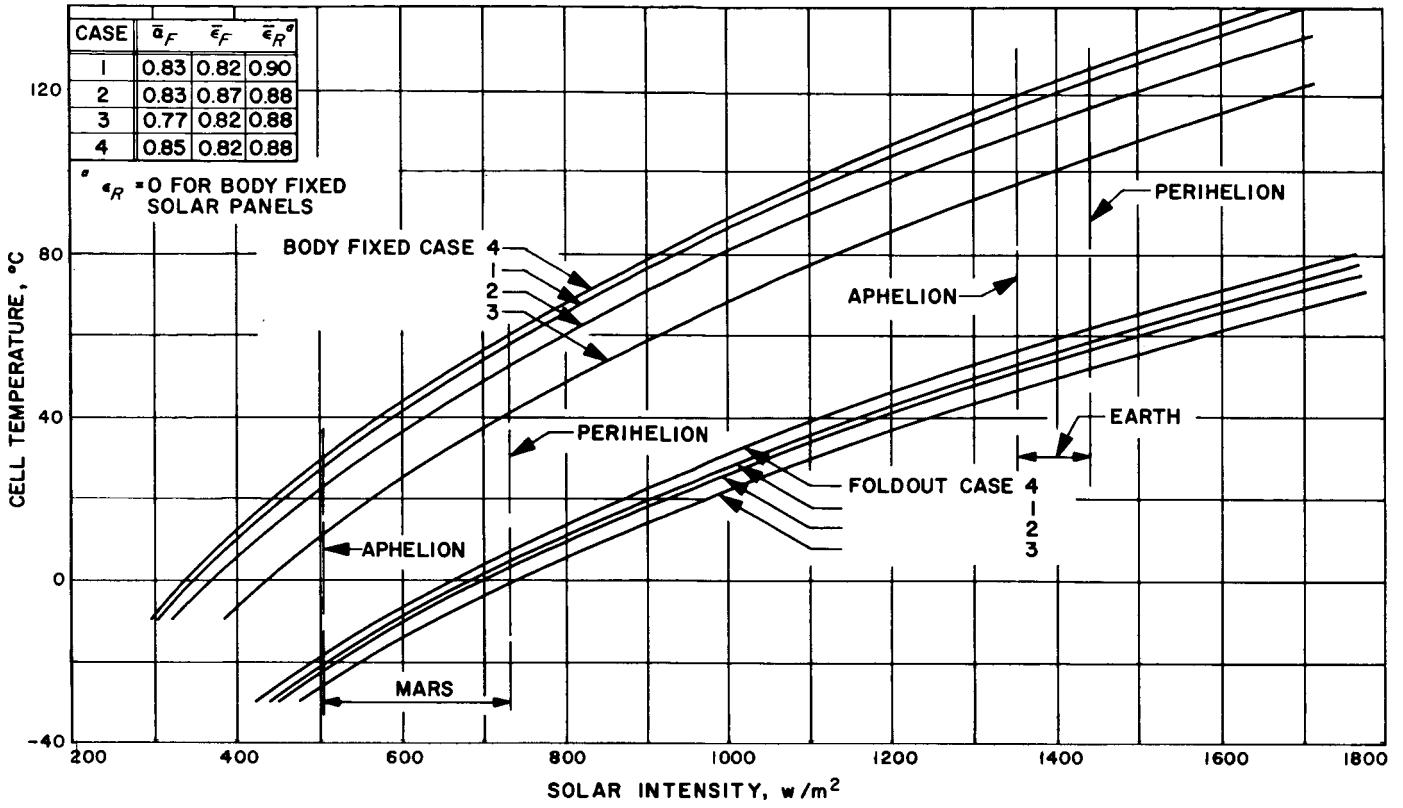

Fig. 12. Panel temperature as function of solar intensity

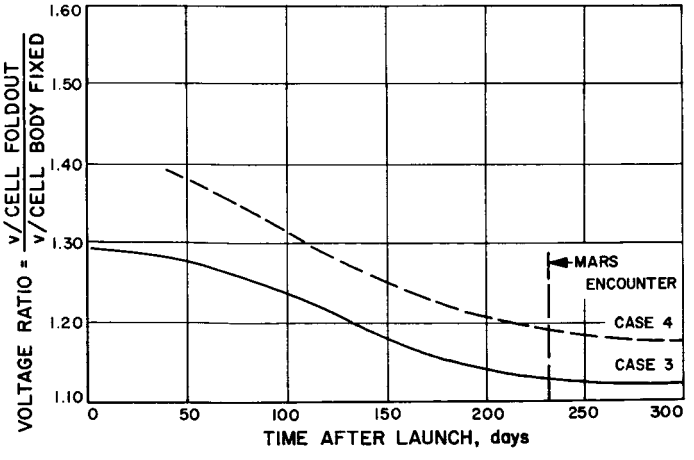

Fig. 13. Ratio of foldout versus fixed panel cell voltages

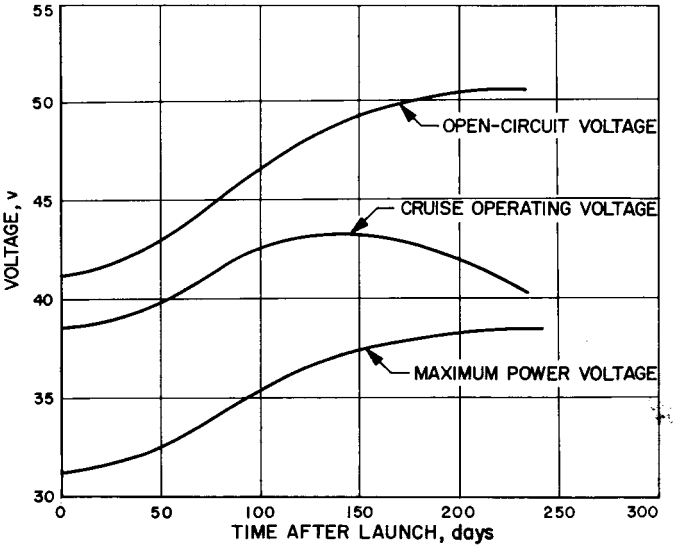

Fig. 14. Mars solar panel voltage characteristics

to irradiate the cells. An infrared absorbing visible transmitting filter will be used with the raw xenon source to minimize the "tungsten" effect in the temperature characteristics of the cells. It is anticipated that these tests will provide data that will make it possible to predict more accurately solar-panel performance on interplanetary missions.

e. Radiation damage to solar cell power supply. Since the discovery of severe electron and proton radiation in Earth-space and interplanetary space, the effects of radiation to different materials have provided the basis for many extensive investigations. Among these is the inves-

tigation of electron and proton radiation damage to semiconducting materials and semiconductor devices. Of particular interest is the effect of radiation on solar-cell power supplies for use in spacecraft. The approach to the problem of solar-cell radiation damage has been along three separate paths: (1) the investigation of solar cell damage in the laboratory, using radiation (both electron and proton) whose energy and flux density is known, (2) the evaluation of the radiation environment (with regard to particle energy and flux density) encountered in space, and (3) the monitoring of radiation damage to actual solar-cell arrays or single solar cells in space with telemetry data.

Laboratory measurements of solar-cell radiation damage have been performed by the following organizations:

(1) Space Technology Laboratory: study of damage resulting from electron radiation between 500-kev and 1-Mev energy and high-energy proton radiation (up to 700 Mev).

(2) Radio Corporation of America, David Sarnoff Research Center: measurements with electrons below 2 Mev and with 8.3-Mev and 19-Mev protons.

(3) Bell Telephone Laboratory: study of damage resulting from 1-Mev electrons and 18-Mev to 500-Mev protons.

These measurements have been performed on silicon cells of both the P-N and N-P types. Silicon P-N solar cells are being used for both the *Ranger* and *Mariner* R solar panels. On the basis of the above laboratory measurements it appears that N-P type cells are more resistant to radiation damage than are the P-N type, but just how much more resistant is not accurately known. Measurements thus far indicate a large spread in damage rates in seemingly identical solar cells. It is believed that the impurity content of the parent material is a possible key to the quantitative evaluation of the radiation damage. In spite of the varied results, the data obtained to date can be of significant value in evaluating the possible damage to solar-cell power systems in space. However, in order to make use of the laboratory data, the radiation environment encountered in space must be known.

For convenience, the radiation in space may be classified as follows:

(1) Van Allen radiation: consisting of electrons and protons of wide energy ranges which are trapped by the Earth's magnetic field. This region surrounds the Earth in a toroidal manner with symmetry about the geomagnetic equator and extends to about 30,000 to 40,000 mi above the geomagnetic equator.

(2) Deep space radiation: consisting of all radiation encountered beyond the Van Allen radiation zone. Immediately beyond the limits of the Van Allen belt is a region of about 12,000 mi in which there is a large amount of magnetic turbulence and in which the radiation environment is very unstable. Beyond this region several types of radiation are encountered:

   (a) Galactic radiation: light and heavy nuclei originating from the stars and other cosmic bodies.

   (b) Solar X-rays: X-rays emanating from the Sun, usually during high solar flare activity.

   (c) Solar electrons: an electron plasma which originates from the Sun and is usually of greatest abundance during solar flare activity.

   (d) Solar protons: large bursts of protons (1 Mev to 10 Bev) which are usually the product of a large solar flare.

For an Earth satellite, the Van Allen radiation is of greatest significance. However, for an interplanetary spacecraft, the radiation in deep space is greater in importance. Table 7 is an outline of some radiation damage data received from Earth satellites operating in the Van Allen belt.

Explorer VI spent most of its time in the outer regions of the Van Allen belt. In this area mostly electrons exist. The total number of electrons seen by *Explorer VI* exceeded the total number of protons by a factor of 10^4. *Explorer XII* was able to detect low-energy protons (120 kev $< E <$ 4.5 Mev). This was the first time that such low-energy protons were observed in the Van Allen belt. The relative abundance of such radiation is revealed by the quite large total flux of 5.4×10^{10} protons/cm^2 seen by the spacecraft during the first three days after launch. This flux far exceeded the electron flux encountered during the 3-day period.[a] Both *Transit* 4B and *TRAAC* were confined to the inner region of the Van Allen belt.

[a]The *Explorer XII* data show a large difference in the damage rates between uncovered cells and covered cells. A glass cover as thin as 0.003 in. gave enough protection from the proton radiation to provide for no degradation in the glass covered solar cells, while a 50% degradation was observed in the bare cells. These results are reasonable since a glass cover 0.003 in. thick should be able to stop protons whose energy is less than 4.5 Mev.

Table 7. Van Allen belt radiation damage to Earth satellites

Spacecraft	Power Degradation, %	Days in orbit	Total radiation flux	Type of solar cells	Apogee[c]	Perigee[c]
Explorer VI	27	18	7.5×10^{13} electrons/cm^2 ($E > 200$ kev)	silicon P-N bare	26,500	130
Explorer XII	50	3	5.4×10^{10} protons/cm^2 (120 kev $< E <$ 4.5 Mev)	silicon P-N bare	47,627	481
	0	3	(120 kev $< E <$ 4.5 Mev)	silicon P-N, 0.003-in., 0.020-in., 0.006-in. glass covers		
Transit 4B	7.2	55	8×10^{10} protons/cm^2 ($E > 4$ Mev)	silicon P-N, 0.006-in. glass cover, 0.420 micron filter[a]	689	593
TRAAC	13.2	81	10^{11} proton/cm^2 ($E > 4$ Mev)	silicon P-N, 0.006-in. glass cover, 0.450 micron filter[b]	694	589

[a]The 0.420-μ filter reflects 50% of the light with wavelength less than 0.420 μ while transmitting 90–95% of all electromagnetic energy of longer wavelength.
[b]Same as above, with 0.450 μ wavelength.
[c]In statute miles.

In this region, protons rather than electrons are predominant. On the basis of the data in Table 7, it is obvious that radiation damage to solar cell power supplies is a very significant problem.

In order to evaluate the probable damage to the *Mariner* B solar-cell power supply, it is necessary to have a knowledge of the deep space radiation environment. Of all the components of deep space, radiation solar protons present the largest hazard to solar cells. As has been mentioned, there seemingly is a connection between solar-proton radiation and solar-flare activity. Solar protons have been observed to appear in bursts following the commencement of a significant solar flare (class 2 or greater). Solar proton bursts have been observed with a maximum flux density of 10^4 protons/cm^2-sec. Such events have been known to remain at maximum intensity for about a day and then decay with a time t dependence of t^{-2} to t^{-3}. The duration of an event can be for a total of about 4 days.

The correlation between solar flares and solar-proton events is still somewhat uncertain. For example, solar-proton events have been observed to occur during a period of low solar-flare activity and, conversely, high solar-flare activity is not always accompanied by solar-proton events. More and more data are being obtained to establish a relationship between the two solar phenomena.

Certain facts about the solar activity cycle will aid in the analysis. For instance, solar-flare activity has a cycle of 11 years, during which time its rate of activity goes from a minimum to a maximum. The present cycle, number 19, reached its maximum in 1958. During the period of 1962 to 1965, relative solar minimum activity should prevail. During the years from 1965 to 1969, maximum solar activity is predicted.

A second cyclic solar phenomenon of some consequence exists. Sunspots (or flares) have been observed and recorded since 1875 and earlier. On the basis of these observations, it appears that the over-all solar activity during an 11-year solar cycle changes from one cycle to another. This change also appears to be of a cyclic nature, repeating itself every 175 to 185 years. The last four 11-year solar cycles have indicated a pronounced over-all increase from cycle to cycle in the total number of sunspots. There is an uncertainty as to whether (1) this upward trend will continue into cycle 20 beginning in 1962) or (2) the 175-year cycle will begin to repeat itself, making cycle 20 a minimal activity cycle. However, even if cycle 20 has a low relative number of sunspots, the possibility of having many large solar-proton events is by no means excluded.

It is certainly desirable to attempt a correlation between solar flares and solar-proton bursts on a probability basis. Such an effort could possibly yield some realistic probabilities for solar-proton events occurring during a certain time in the solar activity cycle. An effort toward this end is now being made. The results of this effort will hopefully yield probability figures for a given radiation damage to solar cells in a certain time period.

f. Solar-cell space efficiency standards. It is a well-known fact that the light-generated current in a solar cell is dependent on (1) the total intensity of the light source, and (2) the spectral character, or spectral distribution, of the light source. Since the light source for solar cells in space is the Sun, then, ideally, the light source under

CONFIDENTIAL

which single solar cells or groups of solar cells are tested should have (1) the same intensity as the Sun in space and (2) the same spectral character as the Sun in space. To date, the most successful light source for the testing of single solar cells and groups of five solar cells in series has been a tungsten light source operating at a 2800°K color temperature. Figure 15 shows the relative spectral distribution of a 2800°K tungsten lamp in relation to the spectrum of the Sun in space. Attempts have been made to procure a laboratory light source which has the same spectral character and intensity as the Sun. However, such attempts have been complicated by (1) the difficulty in measuring the spectral character of the light source and (2) the difficulty in measuring the total intensity of the light source. Different types of radiation sensing devices, such as pyrheliometers and thermopiles, have been used for the measurement of both total and spectral light intensity. However, such devices can not be accurately calibrated on either a total intensity or spectral intensity basis. The ideal device for the measurement of the intensity of a light source to be used for solar cell testing would be a solar cell whose short circuit current output in sunlight above the Earth's atmosphere is known. For this purpose, a program for the measurement of solar cells at high altitudes has been entered into by JPL.

The General Mills Balloon and Aerospace Division, Minneapolis, Minn., has been awarded a contract for the performance of three balloon flights for solar cell measurements. The first balloon flight took place on March 21, 1962. Due to noise generated in the telemetry system, the automatic aborting system was fired at an altitude of 50,000 ft. Since the balloon was to have reached an altitude of 80,000 ft, the first flight was unsuccessful and no useful data were obtained. The second flight took place on June 13, 1962. This flight was very successful, yielding 3½ hr of data at an altitude of 77,000 ft above sea level. During this time the short-circuit currents of 14 different solar cells were measured every 6 min. Two of these cells are shown in Fig. 16. The data from this flight has not been completely reduced, but preliminary data indicate that the measurements were very good.

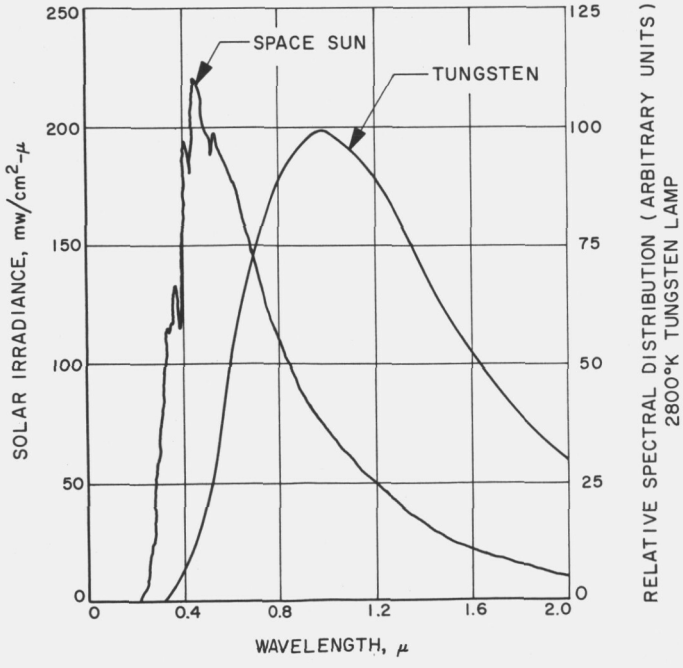

Fig. 15. Comparison of the relative spectral distribution of space sunlight and radiation from a tungsten source

Once the data have been reduced and the measurement error has been determined on the 14 solar cells measured on balloon flight 2, these cells may be used as primary standards. These are the first cells to date which have been measured in what are essentially Earth-space conditions and have been recovered.

g. Electrical conversion.

Mariner *B battery charger.* In order to provide battery-charging power during all cruise periods throughout the *Mariner* B flight, a booster type of charger system was needed. During the low panel voltage portions of the mission there was not sufficient margin between the lowest panel output and the battery voltage to make use of the series type of charge regulator.

The battery terminal voltage will increase to its maximum value when the charging power is first applied. After a short charge period, the voltage will decrease to

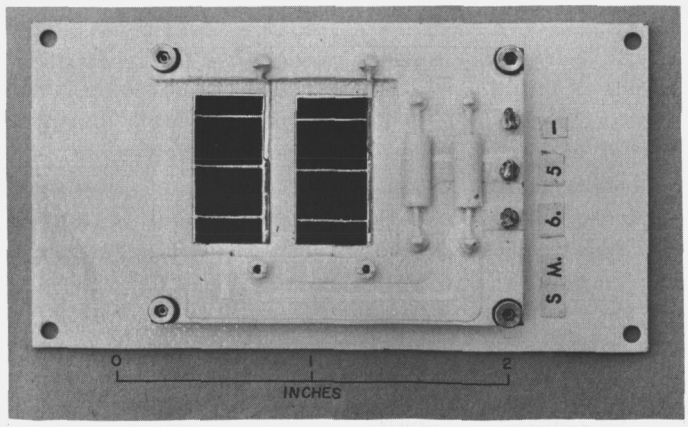

Fig. 16. Solar cell space efficiency standards

CONFIDENTIAL

a lower plateau until the charge nears completion. The charge regulator must be capable of furnishing the initial and final voltage peaks and of limiting the maximum current levels during the main charge periods. The limited availability of power during cruise flight periods will place an additional restraint on the maximum allowable current levels.

The design approach used for this program is shown in the block diagram (Fig. 17). An inverter power amplifier, driven by a transistor oscillator, increases the voltage through a step-up transformer. Voltage regulation is controlled by a series magnetic amplifier. The rectifier and filter converts the power to smooth direct current. A voltage reference from this point closes the regulation loop to the magnetic amplifier.

The final element between the regulated dc and the load is a current limiter. The maximum limit level is selected to match the critical factor, battery charge current or available raw power. The output voltage is reduced gradually as the load current increases.

The driver oscillator is a transistor magnetic-core circuit. The inverter amplifier uses a pair of silicon power transistors which switch the power transformer at a frequency of several thousand cycles. A center-tapped magnetic amplifier circuit follows the transformer and is controlled through a zener diode reference. Silicon rectifier diodes and the inductor-capacitor filter complete the voltage loop. The current limiter consists of a series connected power transistor and its current sensing network.

A breadboard circuit of the battery charger was built and tested to evaluate operational limits. The dc input voltage ranged from 28 to 50 v. The regulated dc output was set for 36 v dc to match the anticipated battery terminal voltage at full charge.

Load and line regulation tests and efficiency measurements were made on the regulated supply portion of the charger without the current limiter. The output voltage change over a load current range of 0.1 to 2 amp was 0.8 v, or about 2%. At constant loads of up to 1 amp, the output changes approximately 2% for an input range of from 32 to 50 v dc. Variations at the higher currents will be masked by the current limiter action.

Power efficiency is better at lower input voltages and reaches 75% at 1-amp load and 30-v input. The efficiency drops to about 65% with 50-v input. Efficiency curves over a 2-amp load range at three input voltages are given in Fig. 18.

The addition of the current limiter changes the output characteristic, as shown in Fig. 19. The maximum voltage

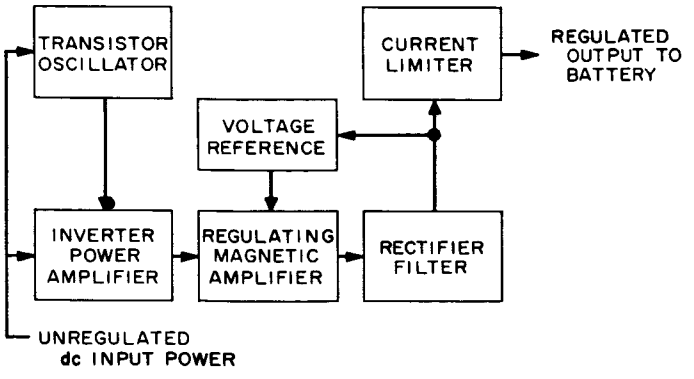

Fig. 17. Regulating battery charge supply block diagram

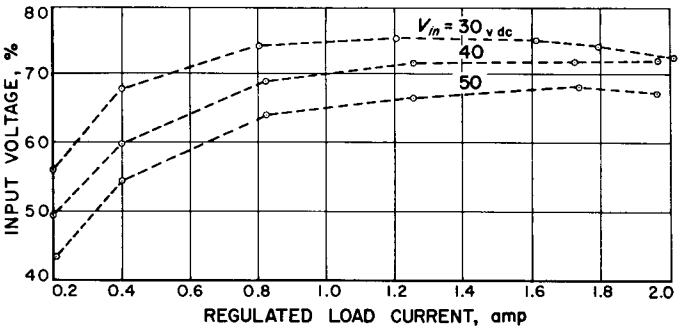

Fig. 18. Power efficiency as a function of load current and input voltage

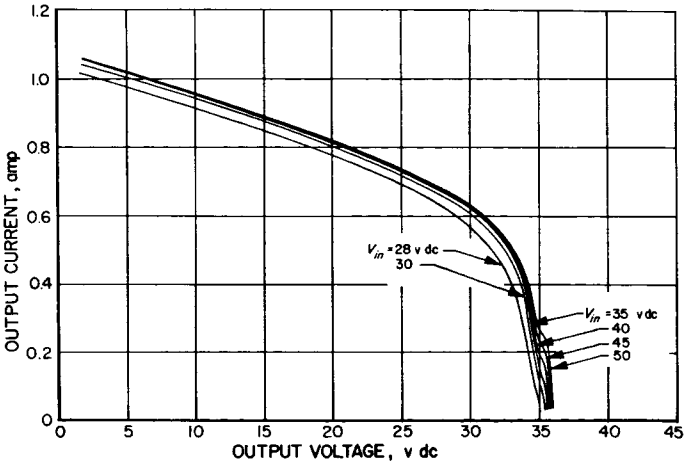

Fig. 19. Output voltage versus load current with current limiter

is available only at very low currents. The output voltage drops as the current increases and approaches zero at a maximum current of 1.1 amp. Under peak charging conditions the output will probably stabilize around 27 v at a current of 0.7 amp.

An alternate current-limiting scheme involving the inclusion of the current sensor in the magamp control loop is being considered as a means of simplifying the charger. A somewhat sharper "knee" in the charger characteristics may be expected using the alternate circuit.

Booster and inverter. The proposed mechanization of the *Mariner* B power system is a square wave output ac distribution system utilizing booster regulators and square wave inverters similar to that used on *Mariner* R spacecraft. An investigation is presently underway which will result in an improvement of this system in over-all performance and efficiency.

The *Mariner* R booster regulator stability characteristics have been re-evaluated. The open-loop characteristics have indicated that in order to assure stability over the *Mariner* B extreme load and voltage variations it is desirable to increase the phase and gain stability margins. This has been achieved by the introduction of phase lag compensating networks. The open-loop characteristic plots have shown that the modified booster design has improved stability margins.

In order to improve the efficiency of the booster, an investigation of all the power-dissipation areas has been initiated. A large amount of power is being consumed in the power transistor in the amplifier. This loss is composed of switching losses and saturation losses. An attempt is being made to reduce the switching losses by using new triple-diffused transistors with improved switching characteristics. The application of these transistors to the circuit has shown an improvement in efficiency of about 4 to 6%. It is anticipated that the application of the higher speed switching transistors to the inverter will also result in an increase in efficiency. Selection of transistors for low saturation resistance will minimize saturation losses in both the booster and inverter.

The booster oscillator circuit has been redesigned to reduce losses in the switching transistor and transformer. A reduction of power loss of about 3 w has been achieved.

h. Energy storage devices. Although the design specification for the *Mariner* B spacecraft energy storage devices has not been finalized, the following main flight battery characteristics have been defined:

Type: Rechargeable in flight

Weight: 64 lb

Capacity: 67 amp-hr

Voltage range: 25.8–33.3 v

At the present time, no batteries meeting the above requirements have been procured. However, a number of existing cells and batteries have been obtained in order to perform evaluation tests. One of these tests involves the float charging of an existing *Mariner* R battery. This rechargeable silver-zinc battery has now been on an extended float charge profile for approximately 34 weeks. Periodic load tests during this period indicate satisfactory performance and tests are continuing. Similar tests for the silver-cadmium cell are also being conducted. Other tests include cycling, and temperature effects.

A regenerative hydrogen–oxygen fuel cell development has also been sponsored for the *Mariner* B requirements. Electro-Optical Systems, Inc., has been selected as the contractor. Design objectives are for a 1200 w-hr unit, to operate between 70 and 210°F. Advantages of a fuel cell are in its ability to be on float charge for an indefinite period of time without deterioration, no deterioration with number of cycles, and ease of measurement of state of charge. The weight is expected to be competitive with silver-zinc batteries.

In addition to the main energy storage device, activity has been initiated into the area of thermal batteries as a separate energy storage device for squib events. Thermal batteries are fused salt electrochemical systems. Some of the advantages and disadvantages of the batteries thus far tested are listed in Table 8. Tests to date include batteries from the Eagle Picher Co. and the Eureka Williams Co.

Table 8. Thermal battery characteristics

Advantages	Disadvantages
Long shelf life	High discharge temperatures approx. 500°F
Can be heat sterilized	Response time to load longer than than either Ag-Zn or Ni-Cd. (about 0.4 to 1 sec)
Gassing problems insignificant No leaks due to pressures	W-hr/lb lower than Ag-Zn and roughly comparable to Ni-Cd batteries. Between 2-7 w-hr/lb of battery package
Lowest weight for high current–short pulse situations	

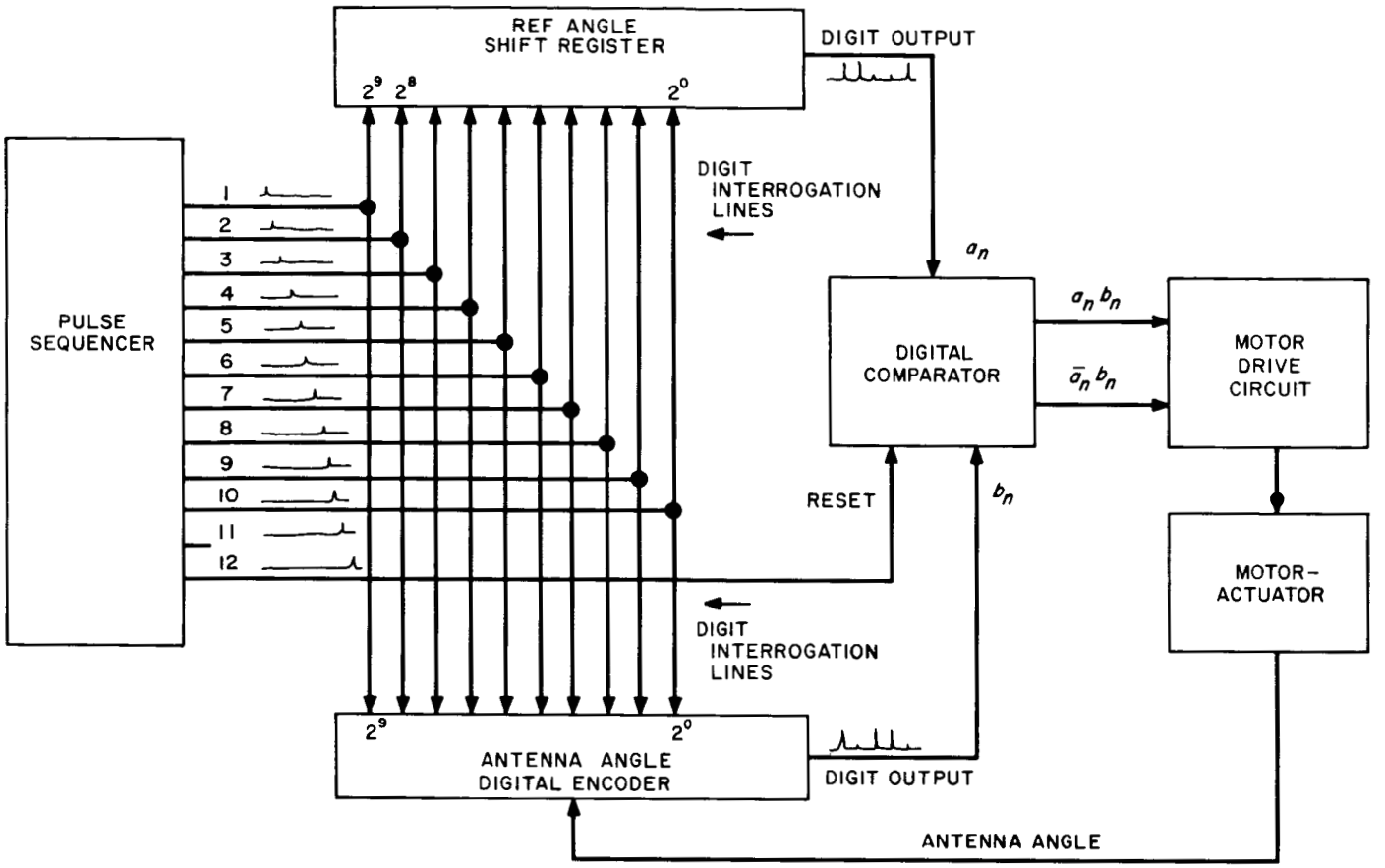

Fig. 20. Digital servo block diagram

2. *Attitude Control*

a. Antenna control system. Since the *Mariner* B spacecraft is not Earth-oriented, the high-gain antenna requires 2 deg of freedom and control. Each axis is controlled by a program generated in the CC&S. The program for each axis starts from an initial preset angle and continues as an incremental function. Upon receipt of a start command from the CC&S, the antenna is controlled by a digital-position servo which positions the antenna to the initial preset angle. The antenna angle is compared with a digital reference angle stored in a binary shift register and the error controls the antenna actuator.

The fundamental digital servo problem has been discussed in *SPS 37-14*. It has been shown that it is advantageous to determine only the sign of the position error from a bit-by-bit comparison of the two numbers. The sign of the difference is the sign of the most significant nonzero comparison.

A functional block diagram of the digital servo is shown in Fig. 20. This system utilizes a sequential comparison of the reference and position numbers starting with the most significant digits.

The sequencer utilizes a current-steering commutator circuit.[b] Each sequential output is a 400-ma current pulse of 2- to 4-μsec duration. This pulse is well suited for interrogation of the magnetic shift register and is easily converted to a voltage pulse for encoder interrogation by the use of a small load resistor. A partial schematic of the sequencer is shown in Fig. 21. A two-phase current pulse source is the input to the circuit. The circuit operates with all cores except one in the plus-saturation or "set" state. The input current pulse switches this single core from the reset to the set state and induces a voltage in its winding. This induced voltage back biases all the diodes except the one corresponding to the core being set, thus steering the input current pulse through the forward biased diode and the connected load. This load current resets the next core in the sequence so that the

[b]Rajchman, J. A., H. D. Crane, "Current Steering in Magnetic Circuits," *IRE Transactions on Electronic Computers*, Vol. EC-6, March 1957, pp. 21–30.

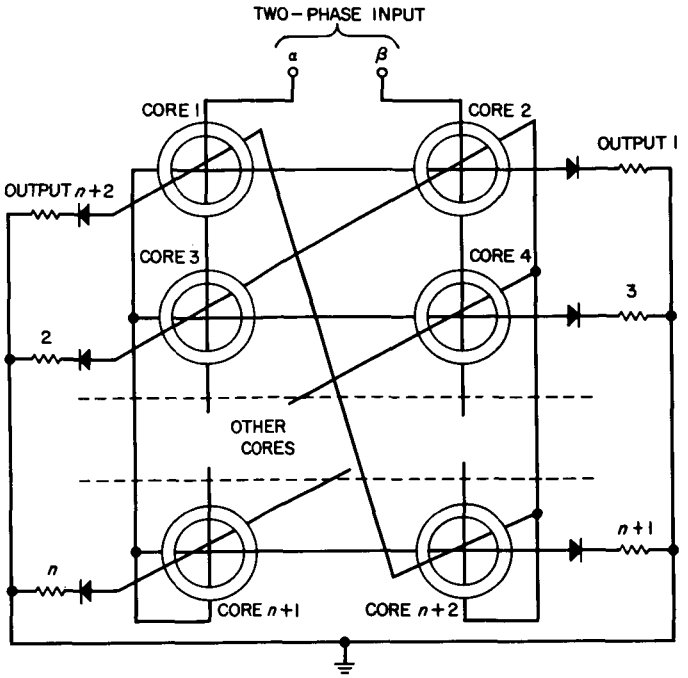

Fig. 21. Current steering commutator

next input pulse on the alternate input phase will produce a similar output. The cycle is completed by the load current of the last core resetting the first core. As compared with a semiconductor ring counter, this circuit has the advantages of simplicity, low power consumption, and high output current availability.

The reference number is stored in a multi-aperture core shift register provided with a separate interrogation winding for each bit and an output winding linking all bit cores of the register. The content of the register is read by pulsing the interrogation winding of each bit in sequence. A "one" digit is read by the interrogation current reversing the flux path about the minor aperture of the core, which induces a voltage in the output winding. A "zero" corresponds to a saturated state such that the flux does not reverse and no output voltage is produced.

The output angle encoder is pulse interrogated in a similar manner. A "one" digit in the encoder is characterized by a low resistance path between the digit output and a common return, while a zero corresponds to an open circuit. A pulse voltage is applied to each digit line in sequence; its presence or absence at the encoder common corresponds to a "one" or "zero," respectively.

The serial outputs of the reference register a_n, and the angle encoder b_n, are routed to a comparator. The comparator has two separate outputs, $a_n b_n$ and $a_n b_n$, corresponding to the conditions where $a_n > b_n$ and $b_n > a_n$. A bistable circuit in the comparator locks up both outputs after a nonzero comparison is made. This prevents comparisons of less significant digits and retains the comparator output corresponding to the most significant inequality until it is reset by the sequencer. The comparator outputs control the phase sequence of the motor drive circuit, thus controlling the direction of rotation of the four-phase stepper motor.

This circuit has been breadboarded in the laboratory and good results have been obtained. Instability has been noted at certain critical frequencies of operation. This instability is due to the comparator operating on transitional values of the encoder digits, with a resultant error in the comparison. The lowest critical frequency is above the normal operating range of the *Mariner* B antenna servo, so this instability is not a significant system problem. Further investigations of the general stability problem will be made in the future.

b. Attitude control. The *Mariner* B attitude control maintains the necessary spacecraft orientation for the purpose of:

(1) Making scientific measurements.

(2) Improving the spacecraft trajectory by the addition of corrective velocity vectors.

(3) Providing an oriented vehicle for the injection guidance of the spacecraft or on-board experiments into orbiting or landing trajectories.

During the coasting phase of flight, attitude control is maintained by pointing the roll axis at the Sun and then control about the roll axis, established by using the star Canopus as a reference. In preparation for the powered-flight phase, spacecraft orientation is established by making commanded turns based upon the Sun–star reference system, and then during the powered flight an autopilot maintains the direction of the velocity vector. The magnitude of the velocity vector is determined by integrating the output of an accelerometer.

c. Acquisition system. The *Mariner* B coasting attitude control must be capable of acquiring the Sun–star reference system, automatically, under the following conditions:

(1) Following separation of the spacecraft from the booster with separation rates about each axis of 3 deg/sec maximum.

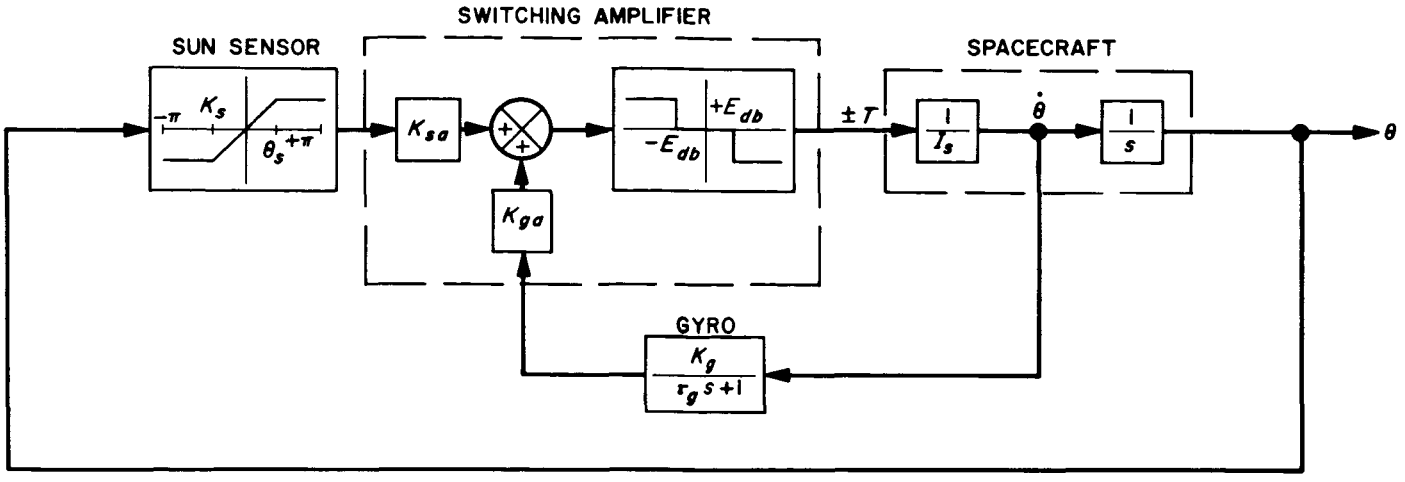

Fig. 22. Pitch and yaw acquisition block diagram

(2) Following the completion of any commanded turn and powered-flight phase.

(3) Following the loss of attitude control due to a non-catastrophic disturbance.

Attitude is maintained by the use of three independent control systems, one for each spacecraft axis. In each case, control torques about the axes are provided by valves and jets expelling cold nitrogen gas. Optical and inertial sensors yield position and rate information for control purposes. The pitch and yaw control systems, which point the roll axis at the Sun, are identical. The roll control system, which uses the star Canopus as a reference, has differences that require a separate description.

d. Acquisition system description.

Pitch and yaw acquisition. A block diagram of the pitch (or yaw) system is shown in Fig. 22. The pitch (or yaw) angle θ is detected by a sensor with a 2π rad field of view, and a linear region around null of ± 1.65 deg. The linear region, with a gain K_s, provides the necessary angular error signal to establish the cruise limit cycle deadband of ± 0.1 deg. The saturation region ($\theta = \theta_s$) output combined with the single-degree-of-freedom gyro rate output, results in a constant rate to bring the Sun into the linear region. Once in the linear region, the rate and position are reduced to the values necessary to allow the cruise system to take over. The rate and position information are fed into a switching amplifier which actuates the valves and jets to provide the constant control torques $\pm T$. It may be seen from the block diagram that the switching amplifier actuates the valves and jets whenever the sum of the position and rate output are equal to (or greater than) E_{db}, the switching voltage deadband. In a steady-state condition, this is expressed by

$$K_s K_{sa} \theta + K_g K_{ga} \dot{\theta} = \pm E_{db} \tag{1}$$

where

K_g = Sun sensor gain in linear ragion

K_{sa} = switching amplifier gain referred to Sun sensor

K_{ga} = gyro gain

K_s = switching amplifier gain referred to the gyro

E_{db} = switching amplifier deadband

Equation (1) may be normalized as follows:

$$\theta + \tau\dot{\theta} = \pm\theta_{db} \tag{2}$$

where

$$\tau = \frac{K_g K_{ga}}{K_s K_{sa}} \quad \text{in seconds}$$

$$\theta_{db} = \frac{E_{db}}{K_s K_{sa}} \quad \text{in milliradians}$$

When the spacecraft separation rates are being reduced, the Sun sensor saturation θ_s will cause the spacecraft to acquire at an acquisition rate $\dot{\theta}_s$, determined by:

$$\dot{\theta}_s = -\frac{\theta_s}{\tau} \pm \frac{\theta_{db}}{\tau} \tag{3}$$

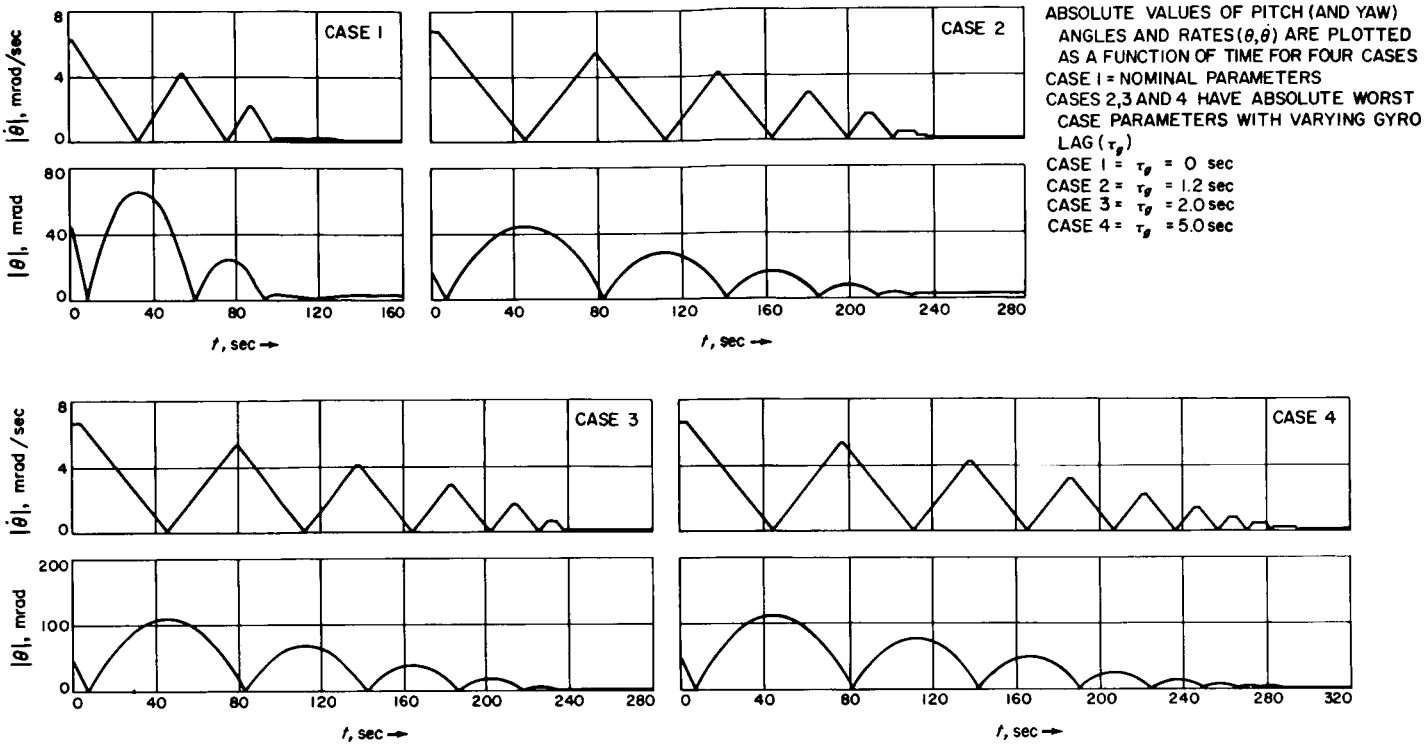

Fig. 23. Pitch and yaw acquisition in the linear region

where $\theta_{db} << \theta_s$, and θ_s/τ essentially determines the acquisition time. In the linear region of the Sun sensor, the position error will be reduced to the switching amplifier deadband value. At the same time, the rates will be reduced by the damping effect of the gyros, determined by τ. During this phase, dynamics are very important, and the problem was analyzed on the analog computer. The most significant effect studied was the problem of a rather large time lag associated with the gyro damping fluid, which is a function of temperature. If an acquisition process is necessary after the spacecraft has stabilized its temperature to the space environment, depending on the gyro being used, the time lag can be as large as 2 or 3 sec.

Analysis results—pitch and yaw system. In the process of obtaining control system parameters, mechanization constraints as well as system requirements must be considered. For the pitch and yaw system, the following parameters were obtained:

K_s = Sun sensor gain (normalized) = 1.0

θ_s = Sun sensor saturation (linear region) = ±1.65 deg (28.8 mrad)

θ_{db} = switching amplifier deadband = ±2 mrad (0.1165 deg)

τ = ratio of rate to position gain = 5 sec

α = spacecraft control torque acceleration (torque to inertia ratio) = ±0.2 mrad/sec^2

This means that the maximum acquisition time in the saturated region of the sensor is 9 min $\pi/(\theta_s/\tau)$ for completely nominal operation.

Analog computer runs were made for the operation in the linear region. Four of the cases are used to illustrate the performance (Fig. 23). The analog computer outputs are in the form of plots of the absolute magnitudes of pitch (or yaw) angle and rate versus time. In every case the Sun sensor gain (K_s) has been normalized so that it is always one. Tolerances have been established for the various parameters and these are varied, as described below, to illustrate their effect upon performance. Case 1 is a completely nominal case with which to compare the others. Cases 2, 3, and 4 use parameters whose tolerances have been applied in a manner to produce absolute worst cases. Different values are used for the gyro time lag τ_g.

The significance of the gyro time lag arises from the problem of keeping the gyros at operating temperature when they are not being used during the cruise periods. This analog computer study helps illustrate the effect of different temperatures on acquisition performance. The

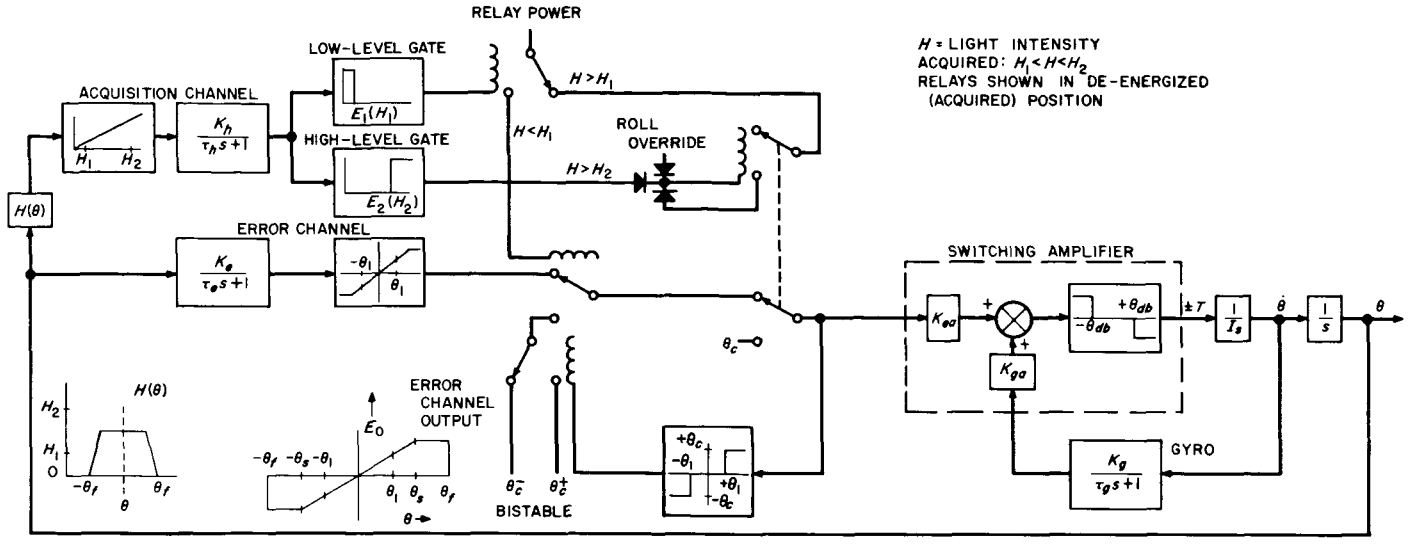

Fig. 24. Roll acquisition block diagram

time lag τ_g varies with temperature as a function of the change in gyro damping fluid viscosity. Therefore, τ_g versus temperature will vary from one gyro to another, depending upon the fluid used. Since the actual flight gyro has not yet been picked, the performance can not be picked. However, the time constant at operating temperature will be in the neighborhood of 0.5 to 1 sec. For a cold start (50°F), the time constant will be in the neighborhood of 2 to 3 sec.

Referring to Fig. 23, the cases are as follows:

Case 1. All nominal parameters

K_s = Sun sensor gain = 1.0

θ_s = Sun sensor saturation = ±28.8 mrad

τ = rate to position gain = 5.0 sec

α = control torque acceleration = ±0.2 mrad/sec²

τ_s = Sun sensor lag = 0 sec

τ_g = gyro lag = 0 sec

Case 2. Worst case parameters

K_s = 1.0

θ_s = 24.9 mrad

τ = 4.1 sec

α = 0.16 mrad/sec²

τ_s = 0.02 sec

τ_g = 1.21 sec

Case 3. Worst case parameters, the same as Case 2 except that τ_g = 2 sec.

Case 4. Worst case parameters, the same as Case 2 except that τ_g = 5 sec.

Conclusions. In every case, the spacecraft acquires. Case 4 represents an extreme worst case condition, and the only effect is an increase in acquisition time and gas consumption. But the total acquisition time is increased by only about 200 sec, and the gas consumption is estimated to be increased by only about 1% for each axis (pitch and yaw) for one acquisition.

Roll acquisition. In the sequence of operations, roll acquisition is initiated after the completion of pitch and yaw acquisition. This is accomplished by control logic to be described later under "automatic acquisition." A block diagram of the roll acquisition system is shown in Fig. 24. There are two significant differences from the pitch and yaw system. These are: (1) the star sensor roll field of view is very limited (±2 deg) and (2) the star Canopus must be identified, that is, differentiated from other celestial objects. The same principle of position plus rate used in the pitch and yaw system is also used here. In addition to this, the star brightness is detected and channeled through a low-level (H_1) and a high-level (H_2) gate. The brightness of Canopus is between H_1 and H_2. If the brightness H is less than H_1, then relay power in

the line $H > H_1$ puts a plus or minus command ($\pm\theta_c$) from the bistable relay into the roll channel and starts the spacecraft in a roll search mode. During this search, if an object for which $H > H_1$ is picked up, the roll channel is switched from $\pm\theta_c$ to the star sensor roll-error signal, which takes over control. If $H > H_2$, the high-level gate switches another search command (θ_c) into the roll-error channel. It also switches in a signal from the gate $H > H_1$ as a lockup. θ_c causes the object to roll out of the sensor and in the process, when H drops to $H_1 < H < H_2$, the $H > H_1$ line keeps θ_c locked in to completely lose the object. Then when $H < H_1$, $\pm\theta_c$ is switched in and the search continues.

In order to accommodate the small roll field of view, a switching amplifier is used to set the bistable roll-search relay ($\pm\theta_c$). As the star passes through the field of view, when roll angle $\theta > \theta_1$, the relay is set to $+\theta$. If the star goes out of the field of view before it is acquired, $+\theta_c$ will continue the deceleration to reverse the spacecraft and bring the star back. Of course, if $\theta < -\theta_1$, the relay is set to $-\theta_c$.

The same problem of long gyro time constants (τ_g) exists in the roll system as well as in pitch and yaw. In addition, relatively long time constants are associated with the star sensor. These are noted as τ_e in the roll error channel, and τ_h in the identification channel.

Analysis results—roll system. As in the pitch and yaw systems, mechanization constraints and system requirements were considered and the following nominal parameters for the roll channel were selected:

K_e = star sensor gain (normalized) = 1

K_h = brightness channel gain (normalized) = 1

θ_s = star sensor saturation (linear region) = $\pm$21 mrad ($\pm$1.2 deg)

θ_1 = bistable relay switching deadband = $\pm$12 mrad

θ_f = star sensor roll field of view = $\pm$2 deg ($\pm$35 mrad)

θ_{db} = switching amplifier deadband = $\pm$2 mrad

$\dot{\theta}_c$ = search command search rate = 3.5 mrad/sec (0.2 deg/sec)

τ = ratio of rate to position gain = 6 sec

α = spacecraft control torque acceleration = $\pm$0.2 mrad/sec^2

τ_h = brightness channel time lag = 1 sec

τ_e = roll-error channel time lag = 2 sec

Acquisition outside the field of view of the sensor is simply a matter of turning at the search rate of 3.5 mrad/sec. This means a nominal maximum acquisition time of 30 min. (It is assumed that the separation rates have been reduced before the roll search begins.) Analog computer runs were made for acquisition in the sensor field of view. Five cases are shown to illustrate performance. These are presented in Fig. 25. Absolute values of roll position and rate are plotted versus time.

Case 1. All nominal parameters, as shown above with the gyro lag, τ_g = 0.46 sec.

Case 2. Worst case parameters. Tolerances are included in a manner to produce an absolute worst case. τ_g = 1.2 sec.

Case 3. Worst case parameters. τ_g = 2 sec.

Case 4. Worst case parameters. τ_g = 5 sec.

Case 5. This case has been included to illustrate how an object with $H > H_2$ is rejected. The parameters are the same as those used in Case 3.

Conclusions. As with the pitch and yaw system, the gyro warm-up problem of long gyro time constants is not serious. However, gas consumption and acquisition time are increased accordingly. For an extremely long time constant (τ_g = 15 sec) the roll channel will not acquire. But in any case, if the gyro is turned on and spins up, it will heat up to a point where acquisition may take place.

e. Automatic acquisition. Automatic acquisition is accomplished by means of the addition of a solar detector that detects the Sun when it is within 2½ deg of the roll axis. When the pitch and yaw axis controls have brought the roll axis to within 2½ deg of the Sun, the solar detector (Sun gate) switches in the star sensor power, and the star sensor brightness gate will automatically start the roll search.

After acquisition is complete, that is, when the star sensor brightness gate is activated, the gyros are turned off after an appropriate time delay of about 180 sec. If roll acquisition is lost, the brightness gate turns on the gyros and initiates a roll search as in an ordinary acquisition sequence. If pitch or yaw acquisition is lost, the

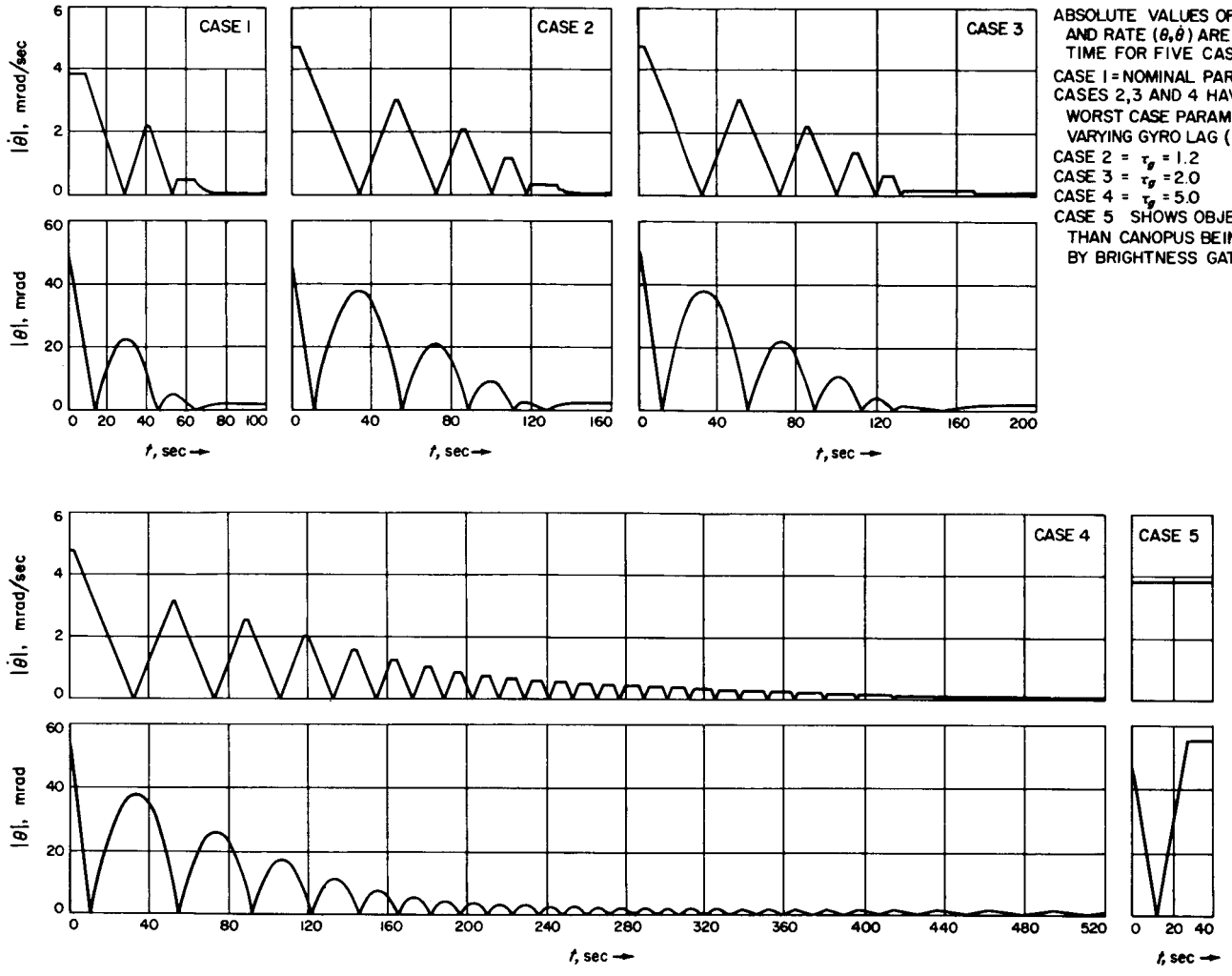

Fig. 25. Roll acquisition in the linear region

Sun gate will turn off star sensor power, turn on the gyros, and start the acquisition sequence from the beginning.

f. Commanded turn simulation. The *Mariner* B commanded turn or mid-course maneuver mechanization is presently undergoing single-axis simulation tests. The *Mariner* B commanded turn mechanization consists of a wide-angle floated integrating gyroscope with unity gain and an input axis angular storage capability of ±3 deg. The gyroscope provides the inertial reference for the spacecraft during the maneuver and powered portion of flight. The output of the gyro is mixed with a "derived rate" signal and the ratio of this mix determines the switching criteria for the system during the commanded turn. The "derived rate" or damping signal is generated from a voltage which is proportional to torque and then passively integrated to supply a rate damping term to the control system. A block diagram of the maneuver system is shown in Fig. 26.

A commanded turn, or angular displacement of the spacecraft, is accomplished by torquing the gyro gimbal through the torquer for a fixed time interval. This gimbal torque is then counteracted by the spacecraft rotation. The gyro supplies a positional error term to the switching amplifier and the derived rate network supplies the rate damping signal to stabilize the vehicle control system.

To accomplish a simulation of the commanded turn dynamics on a single-axis basis, an electromechanical simulation of the vehicle dynamics is provided. The simulator uses the output of the attitude-control system switching amplifier to drive relays in place of the actual solenoid valves used on the spacecraft. The simulator

consists of these relays to simulate the mass expulsion system, an electronic integrator and a velocity servo to simulate the vehicle inertia. The gyro is mounted to the output shaft of the velocity servo, and its output is then used as it would appear in the spacecraft.

At present, a GG49E2 Minneapolis-Honeywell gyro is being operated at a temperature of 115°F to achieve unity gain in the gyro. Analog plots of gyro-error signal, simulator rate, and torque versus time are shown in Fig. 27. A corresponding phase plane plot derived from this data is shown in Fig. 28.

g. Autopilot. The *Mariner* B spacecraft has, during the course of its flight, the capability of firing a small rocket motor to correct trajectory errors. The function of the autopilot is to maintain a stable attitude during the mid-course maneuver. Imperfect alignment of the motor thrust vector with the center of mass of the spacecraft generates disturbing torques which tend to tumble the spacecraft; the autopilot senses spacecraft displacement from the nominal heading with gyroscopes, and processes this information to position jet vanes in the exhaust stream of

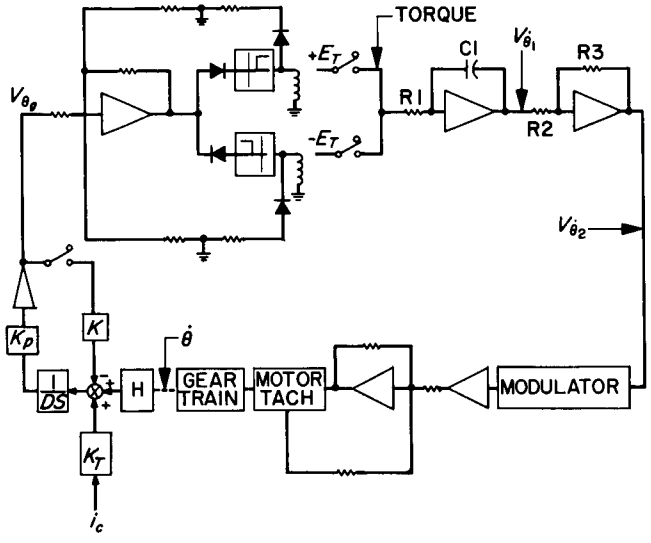

Fig. 26. Commanded turn simulation block diagram

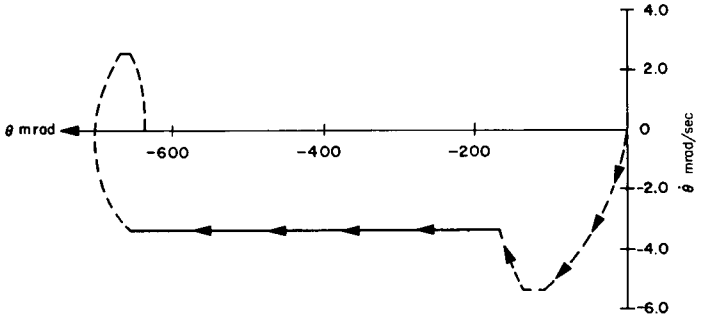

Fig. 28. Commanded turn single-axis simulation phase plane plot

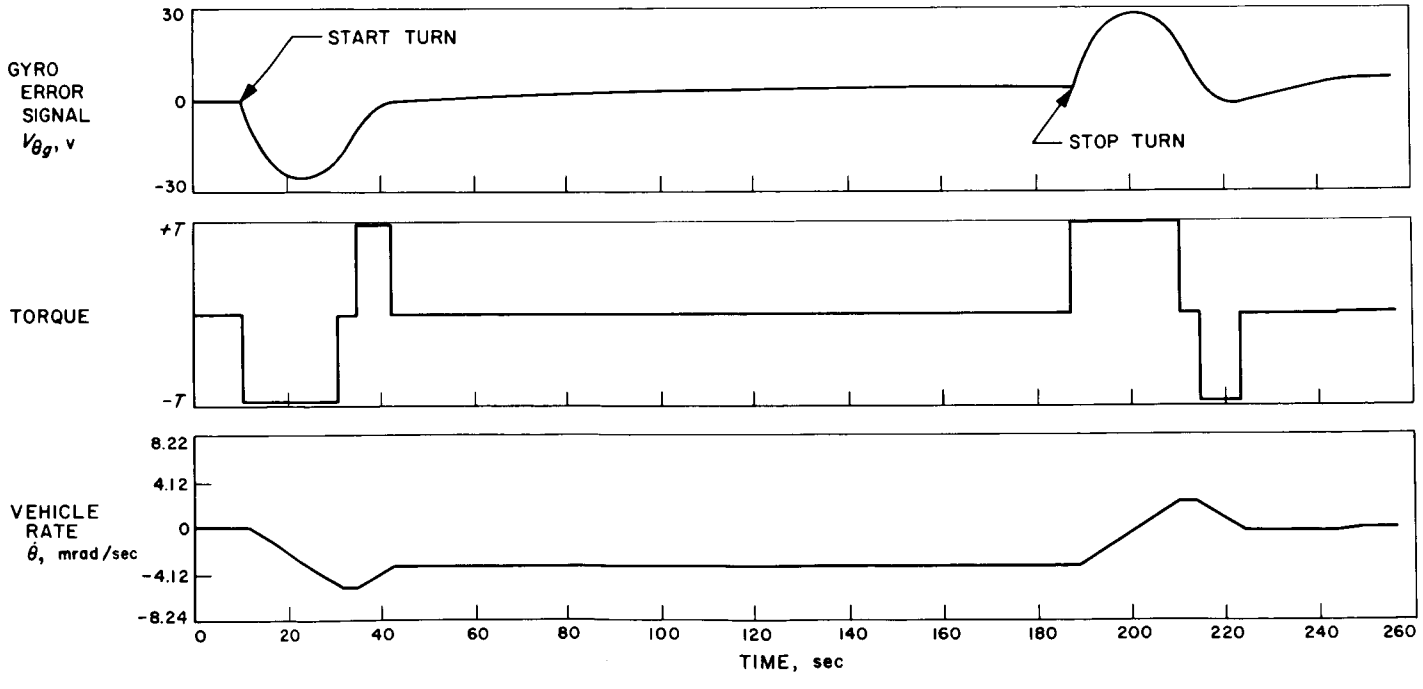

Fig. 27. Commanded turn single-axis simulation

the motor. Forces on the jet vanes provide correcting torques to stabilize the vehicle.

Because the effective action of the basic autopilot is to point the total thrust vector through the center of mass of the spacecraft, the final thrust vector will not point in the desired inertial space direction which was set with the initial heading of the spacecraft. A second control loop, called the path guidance loop, could be added to correct the spacecraft attitude to compensate for this effect. An investigation of a path guidance loop was made, but this extra loop was not adopted for *Mariner* B for the following reasons:

(1) The high moment of inertia for *Mariner* B necessitates a very slow-acting guidance loop. Thus, for the shorter firing times likely for the second, third and fourth mid-course maneuvers, the autopilot error would not be greatly reduced.

(2) It is possible to measure the location of the center of mass, motor alignment, etc., accurately enough that the error would be small anyway.

(3) If the autopilot error is expressed in terms of miss distance at the planet, the rms error of the autopilot error combined with the orbit determination error is not significantly different from that due to the orbit determination error alone.

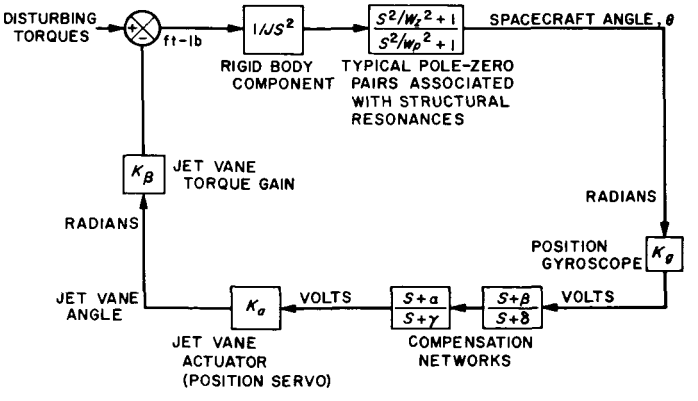

J - SPACECRAFT MOMENT OF INERTIA, SLUG ft²
W_z, W_p - STRUCTURAL RESONANCE FREQUENCIES, rad/sec
K_g - GYRO GAIN FACTOR, v/rad
γ, α, β, δ - COMPENSATION NETWORK FREQUENCIES, 1/sec
K_a - JET VANE POSITION GAIN, rad/v
K_β - JET VANE TORQUE GAIN, ft-lb/rad

Fig. 29. Single-axis autopilot block diagram

The present *Mariner* B single-axis autopilot block diagram is shown in Fig. 29. The spacecraft angle is sensed by integrating gyroscopes which give a voltage signal proportional to the spacecraft angle θ. The use of position gyros instead of rate gyros is a departure from the *Ranger* and *Mariner* R autopilot system. Position gyros have these important advantages:

(1) There are no low-frequency resonances such as occur with the rate gyros, with their torque rebalancing systems. This makes the problem of autopilot interaction with structural resonances much simpler.

(2) There is less noise associated with the position gyro.

Compensation networks are required to give adequate damping and phase margin to the system. One pole-zero pair provides damping for the low-frequency poles associated with the rigid body component of the spacecraft. The other provides phase margin for pole frequencies associated with structural resonances. The effect of the compensation is shown in Fig. 30, the autopilot root locus diagram.

The jet vane actuator system consists of amplifiers driving dc torque motors with position feedback, thus making the output shaft position proportional to the input voltage.

Efforts in the autopilot area are directed toward developing the necessary electronic circuits and refining the system analysis. The single-axis spacecraft simulator will be used in the electronics development, as well as for

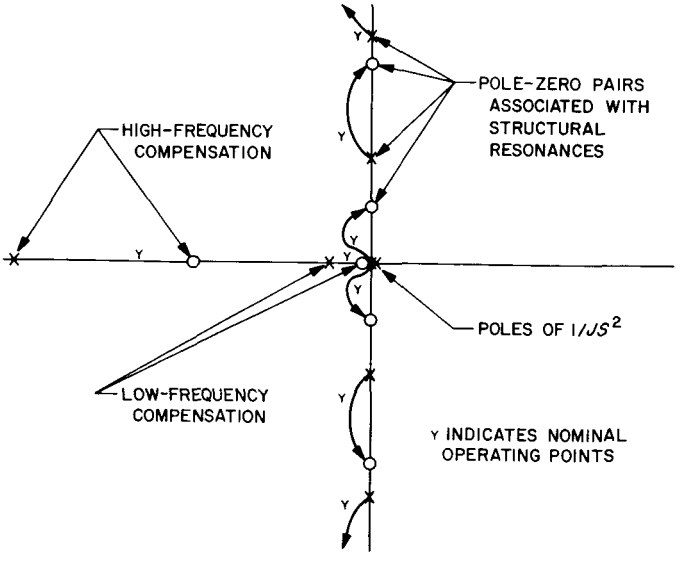

Fig. 30. Autopilot root locus diagram

evaluating the effects of nonlinearities due to friction and torque saturation in the actuator.

The effect of combining all components into a three-axis autopilot system is being studied with the 6-deg-of-freedom analog computer program. This program simulates the spacecraft with elastically coupled members, and allows three-dimensional translation and rotation. It also simulates the three gyroscopes, the four jet-vane actuators, and the jet-vane forces as they occur in the real system.

h. Gyro evaluation. Design of the *Mariner* B attitude-control system has included the use of the gyro's angular input capability, which in the case of *Mariner* B has been specified as ± 5 deg. This compares to an angular input capability of a few arc sec in both the *Ranger* and *Mariner* R gyros. It should be pointed out, however, that the angular input freedom and gain of the gyro are design selections based on the amount of gimbal damping and position of the gimbal stops, and, therefore, the use of a wide-angle gyro for *Mariner* B does not represent a new development by gyro manufacturers. The design of the *Mariner* B system constitutes the first spacecraft application of a wide-angle gyro by JPL, and a comprehensive evaluation of several high performance, miniature rate-integrating gyros, capable of being used in wide angle applications, is being conducted. Four gyros, each from a different manufacturer, were procured for this evaluation. The gyros selected were as follows: (1) Kearfott 2516-030, (2) Minneapolis-Honeywell GG8001, (3) Norden RI-203, (4) Sperry SYG-1000.

The test program established for this evaluation was designed primarily to firmly establish the gyro's performance, including stability of specific parameters, through repeated testing. This phase is being carried out under controlled laboratory conditions, using several of the industry accepted methods of testing. Secondly, the gyro is subjected to environmental testing, specified as type approval requirements for advanced *Mariner* spacecraft. The third phase of the evaluation repeats that of the first, then returns the gyro to laboratory conditions. A determination is made of the changes from the previously established performance. The evaluation of each unit is concluded with a number of special tests designed to uncover possible system usage problems, and a life test of continuous operation to 2,000 hr.

To date, the Kearfott 2516-030 gyro has completed the evaluation to the point of approximately 1500 hr in the life test. The Minneapolis-Honeywell GG8001 gyro has completed all but the special purpose tests and the life test. Detail test results, being quite lengthy, are to be reported separately. Both the Norden and Sperry gyros have not as yet been received at JPL, and are late due to manufacturing problems. Inasmuch as the program schedule necessitates an early decision as to a specific gyro, it is felt that this decision will be made based on only the two gyros presently being tested. An evaluation of the Norden and Sperry gyros will be conducted when they are available as a basis for future consideration.

3. Integrated Guidance Package Design

a. Configuration. Design aims included:

(1) All guidance sensors should be in one package that can be aligned and tested independent of the spacecraft.

(2) The package should go into the spacecraft in the same location for all *Mariner* B missions.

(3) Modification to sensors in the package to accommodate mission geometry changes should not involve gross mechanical redesign or cabling changes.

Fields of view of the three guidance sensors are responsible for the general configuration of the package and the location of the package on the spacecraft. The Sun sensors must look through the solar panel and the Canopus tracker must be far from the plane of the solar panel, so that solar panel tips are out of its field of view. The solar panels force the package to be long. Venus-type one cone angles are less than 90 deg, so the guidance planet tracker must look through the solar panel and be located close to it. Even though Mars cone angles are nominally 150 deg, the Guidance Planet Tracker (GPT) can still be located near the solar panel. It must be, because its large size would cause mechanical interference with the folded solar panels if it were located any appreciable distance above the fixed solar panel. Nominal Mars clock angles of 90 deg require the package to be located on the minus X side of the spacecraft.

The GPT as presently envisioned has a 4-deg field of view which is gimbaled by means of two single-axis mirrors so that its dynamic range is a 20-deg included angle cone. To accommodate the widely varying nominal planet directions associated with *Mariner* B missions, a mounting flange will be used to support the GPT. This flange will be tailored to suit the mission.

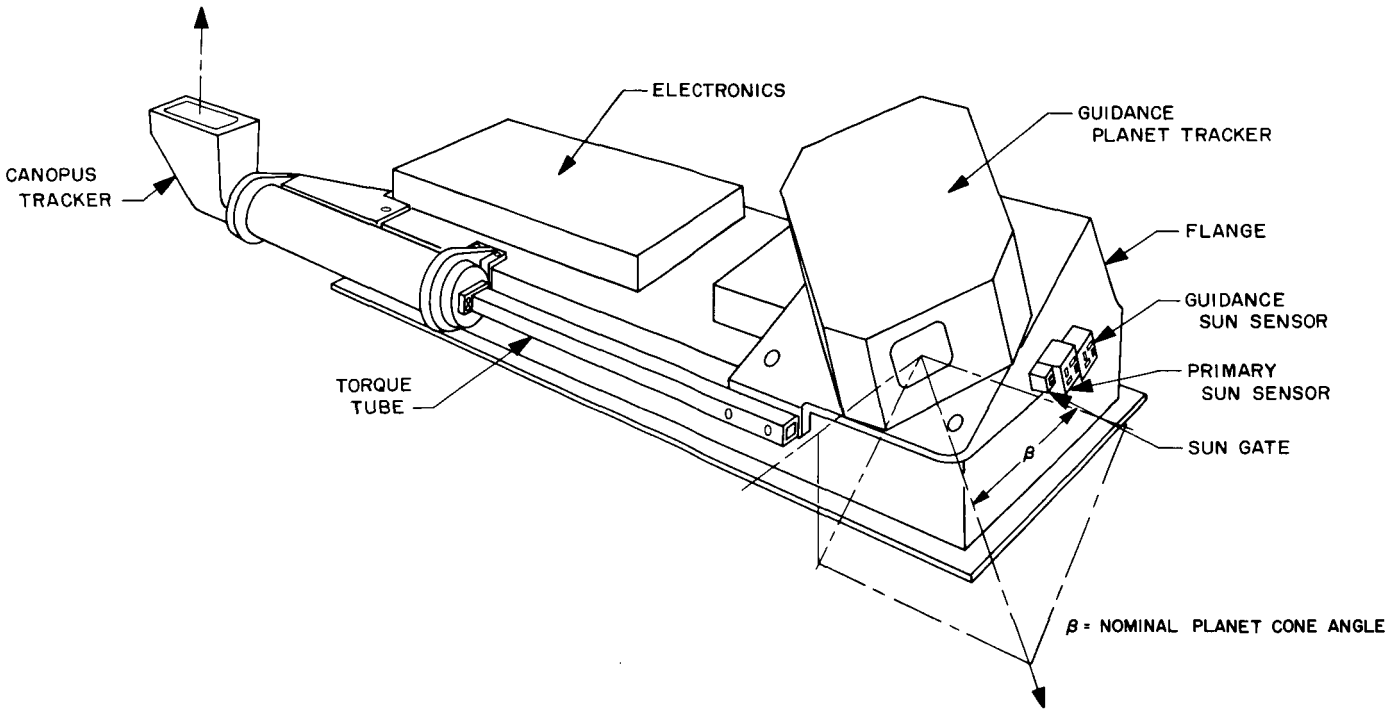

Fig. 31. Integrated guidance package

There are 2 deg of freedom needed for mounting the GPT in an arbitrary position. Cone-and-clock-angle degrees of freedom turn out to be quite convenient. The clock-angle degree of freedom is set by the flange and the cone angle is set by the rotation of the GPT on the flange face. By using this scheme the flange is simplified and one axis of the mirror gimbaling deflects the field of view along a meridian of spacecraft-centered cone-clock angle coordinates. The only compromise involved is a constraint on the mechanical configuration of the GPT: the window must be on a face which is perpendicular to the mounting surface. This constraint does not appear to be a great disadvantage. Using part of this flange for the Sun sensor mounting surface has the advantage of minimizing the number of machining tolerances between the Sun direction and the GPT.

Figure 31 shows the general configuration of the guidance package.

Relative alignment between optical sensors is most critical during the approach-guidance phase of the mission. Although an error analysis has not been completed, it is felt that relative measurement, better than 1 min of arc, will be required. During approach-guidance measurements, the zero-roll direction defined by Canopus tracker and the roll axis defined by the guidance Sun sensor must be held quite closely. This means structural bending between the GPT and Sun sensors must be minimized, and torsional warping between the GPT and the Canopus tracker must be minimized. Bending is of secondary importance in the alinement between the GPT and the Canopus tracker. The bending component in the Sun probe–Canopus plane has no effect and the component out of this plane causes only small errors in the roll attitude. This error is approximated by the following equation:

$$a = A\,(\sin b_{max} - \sin b_{min})$$

where

a = error in roll

A = angular misalignment of Canopus tracker optical axis with Sun sensor

b = Canopus cone angle

The range of the Canopus cone angle during approach guidance is roughly 2 deg. Therefore, $a = 0.035\ A$. Roughly ¼ deg absolute accuracy is needed between Sun direction and the Canopus tracker optical axis.

Bending misalignments can be caused in several ways:

(1) Thermal gradients (static and dynamic).

(2) Creep.

(3) Residual stresses established on assembly.

(4) Change in gravitational environment between time of assembly and zero-g flight.

(5) Machining tolerances.

Torsional misalignments are caused basically in three ways:

(1) Torsion loading.

(2) Differential bending.

(3) Machining tolerances.

Both bending and torsional misalignments can be minimized by keeping the package compact. Unfortunately, this is impossible, due to field-of-view constraints. However, it is fortunate that the GPT and Sun sensors are close together, since their alignment is critical in bending. To maintain the torsional alignment between the Canopus tracker and the GPT, the Canopus tracker is supported in bearings (minimizing torsional loading) and is coupled to the GPT through a single torque tube (eliminating the possibility of differential bending). The torque tube may in fact be supported in bearings at points along its length, since bending does not effect the torsional alignment of the ends. The ¼-deg absolute alignment required between the Canopus-tracker optical axis and the Sun direction must be adjusted at the time of assembly. It is reasonable to assume that thermal warping will not be serious enough to destroy this alignment.

4. Field of View Calculations

The field of view of optical sensors is determined by means of shadowgraphs. Generation of the shadowgraph has been simplified by setting up a 1620 Fortran program. Calculation of the cone and clock angles of spacecraft solar panels, science experiments, etc., as viewed from the *Mariner* B Canopus tracker is illustrated by the shadowgraph (Fig. 32). A roll-attitude degree of freedom is required by *Mariner* B, so it is convenient to make the zero-cone axis parallel to the spacecraft roll axis (roll of spacecraft then does not affect the shadowgraph outline). Canopus tracker field is shown for a roll attitude of 114 deg. Figure 32 shows that roll attitudes may be chosen between 6 and 114 deg, or between 143 and 170 deg. Between 114 and 143 deg, the ion chamber interferes with tracker cone of sensitivity.

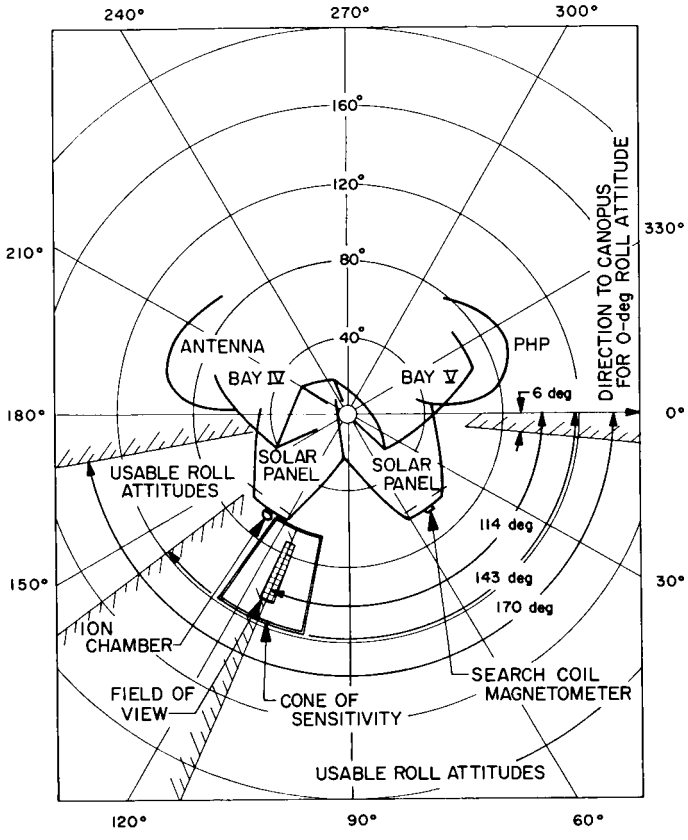

Fig. 32. Shadowgraph of *Mariner* B from the Canopus tracker

5. Sun Simulators and Sensors

a. Sun simulators. The design of the Mod I simulator as described in *SPS 37-14* has been completed. The optical system, which is comprised of standard optical components, has been set up on an optical bench. Preliminary tests indicate that the collimation accuracy is well within the design goal of ±15 sec of arc. The support structure, which has retractable casters for portability, has been fabricated. This structure supports a standard lathe bed, which in turn supports the rest of the simulator. It is estimated that all other parts necessary to assemble the simulator will be available by June 20, 1962.

The contract for the design and fabrication of the optical system for the Mod II simulator has been completed. Tests show that the collimation accuracy of this optical system also is well within the design goal of ±15 sec of arc. The over-all design of the simulator is 90% complete. All drawings should be released by June 30.

Fabrication of the lathe bed support assembly has been completed. The electronic equipment to operate the 5000-w xenon lamp has been procured.

CONFIDENTIAL

It is expected that all parts will be fabricated by July 30, allowing the assembly of the unit to proceed.

b. Sun gate. The Sun gate used on *Mariner* B is of the same design used on *Mariner* R (Fig. 33). Its output signal is used to terminate the acquisition mode whenever the spacecraft roll axis is within 2.5 deg of the Sun line. The excitation voltage to the secondary Sun sensors is removed upon acquisition. This eliminates any secondary sensor outputs which would degrade the accuracy of the primary Sun sensors since both outputs are connected to a common point.

c. Primary Sun sensor. The primary Sun sensor operates on the same principle as do the *Ranger* Sun sensors. The major difference is that the four cadmium-sulfide detectors are located in one assembly rather than at four different points on the spacecraft. This is made possible by a reduction in the field of view which prevents obstructions caused by adjacent spacecraft components. As shown in Fig. 33, a single-aperture plate provides a shadow bar for each detector. The aperture is designed to give the sensor a 44-deg total angle field of view about both the pitch and yaw axes (44 deg in pitch and 28 deg in yaw for the pitch axis and 44 deg in yaw and 28 deg in pitch for the yaw axis).

d. 4π steradian Sun sensor. The 4π steradian Sun sensor is required for *Mariner* B to give a readout of the attitude of the spacecraft relative to the Sun. The sensor has a 4π steradian field of view which allows a readout signal to be generated regardless of the position of the spacecraft.

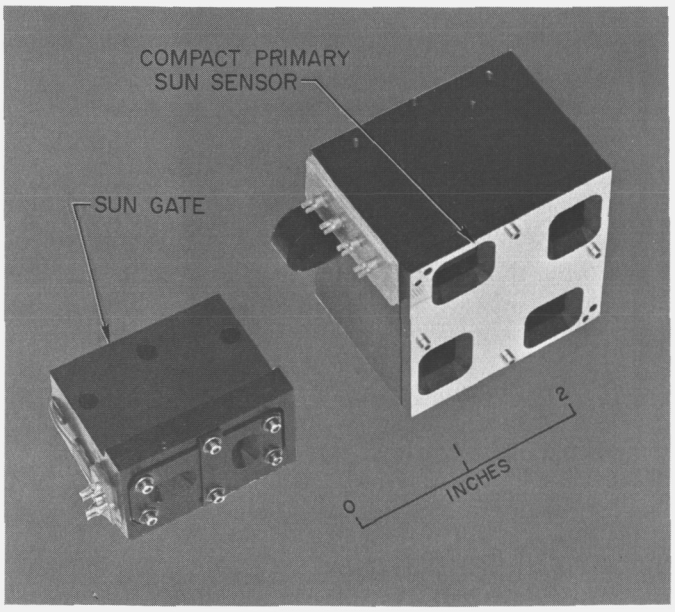

Fig. 33. *Mariner* B Sun gate

The principle of this sensor can best be understood by visualizing it as a cube having a silicon solar cell on each surface. Cells on opposing surfaces are connected to a load resistor so that the signal voltage across the resistor is plus when one cell is illuminated and minus if the opposite cell is illuminated. The system then provides three separate outputs which will be telemetered from the spacecraft. If the faces of the cube are alined perpendicular to the spacecraft axes, then the three outputs would be V_{pitch}, V_{yaw} and V_{roll}. The formulas for the angles between the Sun line and spacecraft axes (assuming a Lambert detector response) then become

$$\theta_{\text{pitch}} = \tan^{-1}\frac{Vz}{Vy}$$

$$\theta_{\text{roll}} = \tan^{-1}\frac{Vy}{Vx}$$

$$\theta_{\text{yaw}} = \tan^{-1}\frac{Vx}{Vz}$$

These calculations will be done by a ground-based computer. The actual computations will be more complex since the cell faces of the sensor will not be perpendicular to the yaw and pitch axes of the spacecraft, and the cells are not Lambert in their response.

The 2π steradian field of view required by each of the six elements of the 4π-steradian Sun sensor can only be met by placing the elements on the extremities of the spacecraft. Even then, objects in the local area of the elements may remain in the field of view. On the *Mariner* B spacecraft, science experiments on the solar panel tips make it impossible to locate three mutually perpendicular pairs of cells on the structure of the spacecraft.

To solve this problem, each element is split in two, and back-to-back mirrors are erected perpendicular to the plane of the cells (Figs. 34, 35, 36). The two mirror-cell units are now separated so that the troublesome object is occulted to the two cells by the mirrors, as shown in Fig. 35. The output currents of the two cells are summed and the sum is treated the same as the output from a simple cell. The current lost because cell No. 2 is partly or completely shaded is made up for by the increase in intensity on cell No. 1 caused by the mirror. Design requirements are:

CONFIDENTIAL

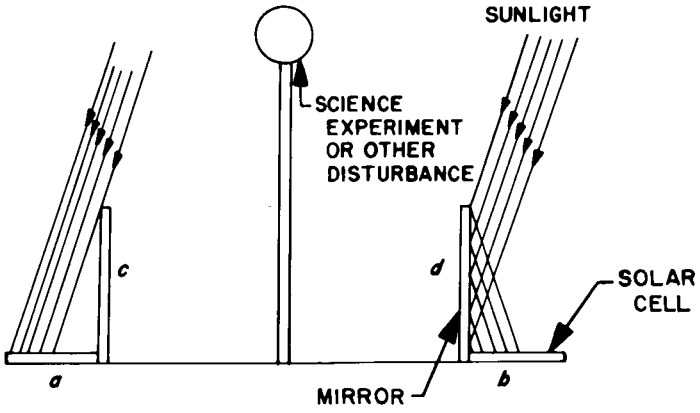

Fig. 34. 4π steradian Sun sensor occulting method

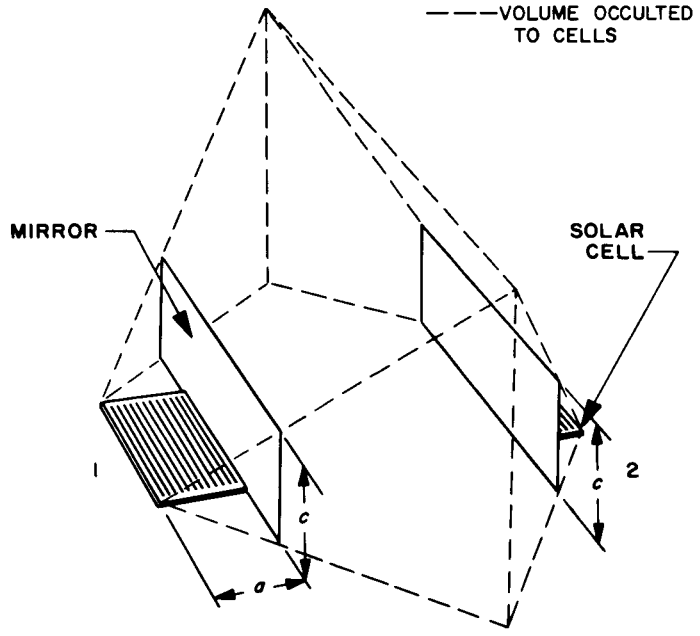

Fig. 35. 4π steradian Sun sensor experiment occultation

(1) The shape of mirrors and cells must be identical.

(2) The cells must be perpendicular to the mirror.

(3) The mirrors must be parallel.

(4) Nothing may be in the 2π steradian field of view of either cell except its associated mirror.

(5) Cell current must be a linear function of intensity.

Errors can be expected from several geometric sources:

(1) Error is contributed the system by nonperpendicularity of the elements faces (Fig. 36): maximum system error = e.

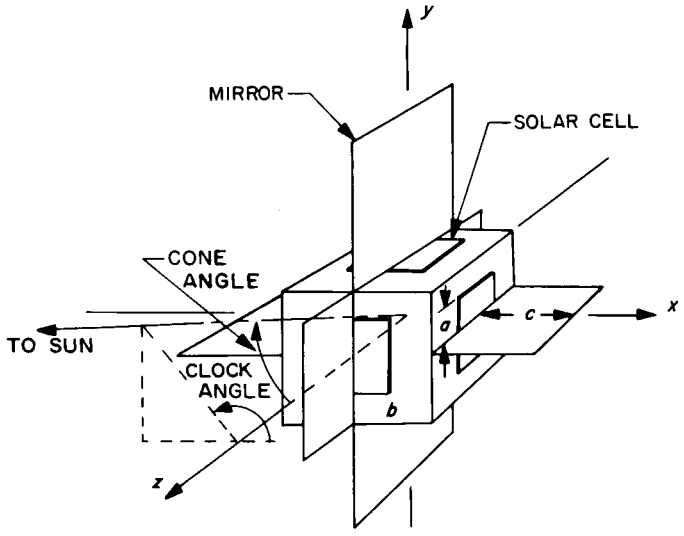

Fig. 36. 4π steradian Sun sensor, showing coordinates

(2) Misalignment of half an element: maximum system error = $\frac{1}{4}e$.

(3) The lack of a mirror (with 100% reflectance) will introduce a certain amount of error to the system. However, by making the mirrors large compared to the size of the cells, large areas of the celestial sphere will be free from error caused by reflectance since the reflectance cancels out the system equations. Shown in Fig. 37 is a polar projection of the areas for which the error cancels for the geometrical configuration shown in Fig. 38 (errors cancel in dark regions). For mirrors with 90% reflectance, the maximum error for large values of c/a will be 1.5 deg.

Test models of the cell and mirror configuration are being fabricated for testing and evaluation. Errors will also be contributed by reflected solar energy from the Earth while the spacecraft is near the Earth. When the range from the Earth's surface exceeds 4000 mi, or when the phase angle exceeds 75 deg, this error will fall below 6 deg.

e. Secondary Sun sensors. The secondary Sun sensor system for *Mariner* B is functionally the same as for *Ranger* and *Mariner* R. The physical configuration will be entirely different, however, with four of the eight detectors integrated into the 4π steradian Sun-sensor assemblies, the other four detectors, plus two of the 4π steradian detectors, will be mounted in two secondary assemblies containing two cells each and their shadow

CONFIDENTIAL

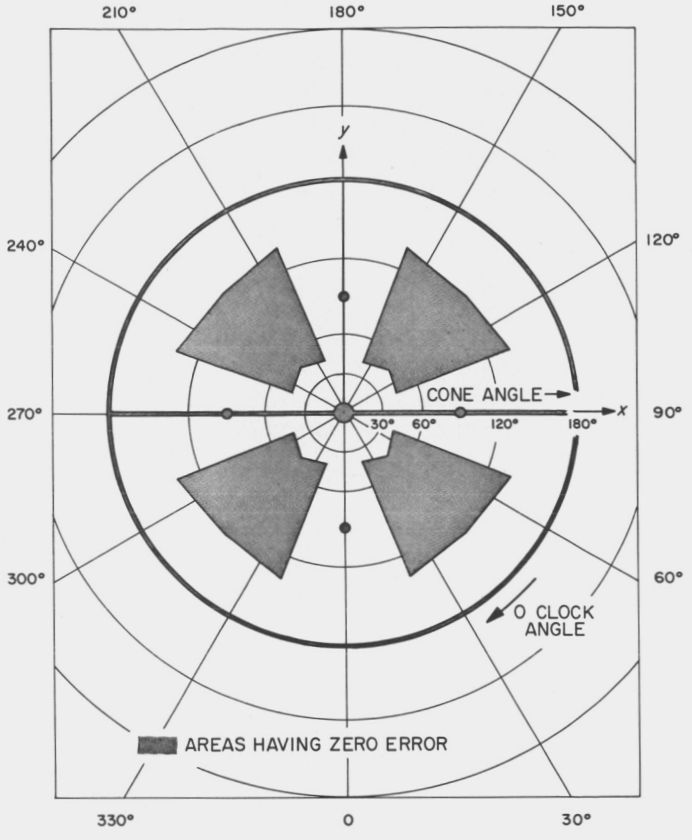

Fig. 37. 4π steradian Sun sensor error diagram

bar. These assemblies will be located on the dark side of two opposed solar panels. Integration of these two sensor systems will result in savings of both space and weight.

f. Guidance Sun sensor. The guidance Sun sensor will be flown aboard *Mariner* B for use during planet approach. Its function is to provide an accurate readout of the angle between the spacecraft roll axis and the Sun line. The angle between the spacecraft roll axis and the spacecraft planet line is determined by the approach planet scanner. These two angles are added to obtain the Sun probe planet angle. Starting approximately 10 days prior to planet encounter, this information will be sampled for use in determining the trajectory correction maneuvers.

The sensor is required to have an output which is linear to $\pm 10\%$ 3 σ over a range of ± 10 min. Figure 38 shows a Sun sensor test fixture having an adjustable length shadow bar. This device will be used to determine the optimum length between the cadmium-sulfide cell and the edge of the shadow bar which casts its shadow on the cell. The sensors scale factor increases as the shadow bar length is increased, but not proportionally.

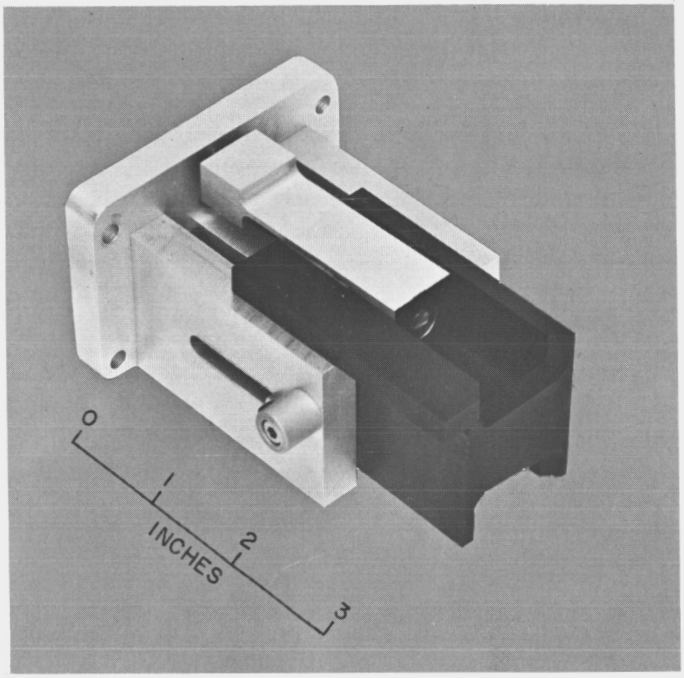

Fig. 38. Sun sensor test fixture

This is caused by the fact that the Sun is not a point source and its finite diameter causes the shadow to be less sharp when the shadow bar is moved away from the cell.

Although the test fixture in Fig. 38 is a single-axis device, the flight guidance Sun sensor will be designed to provide error signals about both the pitch and yaw axes.

6. Canopus Simulation

Adequate testing and calibration of the star sensor for use on the *Mariner* B spacecraft requires that a precise simulation be made of the star Canopus. The simulation should provide good collimation. The absolute spectral energy distribution should be within specified limits. The irradiance should be uniform, within specified limits, over the area to be used by the star sensor in testing.

Work has been initiated to provide a laboratory simulation of Canopus with the required characteristics. In a parallel effort, a program has been initiated to more precisely define the spectral irradiance of Canopus outside the Earth's atmosphere. Data from previous spectral measurements made of Canopus and other reference stars from the southern hemisphere are being reduced. It is anticipated that the spectral irradiance of Canopus be-

CONFIDENTIAL

tween 3800 and 5500 Å will be specified to an accuracy better than 5%, while outside this region the accuracy will be better than 10%.

The simulator will utilize a high-pressure xenon arc for a source. The spectrum of the source will be modified by suitable filters to more nearly approximate the Canopus spectral distribution. The condenser optics will be all quartz and an off-axis parabola will be used for collimation. The collimated star bundle will be 5 in. in diameter.

To calibrate the spectral irradiance of the Canopus simulator components are being procured to build a spectroradiometer. The spectroradiometer will utilize a Leiss double monochrometer to compare the simulator irradiance with the irradiance from a reference lamp spectrally calibrated by the National Bureau of Standards.

7. Horizon Scanner

Testing of the horizon scanner, previously reported in *SPS 37-9*, has continued. Figure 39 shows the horizon scanner, with the rear cover removed, mounted in a test fixture. This fixture allows precision alignment of the horizon-scanner mounting flanges with respect to a distant simulated planet. By using this fixture the optical axis can be adjusted to coincide with the mechanical axis. The fixture rotates the horizon scanner about its front nodal point to enable calibration of the error-output scale factor.

For testing of the horizon scanner for functional performance with environmental simulation, a space background simulator has been designed and fabricated. Figure 40 shows the horizon scanner mounted in the space background simulator. The simulator consists of an outside wall of foam insulation, a liquid nitrogen shroud, and an interior cavity which can be evacuated to less than 10^{-5} torr pressure. The interior of the cavity is treated to have a high emissivity. The interior surface area is large with respect to the uncooled area where the horizon scanner looks in, thus the simulator appears to be a black body with close to unity emissivity at a temperature of 77°K. The window of the horizon scanner also serves as the window to the simulator. To simulate a planet's radiance against the space background, a small heated conical cavity is located inside the large cooled cavity. The heated cavity can be set at any desired temperature for testing and absolute radiometric calibration of the horizon scanner.

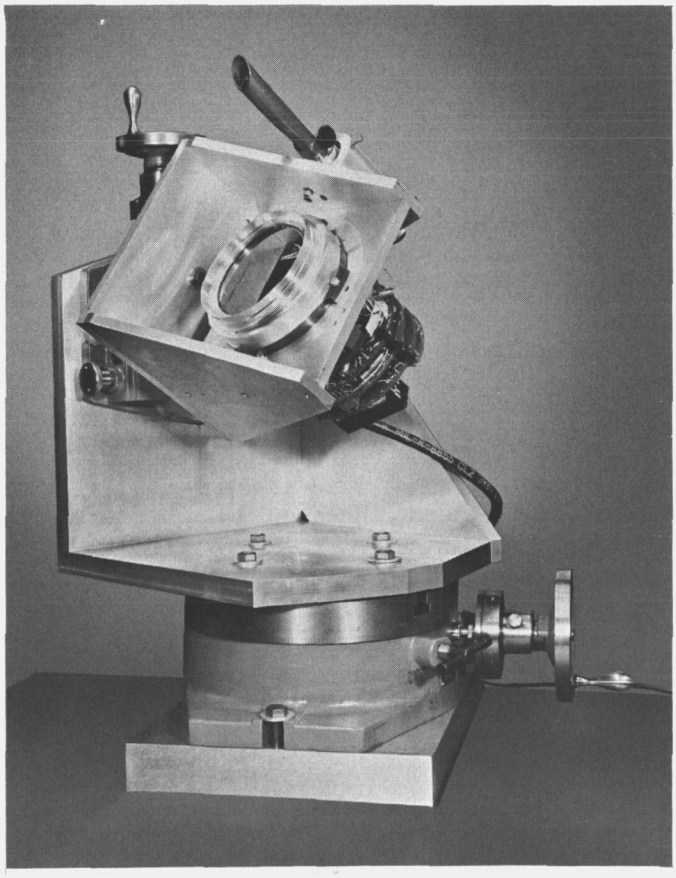

Fig. 39. Horizon scanner

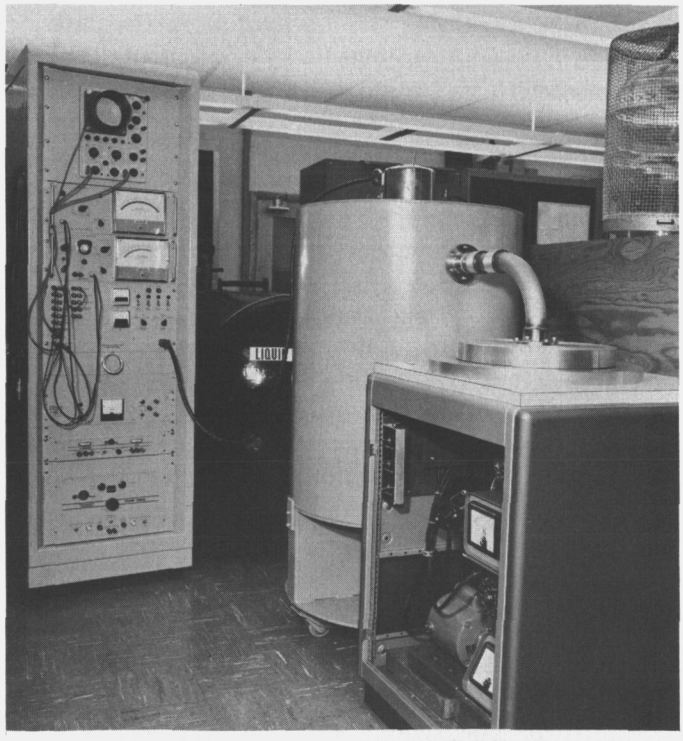

Fig. 40. Horizon scanner test

Preliminary tests with the simulator have confirmed the existence of a space background problem. The nature of the problem is that the over-all efficiency of the optical system (containing five elements of germanium: window, two wedges, objective and detector emersion element, all low-reflectance coated to peak at 12 μ) is approximately 20% for 300°K radiation. When the horizon scanner is looking at a homogeneous background, at a different temperature than the instrument is internally, any variation of the optical efficiency as a function of the wedge angle will result in a change of energy on the detector. This change will give an unwanted signal described as aperture modulation. The effect of this aperture modulation is to reduce the horizon scanner sensitivity by increasing the noise level. An investigation as to the cause of this aperture modulation as a function of wedge angle is being made. In addition, several approaches to compensate for the modulation, such as selected masking of the wedges and/or limiting the spectral response to the region of maximum transmission, are being investigated.

Additional environmental tests have included vibration and acceleration testing of the horizon scanner. Preliminary results indicate no mechanical failures in these tests.

8. *Image Dissector*

Three image dissectors, previously described in *SPS 37-12*, have been received from the contractor to date. Both functional and environmental testing is proceeding on the tubes. Figure 41 shows the test equipment for functional testing. The image dissector is mounted on a pair of rotary tables in such a manner that each table provides rotation in one axis about an identical point.

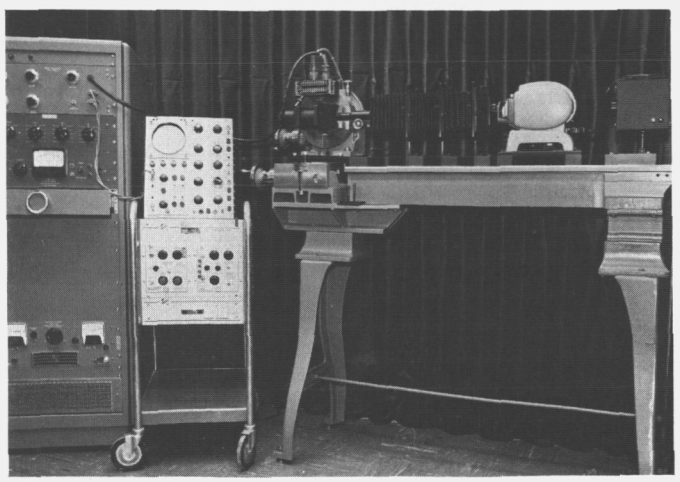

Fig. 41. Image dissector test

This point is chosen to be coincident with the center of curvature of the photocathode. An optical image in focus on the curved photocathode will thus remain in focus as the tube is repositioned. A microscope objective is used to form a reduced image, from the slide projector, on the face of the photocathode. For sensitivity measurements, the microscope objective and projector are removed. Light from a National Bureau of Standards calibrated source, located in the lamp housing shown at the end of the bench, is allowed to illuminate the photocathode.

Preliminary functional tests have given the following results. The deflection linearity over a ½-in. area of the photocathode is better than 1%. The resolution at the center of the photocathode is sufficient to give 30% modulation of a Bar chart with 2-mil spacing between the alternate black and illuminated bars. At ¼ in. from the center the modulation has decreased to 10% and degenerates badly further out. The useful area of the photocathode is thus considered to be approximately ½ in. and will be more specifically defined by the resolution requirements of the particular application of the tube. Since the sensitive area of the photocathode is approximately 1 in. in diameter, the useful area is determined by the electron optics limitations. The resolution does not appear to be improved by increasing the electron optics accelerating voltage in excess of 600 v.

An image dissector mounted in its housing has been subjected to the design qualification type approval vibration environment. No effects due to this environment were noticeable on subsequent retesting of the tube.

Work on development of a high-temperature photocathode for the image dissector was initiated. The purpose of this development was to provide a tube that would have the capability of withstanding sterilization temperatures (125°C for 36 hr) with no subsequent loss in sensitivity. Several tubes were constructed, using a bialkali photocathode of sodium potassium. These tubes did not meet the required sensitivity, having a response of 5 to 10 μamp/lumen (2870°K color temperature incident light) as compared to the 50 μamp/lumen from a typical S-11 photocathode. A change in the *Mariner* B design requirements has eliminated the need for sterilization capabilities in the initial systems using the image dissectors. These changes, together with the initial high-temperature photocathode difficulties, have resulted in a decision to proceed with the S-11 photocathode and to continue the high-temperature development effort on a reduced long-term basis.

Some initial studies have been made on the problems of the design of an optical system, with field corrector, to work with the curved (1¼-in. radius) photocathode. These studies have indicated that the use of a fiber optics face plate for the photomultiplier would ease the optical design problem and would also result in improved image quality. Work has been initiated to incorporate a fiber optics face plate into the image dissector.

9. Canopus Tracker

The Canopus tracker is designed to furnish the third axis reference for the *Mariner* B attitude-control system. It is a no-moving-parts device that promises to have the long lifetime necessary for planetary missions.

The heart of the system is an image dissector tube developed under JPL Contract 950096 by CBS Laboratories. This tube permits a slit-shaped portion (0.004 × 0.070 in.) of a photocathode (0.500-in. diameter) to be instantaneously examined by a 12-stage photomultiplier.

In use, an area of space equivalent to 4 × 32 deg is imaged on the face of the tube by a fast, wide-angle optical system. The 32-deg view angle is positioned on the spacecraft to include all possible Sun–probe–Canopus angles for trajectories roughly within the ecliptic plane. The portion of the cathode along the 32 deg is determined by the Canopus cone angle generator from inputs by CC&S predetermined program and by two modes of ground command backup.

The slit is effectively swept perpendicular to its long axis through 4 deg peak-to-peak by a 20-cps triangular wave. The tube output is a pulse train of 40 pulses/sec whose phase relationship to the sweep voltage determines the error signal about the roll axis. This roll error signal (Fig. 42) is produced by sampling the sweep voltage at the moment of the star pulses and holding this voltage between pulses. The triangular wave shape permits a high degree of rejection of offsets caused by sampling delays, variations in pulse characteristics, and variations in amplitude and frequency of the sweep voltage.

Figure 43 shows the tracker block diagram. Note that an internal signal representing star "color" for additional "identification" is *not* generated. S-11 magnitude and star cone angle (and to some extent cone-angle rate) are the only information used for Canopus identification (available to the star tracker itself). The threshold gates will be set at approximately a factor of ±2.5 from nominal calculated Canopus amplitude. In the event that the

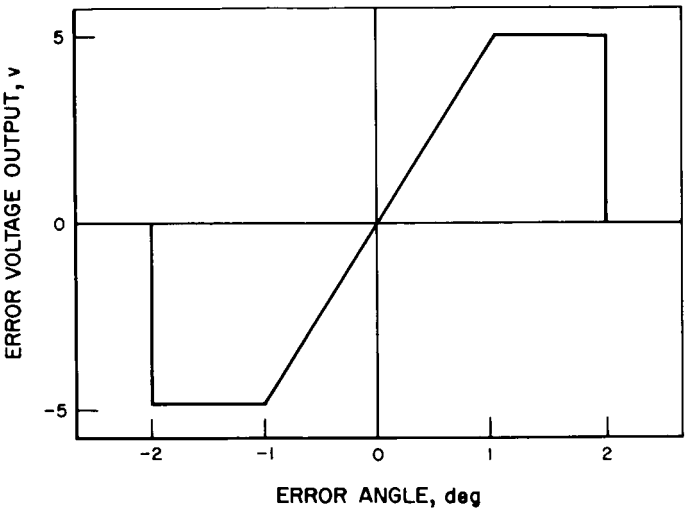

Fig. 42. Roll error signal

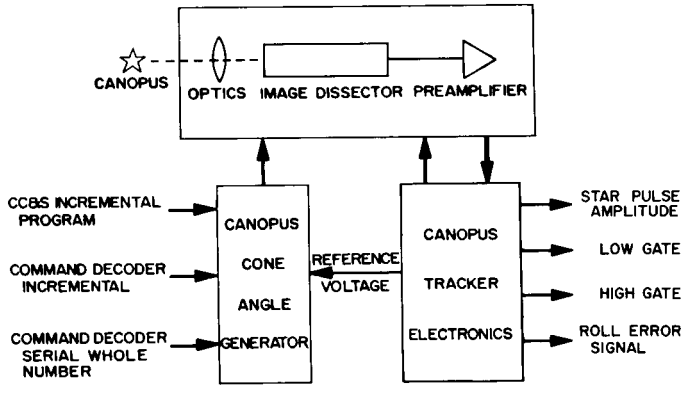

Fig. 43. Canopus tracker block diagram

wrong celestial object is acquired, command access through the omnidirectional antenna is available as a backup. In this event, a roll override command will be given and the spacecraft will begin a roll search for the next "acceptable" bright object.

The Canopus tracker is mechanically packaged in three portions with a total weight of about 7 lb. The tracking head containing the image dissector, optics, 45-deg mirror and lens shade, preamplifier and high-voltage supply is mounted to the side of the integrated guidance package in a special carrier designed to maintain alignment to the planet approach scanner. The two electronics portions, the Canopus cone angle generator and the Canopus tracker electronics are each packaged in *Mariner* B 1.25-in. standard modules. The electronics requires about 4 w of 2400 cps, 50 v rms. The entire tracking head can be rotated to permit different roll null positions and thus different nominal roll attitudes of the spacecraft.

The problems associated with development of the Canopus tracker have mostly concerned the image dissector because of the complexity of the device and the stringent requirements placed on its performance. A problem with optics because of the curved photocathode has been solved with a fiber optics faceplate. A problem with variations of sensitivity of the tube across its face may eventually require a specially graduated filter in front of the tube. A problem with voltage breakdown across the tube base has been solved.

Other problem areas where solutions are in sight are the fast wide-angle optics, mechanical stability and alinement of the tracking head, and electronic stabilities. Stability requirements of all kinds are very severe, not only for attitude control, but primarily for successful solution of planet approach guidance.

The development work has all been done at JPL or under JPL contracts. These include contracts to CBS Laboratories for image dissectors, the Te Company for optics, and DI/AN Controls for the Canopus cone angle generator. During development effort, a request for bids was initiated, with Barnes Engineering Company being the successful bidder for the fabrication and testing of complete Canopus trackers. During the final development effort, Barnes Engineering has their project engineer resident at JPL to ensure a smooth and rapid transition into the production phase for the Canopus tracker.

10. Relating Detector (or Sensor) Response From One Radiant Source to Another Through an Intermediary Standard

If an optical sensor such as a star tracker is to be accurately threshold-calibrated and it is not possible or is inconvenient to calibrate on the actual star, a simulator must be used. Ideally the simulator should have the same absolute spectral "output" as the star outside the Earth atmosphere. This is difficult, since present sources have spectral characteristics much different than a typical star. The following calculations indicate a practical approach of relating tracker response on one source to that on another source through an intermediate calibration (which would logically be the ft-candle or other convenient standard).

Assumptions.

Star or celestial reference "output" at the tracker location

$$k_2 f_2(\lambda) \quad \frac{\text{w}}{\text{cm}^2 \mu}$$

Laboratory simulator output

$$k_1 f_1(\lambda) \quad \frac{\text{w}}{\text{cm}^2 \mu}$$

Tracker response versus wavelength

$$k_3 f_3(\lambda) \quad \frac{\text{amp}}{\text{w}}$$

Area of collecting optic

$$A \quad \text{cm}^2$$

Star or celestial reference output in ft-candles at the tracker location

$$[930]\, 685 k_2 \int_0^\infty f_2(\lambda)\, V(\lambda)\, d\lambda$$

Simulator output in ft-candles

$$[930]\, 685 k_1 \int_0^\infty f_1(\lambda)\, V(\lambda)\, d\lambda$$

Eye response normalized to 1 at peak

$$V(\lambda)$$

Computations.

For tracker output when operated against simulator to be equal to the same as its output against the star

$$A k_1 k_3 \int_0^\infty f_1(\lambda)\, f_3(\lambda)\, d\lambda = A k_3 k_2 \int_0^\infty f_2(\lambda)\, f_3(\lambda)\, d\lambda \qquad (1)$$

and if simulator ft-candle flux equals R times the star ft-candle flux then

$$[930]\, 685 k_1 \int_0^\infty f_1(\lambda)\, V(\lambda)\, d\lambda = [930]\, 685 R k_2 \int_0^\infty f_2(\lambda)\, V(\lambda)\, d\lambda \qquad (2)$$

which implies

$$k_1 = \frac{R k_2 \int_0^\infty f_2(\lambda)\, V(\lambda)\, d\lambda}{\int_0^\infty f_1(\lambda)\, V(\lambda)\, d\lambda} \qquad (3)$$

substituting (3) into (1) yields

$$R = \frac{\int_0^\infty f_1(\lambda) V(\lambda)\, d\lambda \int_0^\infty f_2(\lambda) f_3(\lambda)\, d\lambda}{\int_0^\infty f_2(\lambda) V(\lambda)\, d\lambda \int_0^\infty f_1(\lambda) f_3(\lambda)\, d\lambda} \qquad (4)$$

The simulator should therefore be set at a ft-candle level that is R times the star ft-candle level. When this is done, the sensor response to the simulator will be equal to its response on the star.

Typical values of R are shown in Table 9, and are subject to individual variation in detector response, assumed Canopus curve, etc. They are, therefore, correct for published nominal values only.

Table 9. Typical values of *R*

Simulator source type	Tracker response	Celestial reference	*R*
Xenon	S-11 photomultiplier	Earth	1.334
Xenon	S-11 photomultiplier	Mars	0.876
Xenon	S-11 photomultiplier	Canopus	1.3
Xenon	S-11 photomultiplier	Sirius	1.47
Xenon	S-11 photomultiplier	Vega	1.75
Xenon	S-11 × LRES optics	Earth	1.33
Xenon	S-11 × LRES optics	Mars	0.9
Xenon	S-11 × LRES optics	Canopus	1.28
Xenon	S-11 × LRES optics	Sirius	1.43
Xenon	S-11 × LRES optics	Vega	1.64
Xenon	S-4 × LRES optics	Canopus	1.34
Xenon	S-4 photomultiplier	Canopus	1.31
Xenon	silicon cell × LRES optics	Sun	0.828
Xenon	silicon cell	Sun	0.442
2750°K black body	S-11 × LRES optics	Canopus	2.31
6000°K black body	S-11 × LRES optics	Canopus	1.155
2750°K black body	S-11 photomultiplier	Earth	2.68
6000°K black body	S-11 photomultiplier	Earth	1.162

D. Telecommunications

1. Antennas

Two basic types of antenna systems are required for the *Mariner* B project. An omnidirectional antenna system is used for short range communication with the spacecraft, during mid-course maneuvers, the period of time when the spacecraft is not attitude-stabilized, and during various emergency modes. A high-gain antenna is used at ranges beyond which the omnidirectional antenna system is adequate.

The omnidirectional antenna system is to be operable at both 2113⅝ and 2295 Mc. For Venus missions, the required pattern coverage is within a hemisphere centered on the spacecraft axis and pointed toward the top of the spacecraft. For Mars missions, the hemispherical coverage required is in the opposite direction (aft of the spacecraft). A system using a turnstile antenna mounted at each end of the spacecraft can probably provide the needed coverage. For normal trajectories, only one of the antennas would be in use, depending on the mission. If for some reason the spacecraft enters a nonstandard flight situation and the spacecraft orientation is such that the antenna in use no longer can radiate sufficient power toward the Earth, the spacecraft can switch to the second antenna, which would now be looking toward the Earth in response to either high-power Earth command or from internal recognition of an extended received signal drop-out.

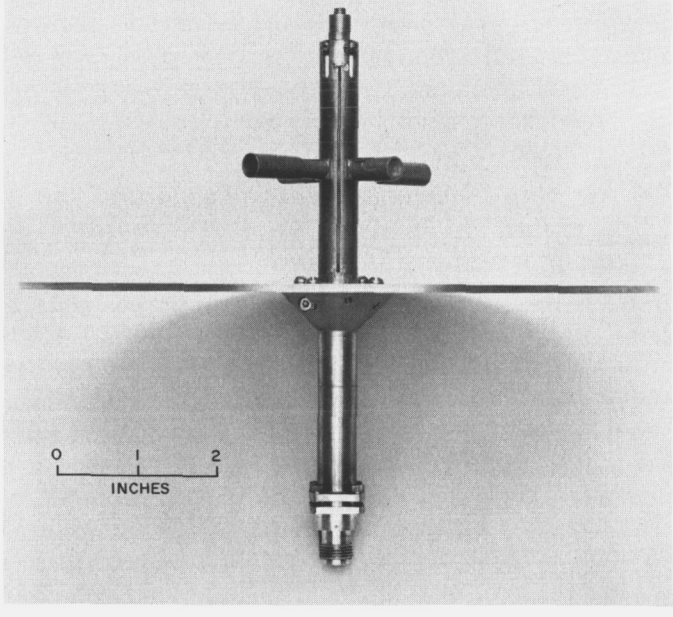

Fig. 44. Turnstile antenna

As seen in Fig. 44, the turnstile antenna consists of a pair of crossed dipoles mounted on a split-tube balun. This assembly is then mounted over a ground plane. Tests are now in progress to determine methods to shape the radiation patterns of the turnstile antennas. It is very desirable to have the patterns drop off quite rapidly

beyond their hemispherical coverage to minimize interference with the spacecraft.

E. Space Sciences

1. Scientific System

The *Mariner* B scientific system is composed of diverse instruments whose variety indicates the exploratory nature of these probes. Table 10 lists the instruments chosen to be flown at some time during the *Mariner* program.

The scientific instruments can be divided into three categories according to their location on the spacecraft. These categories are: (1) the main spacecraft superstructure (bus), (2) the capsule, and (3) the planetary horizontal platform (PHP).

a. Bus instruments. The bus instruments consist of an integrated set of particles and fields experiments which operate continuously from spacecraft/boost-vehicle separation, through the planetary encounter period, and until the spacecraft "dies" or is programmed into silence. Within the particles and fields experiments there are three separate categories: (1) the magnetometer, (2) the cosmic dust or micrometeorite detectors, and (3) the energetic particle detectors.

The last category consists of radiation experiments capable of detecting either charged particles or high-energy photons, or both. Some of the sensors have narrow-angle apertures and are used as directional monitors. Other sensors have wide-particle acceptance angles and are used to determine the interplanetary background. The energy ranges covered by the various instruments are indicated in Fig. 45. This overlapping coverage permits correlation between instruments and increases the directional coverage possible with a minimum number of instruments.

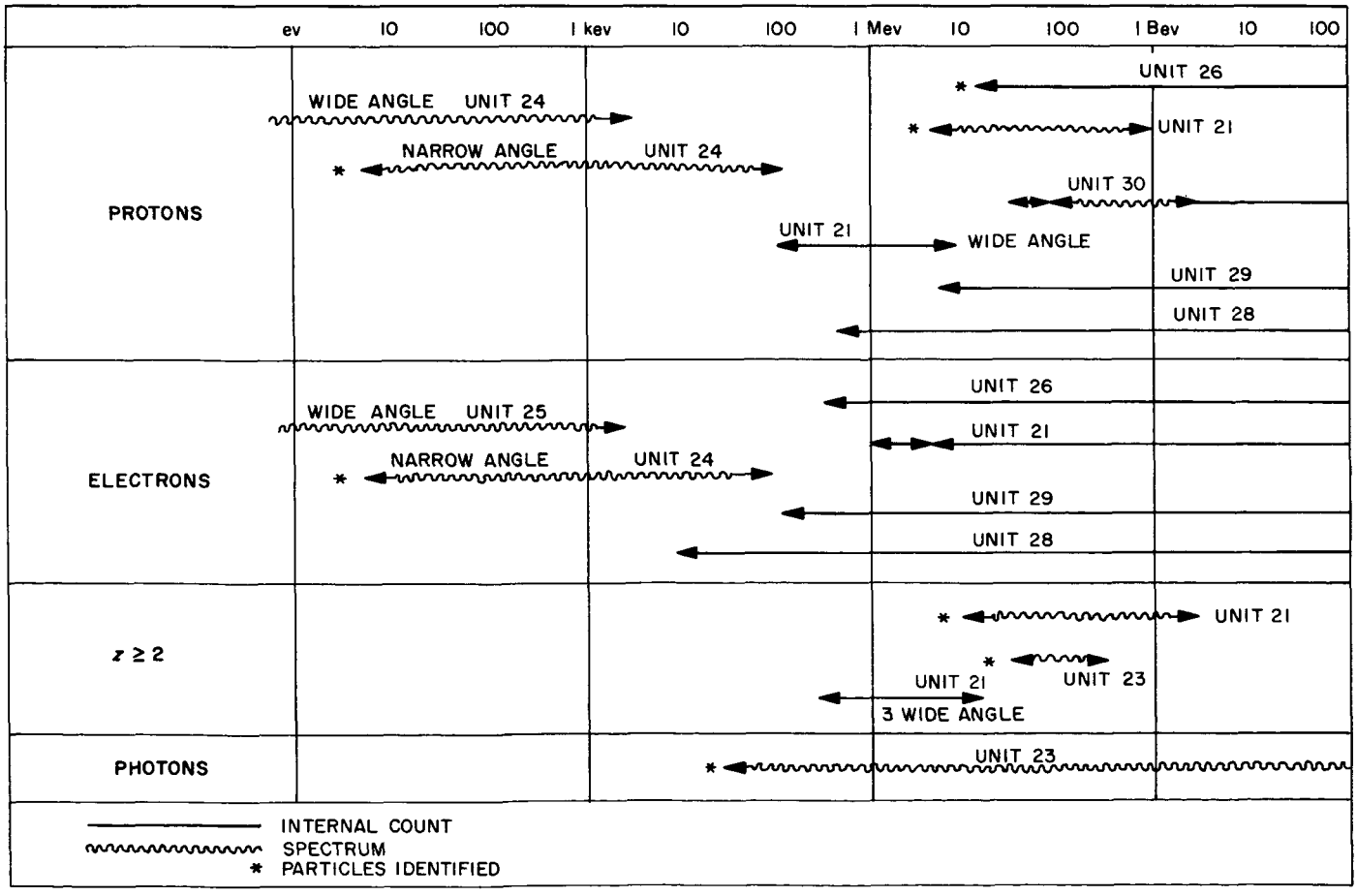

Fig. 45. Energy ranges of radiation experiments

Table 10. Bus experiments for *Mariner–Centaur* missions

Unit No.	Experiment	Experimenters	Cognizant scientist, Cognizant engineer	Primary purpose
36	Television system	Leighton (CIT) Sharp (CIT) Murray (CIT)	R. Newburn D. Allen	Mars mission: Obtain high resolution pictures of Mars surface. Weight = 35 lb; power = 16.5 w.
37	IR spectrometer	Kaplan (JPL) Neugebauer (JPL) Sagan (Berkeley) Weaver (Berkeley)	G. Neugebauer D. LaPorte	Mars mission: Obtain high resolution geographic correlations of "Sinton" CH bands; determine atmospheric H_2O, CO_2, CO content; determine atmospheric T-P structure. Weight = 25 lb;power = 9 w.
41	IR radiometer	Kaplan (JPL) Neugebauer (JPL) Sagan (Berkeley) Weaver (Berkeley)	G. Neugebauer S. Chase	Mars mission: Make temperature mapping of surface. Venus mission: Clouds plus surface mapping. Weight = 3 lb; power = 2.5 w.
35	Microwave radiometer	Barrett (MIT) Copeland (ABMA) Jones (JPL/CIT) Lilley (Harvard)	D. Jones F. Barath	Venus mission: Determine origin of centimeter radiation, determine H_2O abundance below cloud layer, make thermal map of surface. Weight = 31 lb; power = 6.4 w.
34	UV spectrometer	Barth (JPL) Wallace (Yerkes Obs)	H. Spinrad E. Mackey	Venus, Mars (?) mission: Determine O_3, O_2, N_2 content of upper atmosphere; look for aurora. Weight = 25 lb; power = 6 w.
28	Trapped radiation detectors	Van Allen (SUI)	C. Snyder L. Parker	Mars, Venus mission: Determine extent and intensity of planetary radiation belts. Weight = 3 lb; power = 0.5 w.
33	Magnetometer	Coleman (NASA) Davis (CIT) Jones (JPL/CIT) Smith (JPL)	E. Smith B. Connor	Interplanetary, Mars, Venus missions: Measure interplanetary magnetic field intensity and low frequency fluctuations; determine extent, intensity, and configuration of planetary field. Weight = 11 lb; power = 8 w.
32	Micrometeorite detector	Alexander (GSFS) Bohn (Temple U) Fuchs (Temple U)	M. Neugebauer E. McMillan	Interplanetary mission: Measure micrometeorite energy and momentum distribution. Weight = 8 lb; power = 1 w.
21	Cosmic ray spectrum analyzer	Simpson (U of Chicago)	C. Snyder S. Chase	Interplanetary mission: Measure energy spectrum of 1-400 Mev protons and angular distribution of 0.5-20 Mev solar protons; determine spectrum of α particles and high atomic number particles. Weight = 18 lb; power = 2-5 w.
26 27	Ion chamber and particle flux detector	Anderson (JPL) Neher (CIT)	H. Anderson L. Parker	Interplanetary mission: Monitor protons of >10 Mev plus electrons >0.6 Mev. Weight = 5 lb; power = 0.5 w.
30	High energy proton directional monitor	McDonald (GSFC)	C. Snyder W. Hodges	Interplanetary mission: Measure angular distribution of >50 Mev protons. Weight = 4 lb; power = 0.35 w.
29	Medium energy proton directional monitor	Van Allen (SUI)	C. Snyder L. Parker	Interplanetary mission: Measure angular distribution of >3 Mev protons. Weight = 3 lb; power = 0.4 w.
25	Low energy plasma probe	Rossi (MIT) Bridge (MIT)	C. Snyder W. Fawcett	Interplanetary mission: Monitor spectrum of 0-10 kev plasma protons; measure crude angular distribution. Weight = 18 lb; power = 3.8 w.
24	High energy plasma probe	Snyder (JPL)	C. Snyder J. Lawrence	Interplanetary mission: Monitor spectrum of 0.01-20 kev plasma protons; measure medium-fine angular distribution in near solar directions. Weight = 10 lb; power = 1.5 w.
22	Ultraviolet-visual polarimeter	Deirmendjian (Rand) Sekera (UCLA) Gehrels (U of Arizona) Teska (U of Arizona)	G. Neugebauer L. Parker	Mars mission: Measure polarization of light scattered from atmosphere. Weight = 10 lb; power = 3 w.
43	Faraday cup	Mozer et al (Aerospace)	C. Snyder F. Schutz	Interplanetary mission: Measure electron and proton energies from 1-50 kev. Weight = 3 lb; power = 3 w.
44	Articulating narrow angle plasma probe	Albert (LRL) Hill (LRL) Snyder (JPL)	C. Snyder F. Schutz	Interplanetary mission: Extend directional measurements of the high energy plasma probe.
39	Top-side sounder	Knecht (NRL) Sperber (AIL)	D. Jones F. Barath	Mars mission: Investigate upper planetary ionosphere using radar bounce. Weight = 25 lb; power = 1 w.
38	Low-frequency radio receiver	Haddock (U of Michigan)	D. Jones F. Barath	Interplanetary, Mars, Venus missions: Measure radio emission between 0.1 and 20 Mc. Weight = 9 lb; power = 2 w.
42	Spinning sub-satellite magnetometer	Coleman (NASA) Davis (CIT) Jones (JPL/CIT) Smith (JPL)	G. Neugebauer F. Schutz	Interplanetary, Mars, Venus missions: Measure interplanetary magnetic fields of 0.1 gamma and greater by removing magnetometer probe from main vehicle.

Table 10. Bus experiments for *Mariner–Centaur* missions (cont'd)

Unit No.	Experiment	Experimenters	Cognizant scientist, Cognizant engineer	Primary purpose
45	Planetary ionosphere and interplanetary medium	Garriott (Stanford) Eshleman (Stanford) Peterson (Stanford) Villard (Stanford)	D. Jones F. Schutz	Interplanetary, Mars, Venus missions: Investigate planetary ionospheres and interplanetary medium utilizing phase-locked radio receiver and ground based transmitters. Weight = 8 lb.
23	Stacked crystal spectrometer	Rosen (STL)	C. Snyder R. Wengert	Interplanetary mission: Monitor protons of energies between 250 kev and 40 Mev and electrons above 250 kev.

Table 11. *Mariner* B Mars capsule instrumentation

Unit No.	Experiment	Experimenter	Cognizant scientist, Cognizant engineer	Description
61	Atmospheric thermodynamics		R. Sloan D. Adamski	Determination of temperature, pressure, density and velocity of sound.
62	Simple composition		E. Franzgrote R. Wengert	A number of small, simple instruments to measure specific gases.
63	Gas chromatograph		V. Oyama F. Wilhite	Total spectrum instruments to analyze for nearly all gases that may be present in the Martian atmosphere.
64	Mass spectrometer		C. Giffin S. Rothman	
65	Television		R. Newburn D. Allen	
66	Organic chromatograph		V. Oyama F. Wilhite	Will analyze a soil sample for its organic constituents, presumed to come from living material.
67	Multivator	J. Lederberg	G. Hobby J. Stuart	Determination of enzymes, growth, or organic compounds using optical or electrical measurements.
68	Radiation package		W. McDonald S. Chase	
69	Radioisotopic biochemical probe	G. Levin N. Horowitz	G. Soffen F. Schutz (tent.)	Detects life by monitoring a metabolic process using radioisotopes.
70	Abbreviated microscope	J. Lederberg G. Soffen	G. Soffen J. Stuart	Used to view microorganisms and particulate matter in the atmosphere.
71	Macromolecule analyzer		G. Hobby (tent.) F. Schutz (tent.)	Detection of proteinaceous macromolecules would strongly indicate living organisms.

b. Capsule instruments. The instruments which are being considered for possible use with either a 1964 or post-1964 entry capsule are listed in Table 11. The greatest emphasis for the 1964 Mars capsule mission will be placed on the atmospheric thermodynamics and atmospheric composition experiments. A minimal biology experiment will also be flown on the first capsule. This will be a gross type of organic sampler and will yield information on the possibility of life, but will not necessarily verify its existence.

The atmospheric thermodynamics instrumentation will attempt to determine the temperature, pressure, and density of the planetary atmosphere. By taking frequent readings during the descent, a profile will be established that will permit the design of better and more reliable capsules.

Three types of instruments are being studied for use in the analysis of composition of the planetary atmospheres. Two instruments, the mass spectrometer (Unit 64) and the gas chromatograph (Unit 63) will make a complete analysis of the major gaseous atmospheric constituents. The third, simple composition (Unit 62), consists of small individual instruments, each designed to measure a specific gaseous constituent. A decision as to which instruments will be produced for flight will be made following completion of the study/breadboard contracts.

The selection for the 1964 mission may have to be based on capsule power and communication capabilities rather than on scientific merit.

Five instruments are being considered for performance of the biological experimentation after capsule impact with the Martian surface:

(1) Radioisotope biochemical probe.

(2) Microscope.

(3) Multivator.

(4) Macromolecule analyzer.

(5) Organic gas chromatograph.

The radioisotope biochemical probe is used to detect life by monitoring radioactive carbonaceous gases that are generated as a result of biological metabolic processes. A growth medium is prepared incorporating C^{14} glucose and formate. As the organisms metabolize the medium, the C^{14} appears in the respired gases. This is precipitated on a membrane and measured with a solid state radiation detector.

The macromolecule analyzer will be used to detect the presence of proteins or protein-like substances which are highly indicative classes of chemicals making up the machinery and structural architecture of living terrestrial organisms.

The organic gas chromatograph will analyze a sample of soil for its organic constituents by either volatilizing the stable smaller compounds or pyrolizing the sample and breaking the large molecules into smaller more volatile molecules.

The multivator will perform soil sample tests for: (1) enzyme assay, (2) growth, and (3) organic analysis. Approximately 9 to 18 reaction vessels can be used, each of which may be used to perform one of the tests.

An abbreviated microscope will be used to view particulate matter present in the planetary atmosphere in a search for identifiable micro-organisms.

c. PHP instruments. The experiments on the PHP are planet-orientated. During the 1964 Mars encounter period, three experiments on the PHP will be emphasized: (1) the television (Unit 36), (2) the IR radiometer (Unit 41), and (3) the IR spectrometer (Unit 37). The TV and IR spectrometer will observe the sunlit side of the planet and will operate between initial planet acquisition

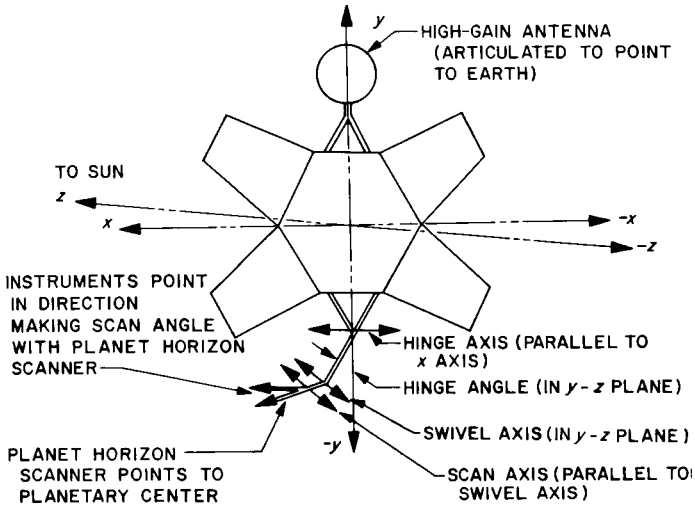

Fig. 46. Spacecraft pointing angles

and the time the terminator is crossed. The IR radiometer will be sampled during the entire period of planet acquisition. During the Venus encounter in 1966, the microwave radiometer (Unit 35), UV spectrometer (Unit 34), and the IR radiometer (Unit 41) will be emphasized.

The PHP is oriented (Fig. 46) such that the instruments scan about the center of the planetary disk. This is accomplished by the use of an infrared device that continuously scans the horizon with a rosette pattern and holds the disk center within ± 1 deg. The planetary scan system is an instrument capable of scanning off the center of the planet in approximately 0.1-deg steps to ± 300 deg. This scanning is controlled by a program in the data automation system (DAS). The particular scan program used during the encounter period will be selected from a set of 15 to 20 programs stored in the DAS on the basis of pre-encounter trajectory data.

Data will be taken by the PHP instruments at times called "stops" when the scan angle is held at a fixed value. During any given stop, any combination of the PHP instruments can be operated. As an example, during a typical stop planned for the Mars mission, the following sequence will occur:

(1) IR radiometer is sampled.

(2) IR spectrometer scans twice between 3.3 and 3.8μ.

(3) IR radiometer is sampled.

(4) IR spectrometer scans between 1.7 and 2.7μ.

(5) IR radiometer is sampled.

(6) TV low-resolution green picture taken.

(7) TV high-resolution picture taken.

(8) TV low-resolution blue picture taken.

(9) TV high-resolution picture taken.

(10) TV low-resolution red picture taken.

(11) Steps 1 through 5 repeated.

This sequence will take approximately 255 sec. During events 6 through 10 the particles and fields experiments can be sampled because the delivery of television data to tape storage is independent of the DAS programming.

A typical Martian encounter scan program is shown in Fig. 47. The solid lines give the angular planet diameter as a function of time. More complex programs are within the capabilities of the programmer, but it is not likely that they will be attempted on the early *Mariner* missions. In Fig. 47, steps 1 to 5 above are listed as "IR Sequence."

In addition to programming the PHP and its associated instruments during the encounter period, the DAS will also sequence, sample, and store data from all of the bus "particle and fields" experiments. The information thus obtained will be correlated with IR, TV and capsule data to yield a comprehensive picture of the planetary environment. This is done easily because accurate time correlation is a function already mechanized within the DAS. It is expected that bus and IR instruments will acquire between 5 and 10 million bits of data during a typical encounter program. The television will be sampled as required to take 100 pictures (100 million bits of data).

During the period from solar acquisition to encounter, the DAS will operate the "particles and fields" experiments under programs comparable to those used during encounter. During the first few weeks, it is planned to take several million bits of data from these instruments. As the spacecraft moves farther away from the Earth and the bit rate is reduced, the active program will be changed to reduce the amount of information accumulated. Toward the end of the mission the acquisition rate will drop to approximately 400,000 bits/day.

d. Data automation system. Several units of the science system on board the spacecraft are not experiments. One is the DAS (Unit 20). The DAS makes practical the acquisition of high rate data that would be impossible utilizing real-time telemetry. The DAS also makes possible the inter-relation and correlation of all the science on a chronological and phenomenological basis. This is particularly true during events such as solar flares and plasma streams.

The DAS consists of three elements: (1) buffer or temporary storage, (2) a programmer, and (3) a tape machine. The input buffer storage of some 10^4 bits allows temporary storage of data while other scientific data are being read into the tape machine or while tape machine is playing back earlier data to the telemetry channel. The 10^4-bit tape/telemetry buffer acts in the following manner:

(1) Accepts data from the input buffer at a high rate and then transfers it to the tape storage upon demand.

(2) Accepts data from the tape machine and transfers it to telemetry on a bit-by-bit basis.

Item (2) makes it possible for the DAS to respond to any telemetry bit rate planned for the *Mariner* missions.

The programmer is mechanically and electrically identical to the buffer storage devices; only the input and output logic is different. The active program of approximately 10^4 bits is rapidly circulated within this device and, as a specific command word is identified by time comparison, it is acted upon by the associated command matrix. The net result is that each instrument is instructed when to read-out, when to change its operational range, when it is to be sampled, or when its operation is no longer desired. Inactive program storage of 40 to 100 different programs is possible through the use of a 10^6-bit tape machine. These programs are selected by ground command and allow compensation for variations from the nominal trajectory, the interplanetary medium, and changes or failures in operation of the scientific instruments. They also permit special modes of operation or high sampling of rates for certain instruments.

The programming flexibility of the DAS allows full exploitation of the scientific instruments. This is accomplished through interleaving the data of related experiments so as to increase the value of the information gathered.

A DAS program contains up to 255 instructions, any one of which can be executed at any specified one of 690,000 times per day. The number of such programs stored in the DAS will be in excess of 40, and different

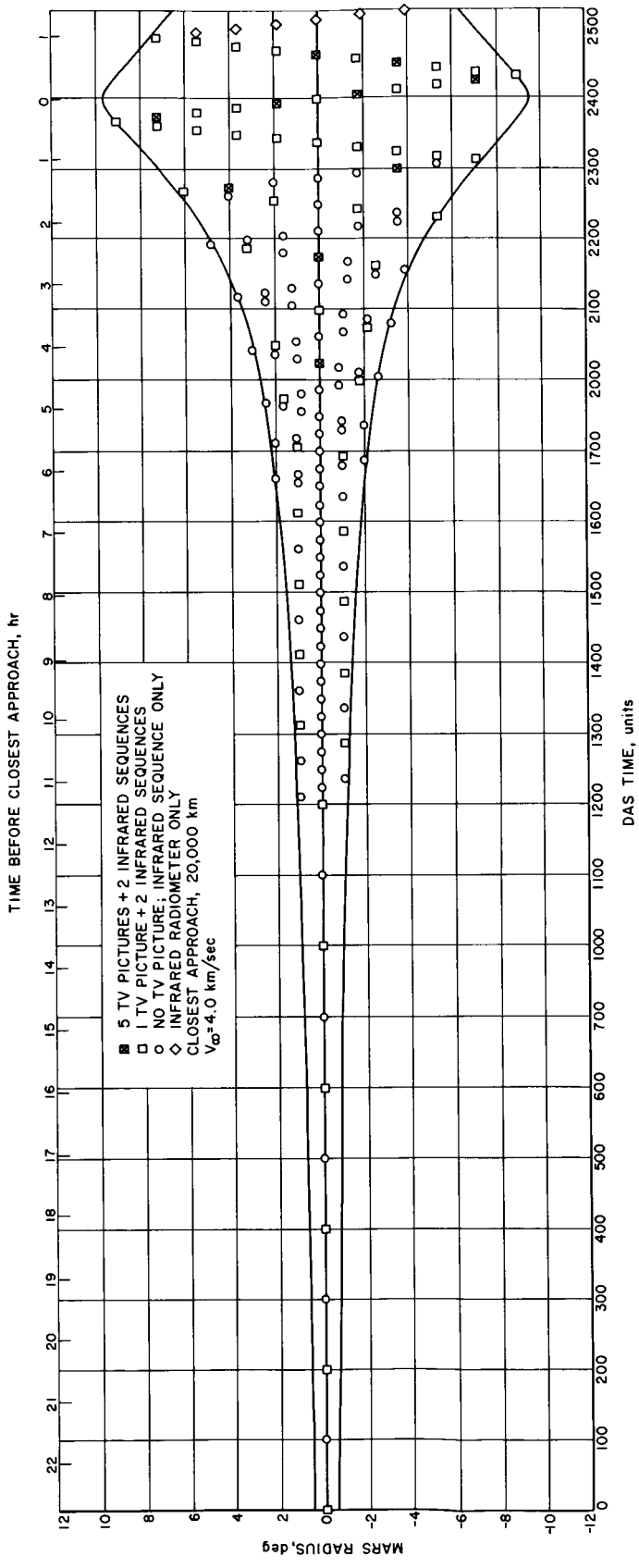

Fig. 47. *Mariner B* Mars scan sequence

programs can be called for by command from Earth or activated automatically by another DAS program. In addition, an entirely new program can be read into DAS storage by radio command from Earth, in case unusual circumstances should make such a step desirable.

The key to this flexibility is the provision for as many as 16 separate subprograms in each DAS program. Any one of these can be initiated or terminated as often as desired. For example, in the sample encounter program already discussed, seven of the subprograms are assigned to general control functions, e.g., they specify the scanning sequence and the timing of events within a certain interval. Thus, subprogram SP-0 is in command for approximately the first 12 hr, SP-1 for the next 6 hr, SP-3 for an hour on either side of closest approach, etc. The remaining subprograms operate and sample specific experiments (those which require unusually high data rates, spectral scans, rapid stepping from one energy to another, etc.), and are initiated and terminated by the control program currently in effect. Two such subprograms are required for the IR sequences in the DAS program that has been studied; two may be required for TV; two for magnetometer sequences; and two for plasma measurements. Other experiments, having simpler command structures, are operated by the control subprograms alone.

Another important capability of the DAS which is provided by its subprogram structure is that of reacting to certain preselected changes in the environment. Examples of this capability which will be utilized during the interplanetary phase of the mission are the "flare mode" and "plasma mode" of operation. Certain charged particle sensors, in response to an increase in their counting rate such as might be produced by a stream of particles emitted by a solar flare, can signal the DAS and immediately initiate a new preset control program which samples, at a high rate, those experiments expected to be of interest at such a time. A special control mode for making high-rate plasma measurements can likewise be initiated by one of the plasma sensors. As another example, a signal from the planetary horizon seeker could signal the DAS to take a TV picture immediately upon planetary acquisition instead of waiting for an arbitrary preset time.

For these externally triggered modes of operation, automatic lockouts are provided in the DAS to prevent their continuous or too frequent actuation by high background levels or sensor failure. These lockouts can be released only by radio commands from Earth.

The tape storage device permits storage of millions of bits of scientific data. Since the rate of data accumulation is not predictable and since the acquisition bit rate varies widely from instrument to instrument, it is necessary that the DAS store this data until the telemetry channel can be made available for transmission to Earth. Data is normally read into the tape machine from the 10^4-bit tape/telemetry buffer; but television data at an 83.3-kc bit rate is read directly into the machine on seven parallel tracks. All of the data transferred from tape to telemetry, however, is sent out through the tape/telemetry buffer.

e. Scientific power switching. The scientific power switching (Unit 40) acts as a sequencer for the spacecraft power system to the science instruments (Fig. 48). The planet science primary power is controlled by the DAS through the power switching, and the backup power turn-on of planet science by CC&S is also accomplished in this unit. It is necessary that the motors of the IR spectrometer and radiometer (Units 37 and 41) be turned off during TV operation because the vibration of the PHP will smear the pictures. The squibs for the UV and IR spectrometer (Units 34 and 37) covers are controlled by the DAS.

f. Data conditioner. The last special instrument is the data conditioner (DCU, Unit 50). This device performs the following functions:

(1) Divides the normal 0- to 6-v analog signals of selected low data rate experiments by two so that they can be sampled by the engineering commutator, digitized, and transmitted in real time.

(2) Provides logarithmic shift registers for reading out specific experiments in real time, or at times determined by the telemetry bit rate.

(3) Provides standard scalers for some of the instruments.

(4) Provides a flare mode trigger to the DAS when the background of the interplanetary medium exceeds preset thresholds.

(5) Acts as a junction box between these experiments and the DAS. Prevents dc ground loops and minimizes ac ground loops.

2. Television Subsystem

The *Mariner* B television subsystem is to consist of a two-camera system, employing a high-resolution, narrow-angle telescope, along with a wide-angle lens unit. Each camera is to be a shuttered system utilizing a "slow-scan"

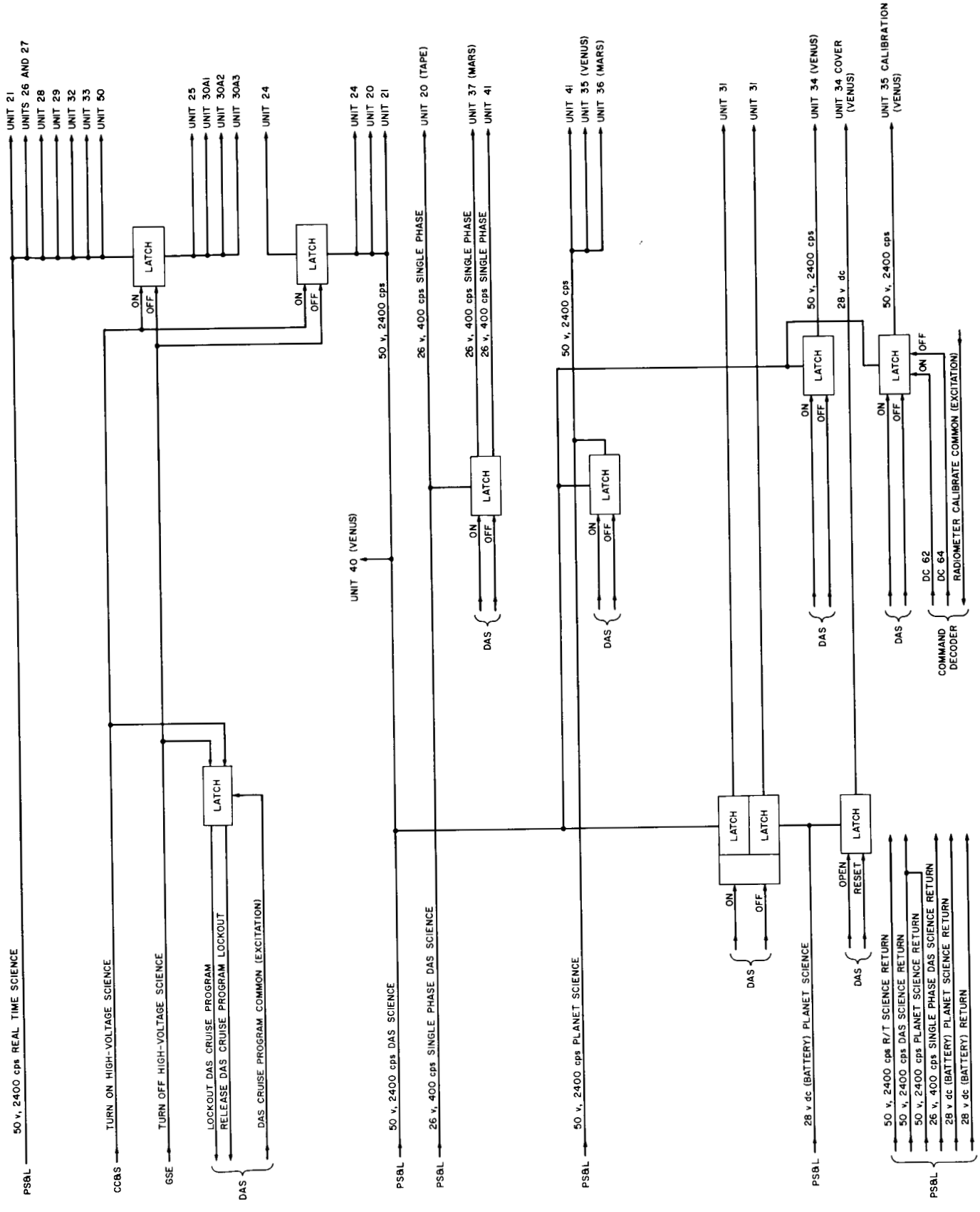

Fig. 48. *Mariner* B Unit 40 functional block diagram

CONFIDENTIAL

vidicon capable of storing an image for at least 15 sec. The entire subsystem will be logically controlled and synchronous with a 1-Mc clock. The cameras will operate continuously after power has been turned on, the data being read out sequentially, one camera after the other. Total mission storage of 100 pictures is to be provided with the selection of which picture to store controlled by a preset program. The TV data is to be telemetered to Earth at a minimum bit rate of 21 bits/sec requiring about 13 hr to transmit one complete picture. A 400-scan line raster is to be used with resolution capability of 400 picture elements per line. A square aspect ratio is to be utilized scanning a 0.44×0.44-in. square on the vidicon faceplate. A vertical resolution of at least 280 TV lines can be expected with 400-scan lines.[c] The active line duration (T) is to be 28.8 ms yielding a highest instantaneous frequency of:

$$f_{max} = \frac{n}{2T} = \frac{400}{57.6 \times 10^{-3}} = 6.95\,\text{kc}$$

where n is the number of picture elements resolved per line.

It was found convenient to utilize an 8.1-ms dead time at the end of each line to enable a tape machine to stop and start on playback. This mechanization greatly simplifies the data readout operation into an output buffer.

Due to the fact that the *Mariner* B system is power-limited, it was decided that the highest probability of success could be accomplished with a digital system. An analog-to-digital encoder was therefore designed and constructed along with camera control functions, so that a synchronous TV camera would result. It was decided to use conventional pulse code modulation (PCM) techniques with 6 bits per picture element. It is recognized that more exotic schemes exist for digitizing TV-type data, but it was believed that the safest system would be a PCM system at the time the decision was made. Figure 49 shows a comparison of the analog and digital data using the *Mariner* B breadboard camera and encoder.

a. Block diagram. Figure 50 is a simplified functional block diagram of the subsystem showing the PHP, bus and data handling interfaces. The equipment on the PHP has been held to a minimum so that PHP vibration frequencies would be as high as possible with small displacements. The PHP, therefore, contains only those portions of the camera that must be physically close to the vidicon sensor, due to signal level and shielding considerations.

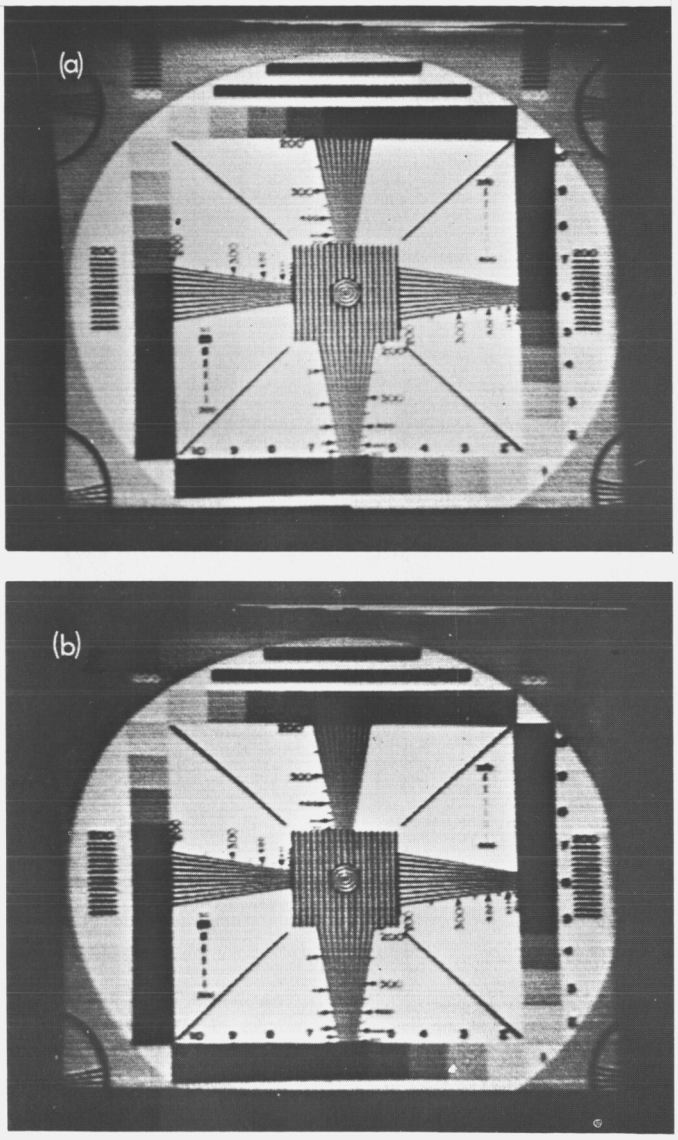

Fig. 49. Digital (a) and analog (b) field presentation

A 125-kc beam modulator is used, resulting in an amplitude-modulated RF carrier system for the signal channel (*SPS 37-15*). This oscillator is common to both cameras. Each camera is shown with voltage distribution circuitry where filtering and decoupling is accomplished. A preamplifier is used to boost the signal level sufficiently high to preserve a good signal-to-noise ratio when coupled to the bus electronics. Engineering temperature measurements will be made of the vidicon faceplate, thus enabling calibration data to affect final picture analysis.

[c] From Fink, D. G., Television Engineering, 2nd ed., pp. 26–32.

CONFIDENTIAL

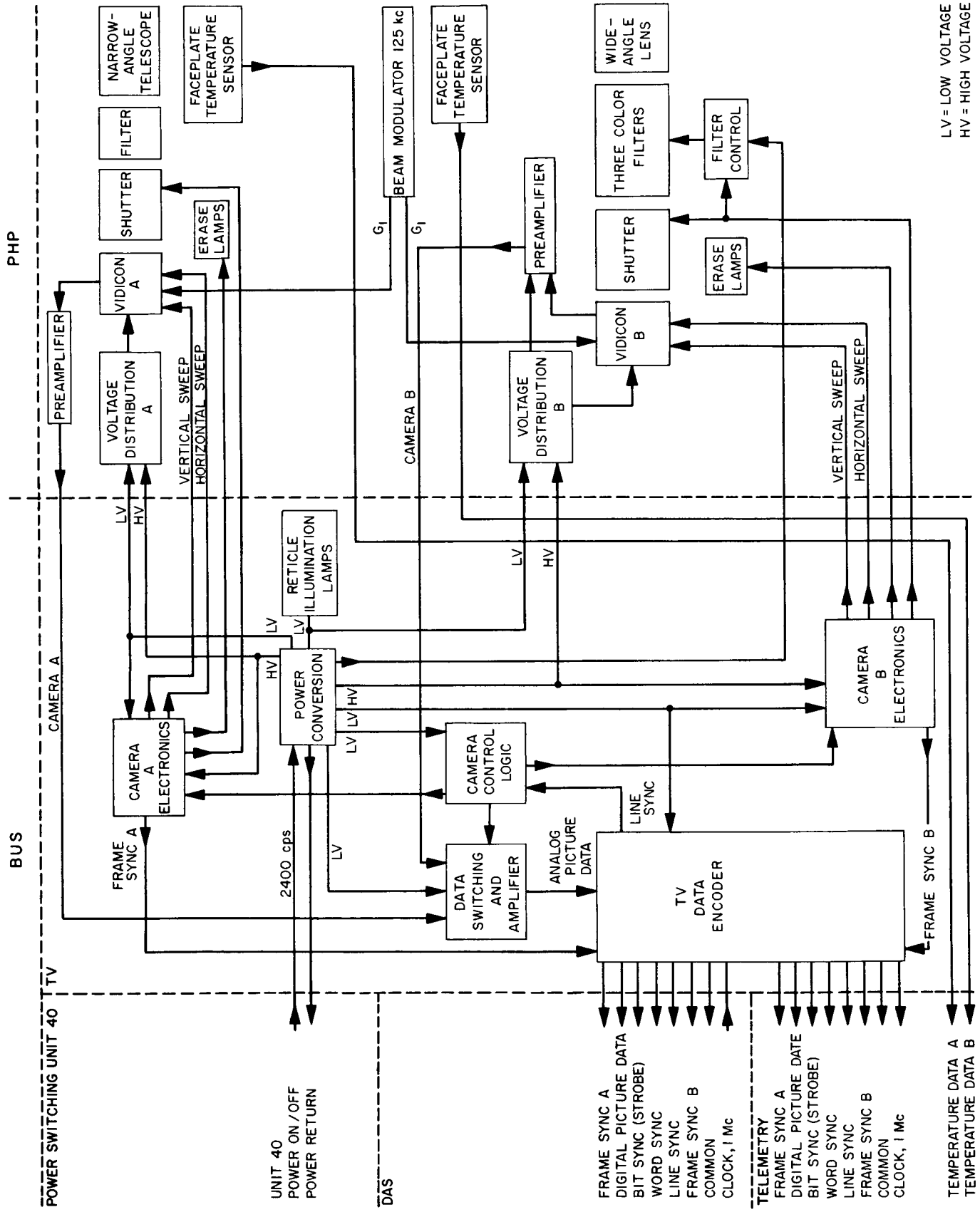

Fig. 50. TV subsystem functional block diagram

The bus will contain all of the additional electronics to operate the two vidicon cameras. Sweep circuitry, erase lamp control, shutter control and G_1 control for each camera are located in blocks labeled "Camera Electronics." The erase and G_1 control functions will be discussed in more detail later.

The camera control logic section contains the necessary logic to control both cameras as shown in the simplified timing diagram (Fig. 51). Waveforms *A*, *B*, and *C* constitute a set for camera A and B control functions. The data coupled to the encoder is controlled by the control logic as shown in Fig. 50.

The analog data is sent to the encoder where it is converted to digital form and coupled to both DAS and telemetry. The encoder supplies a "line rectangle" to the camera, controlling the start and stop of each line. This synchronizes the system so that the first word the encoder digitizes is the first word of a line. This line sync information is also coupled to DAS and telemetry so that proper identification can be inserted in the data. It is anticipated that a sequence with a high correlation factor (such as a P-N sequence) be inserted with the data at the proper time so that a suitable sync pulse be generated on the ground for controlling a display device. This P-N generator is not to be a portion of the TV subsystem.

Word (picture element) sync, bit sync, and frame sync will also be provided as outputs. The TV system contains a 1-Mc clock that is phase-locked to the DAS clock and free runs if the DAS input should fail. The current thinking is that the clock output be made available to telemetry if needed.

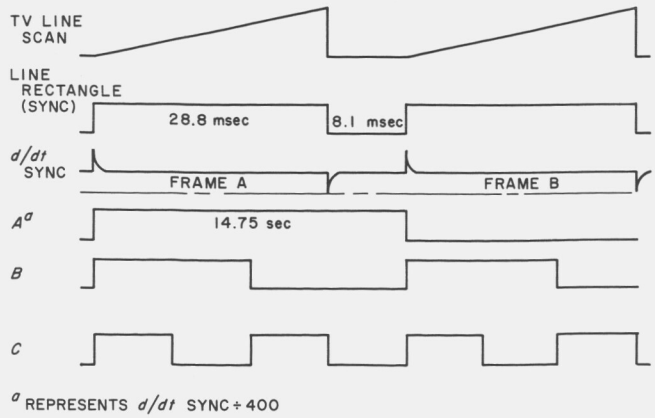

Fig. 51. Simplified timing information

A transformer–rectifier (T–R) section will be provided to convert the basic 2400-cps square wave power to the voltages necessary to operate the cameras.

The TV subsystem is entirely transistorized, except for the vidicon tube. The system, including all optical elements, will weigh about 35 lb with a power requirement of about 16 w.

b. Vidicon tube. A vidicon tube was selected as the camera pickup device because of ruggedness, light weight, small size, and simplicity. An all-electrostatic unit was selected, due to a savings of 2 lb over an all-magnetic system, as well as reduced magnetic interference problems. The tube can use completely transistorized circuitry. A developmental tube along with an electrostatic and magnetic unit are shown in Fig. 52 as a comparison. The tube under development at General Electrodynamics Corporation is known as an Ebicon, incorporating a standard electrostatic vidicon along with an imaging section. It is hoped that a tube such as the Ebicon be incorporated in future missions, due to the expected increase in sensitivity compared to a vidicon.

The operation of a vidicon is based on photoconductivity. This effect produces a change in electrical conductivity with variations in incident light intensity. The vidicon faceplate inside surface is coated with a transparent conductive coating, as indicated in Fig. 53. A photoconductive layer is deposited over this coating. This material, when in the dark, is a reasonably good insulator, but becomes conductive when exposed to light. An elec-

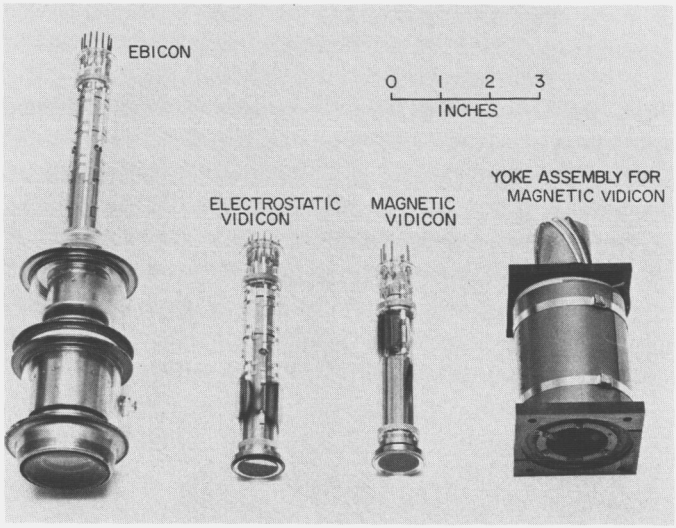

Fig. 52. Vidicon tube comparison

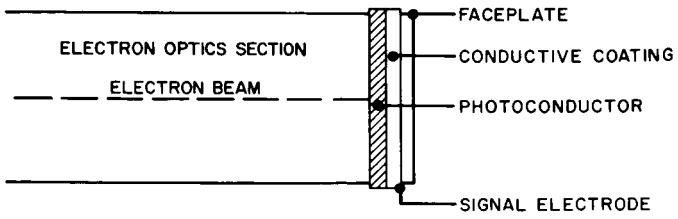

Fig. 53. Vidicon target section

tron beam is made to scan the back surface by the electron optics section.

The front surface of the photoconductor is held at a positive potential with respect to the cathode by applying voltage to the transparent coating. The scanning electron beam deposits a negative charge on the photoconductor back surface. Charge is accumulated in dark areas due to the high resistance of the photoconductor until the back surface reaches cathode potential. This is known as "priming" the vidicon.

Where light from the scene falls on the photoconductor, conductivity increases, reducing the negative charge at the illuminated point. The photoconductor, therefore, becomes charged much like a capacitor in a pattern corresponding to the scene image. As the electron beam scans the back surface, it will release electrons into the less negatively charged areas, and the resultant varying electron flow constitutes the video signal current.

The vidicon being used has a specially-developed photoconductor which allows an image to be stored for a period of 10 to 20 sec. The photoconductor has high-spreading resistance and trapped-carrier characteristics.

An erase and prime system had to be incorporated in the system, since it is basically a shuttered photographic system. Each scanned image must be erased, to not interfere with the next image. The erasure is accomplished by flashing lights on the back side of the photoconductor, thus eliminating the variation in charge pattern that may exist from the preceding image. The vertical sweep is then operated at a 4-kc rate while the current density of the beam (G_1 control) is increased, thus priming the photoconductor for the next shuttered image.

An optical black mask is to be provided on the face of the vidicon to establish a true optical black for each frame. Fiducial markings will be located on the vidicon face to assist in data conditioning and analysis on the ground.

c. Analog-to-digital encoder. The analog-to-digital converter portion of the encoder consists of an amplitude-to-time converter in which 1-Mc pulses are counted. The word resulting from the amplitude-to-time conversion, therefore, indicates the gray shade of the particular picture element.

The pulses that are gated from the converter are counted in a 6-bit accumulator, transferred in parallel to a serial shift register, and shifted out at an 83.333-kc rate.

The digital data output is of the NRZ type as defined by Richards,[d] where discrete voltage levels are assigned to ones and zeros as opposed to modified NRZ where a change is represented as a one.

Since 6 bits are available to identify the amplitude of any picture element, 2^6 or 64 quantization levels result. It should be pointed out that this does not represent 64 "shades of gray," since a shade of gray is defined as a change in intensity of $2^{1/2}$. Sixty-four shades of gray therefore would represent an over-all intensity ratio of 65,536:1.[e]

This number is clearly beyond the capability of any photographic process, including television. The RETMA test pattern shown in Fig. 49 is designed to have an over-all intensity variation of 32:1, thus giving 10 shades of gray.

It is believed that the range of illumination from the sub-solar point to the terminator of Mars could be on the order of 100:1. According to the preceding discussion, this results in:

$$(2)^{x/2} = 100$$

Taking the logarithm of both sides gives

$$\log (2)^{x/2} = \log 100$$

$$\frac{x}{2} \log 2 = \log 100 = 2$$

$$x = \frac{4}{\log 2} = \frac{4}{0.301} = 13 \text{ shades of gray}$$

A dynamic range of 100:1 on a vidicon is a somewhat unknown area, so that gain control as a function of aver-

[d] From Richards, R. K., Digital Computers and Circuits, Feb. 1958, p. 328.

[e] 1 shade of gray is a $2^{1/2}$ change in intensity. Therefore, we have $(2)^{x/2} = y$ where x is the number of gray shades and y is the over-all intensity ratio. Assuming $x = 64$ gives $(2)^{64/2} = (2)^{32} = 65{,}536 = y$.

age illumination is being considered for the *Mariner* B camera. This implies that whatever the contrast ratio of a particular scene, the encoder would linearly quantize the range into 64 separate levels.

d. Optics. The optical portion of the TV subsystem (*SPS 37-15*) contains the following components:

(1) Camera A telescope.

(2) Camera B lens system.

(3) Shutters.

(4) Camera A fixed filter.

(5) Camera B three-color filter system.

The Camera A telescope is to be of a standard Cassegrain configuration of a nominal 100-cm focal length with an effective focal ratio of $f/5.1$. A TV line separation of 1 km on the surface of Mars should be possible at a distance of 10,000 km, if the PHP vibration does not become a limiting aperture.

Camera B will have a 7-in. focal length $f/3.5$ lens with a possible line separation of 4.5 km under the same condition as described before. Camera B will be fitted with a three-color filter system to obtain colorimetric information from the planet and its atmosphere.

The shutters will be of a rotary disc type. Nominal shutter times of 40 msec for Camera A and 100 msec for Camera B are planned.

A fixed filter will be used with Camera A to filter out any UV and deep blue radiation below 0.42 μ. This will prevent the haze effects of the Martian atmosphere from affecting the contrast of surface markings seen by the high-resolution camera.

A mockup of Camera A is shown in Fig. 54. The dome houses the electronics and serves as a thermal shield. The structure is 20 in. long and 10 in. in diameter.

e. Packaging. Thermal problems for those portions of the TV subsystem mounted on the PHP are of particular interest, since they are expected to be in the shade. The actual temperature affects the vidicon parameters; thermal gradients are of concern for the optics portion.

Good numbers do not yet exist for the ambient, but it is expected to be less than 0°C. The TV system sensitivity will be optimized as close as possible to the expected

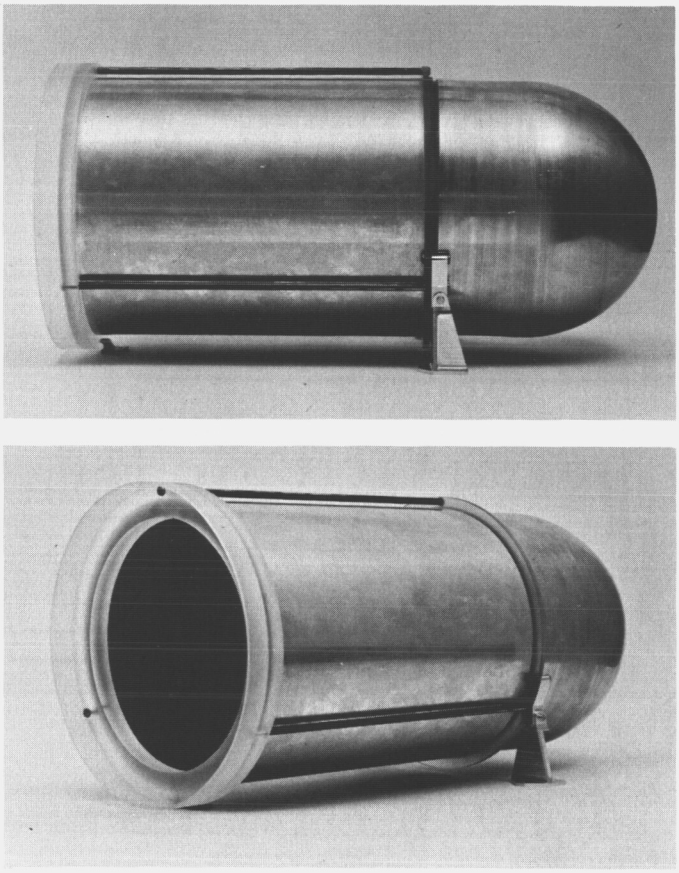

Fig. 54. Camera A mockup

ambient, but operation less than, or equal to 0°C is considered risky and somewhat of an unknown at present. The 1-w vidicon filament dissipation will be used to supply as much heat to the faceplate as possible. This will be done by thermal coupling and isolation from the telescope.

Early prototype drawings are being generated at the present time, with special emphasis given to:

(1) RF shielding and isolation within the camera.

(2) Flexibility, ease of assembly and repair.

(3) Minimum PHP weight.

(4) Temperature control.

(5) Mechanical integrity.

f. Test and acceptance. A complete system breadboard without optics is to be constructed to demonstrate system feasibility, assist in developing test specifications and packaging procedures. The Camera A system has been completed; the pictures of Fig. 49 show early operation.

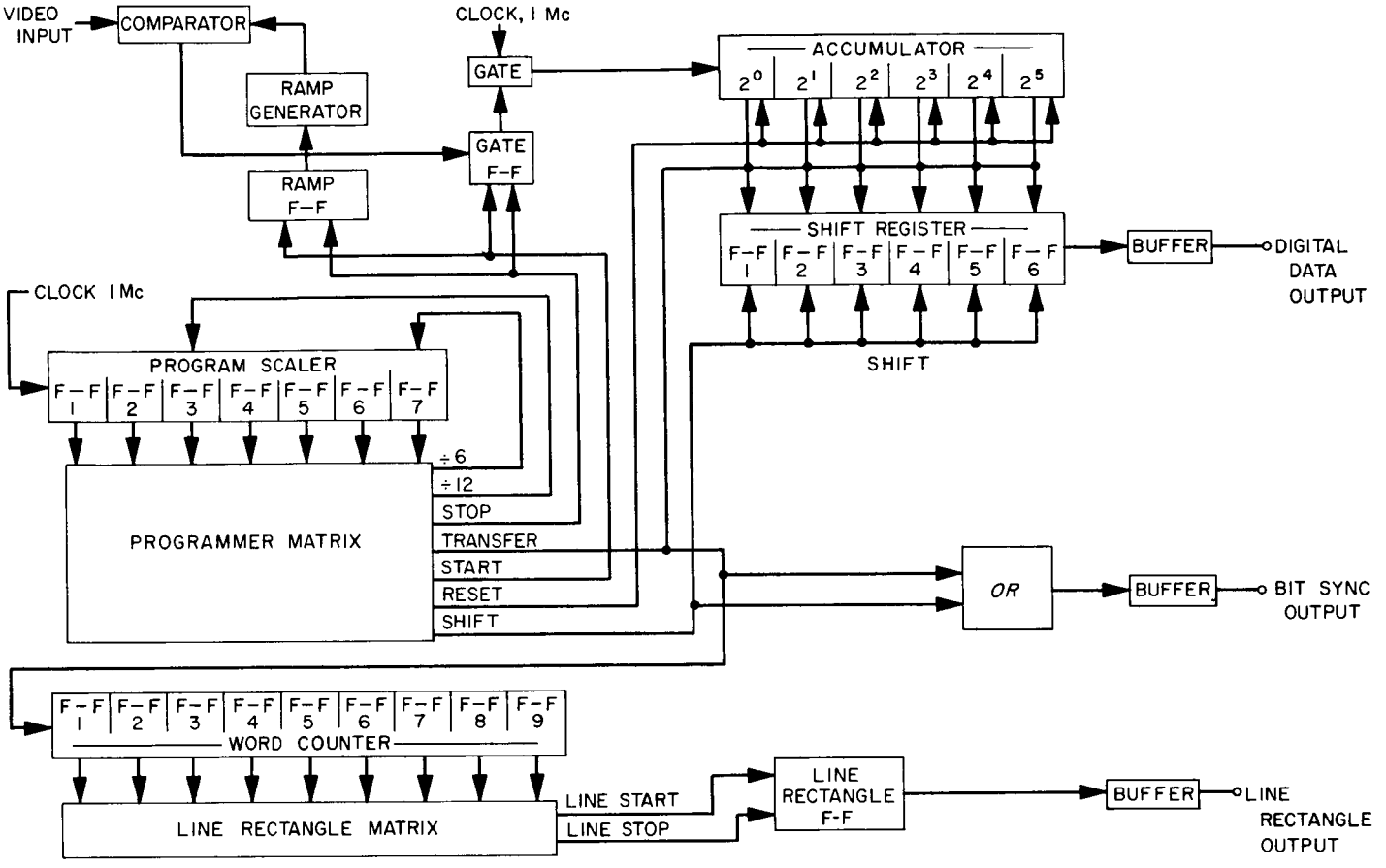

Fig. 55. Video encoder subsystem block diagram

Test racks will be constructed that will completely activate and display all necessary functions, as well as the TV field. These racks will help insure repeatability and consistency of tests to be performed.

3. TV Analog-to-Digital Encoder Subsystem

The video information originating in the *Mariner* B TV cameras occupies a frequency band from dc to 6.9 kc. It is desired to convert this analog information into a serial PCM signal before transmission from the spacecraft.

To preserve the high frequency content of the video information, the sampling rate of the encoder must be at least twice the highest frequency of interest. The sampling rate is therefore chosen at 13.9 kc. In addition, it is desired to recognize at least 64 different voltage levels in the analog video. The encoding is therefore accomplished on a 6-bit word basis.

Each 6-bit word defines the amplitude of one element; 400 such elements, plus 112 more for retrace time, constitute a complete TV line. Thus, each TV picture or frame may be broken down into 400 lines, consisting of 512 6-bit words, making a total of $400 \times 512 \times 6$ or 1,228,800 bits per picture.

In order to attain the sampling speed required, the encoder operates at a basic clock rate of 1 Mc. This basic frequency is divided down in the encoder to provide bit, word, and line repetition frequencies.

a. System block diagram (Fig. 55). The heart of the encoder is in the programmer. Within this unit are generated the timing pulses necessary for correct sequencing of the encoder operations. Since the encoder must sample 13,900 times per second, the programmer repeats the same sequence of pulses every 72 μsec.

The cycle of operation of the encoder begins when the programmer sends a "start" pulse from its matrix. This pulse sets the ramp flip-flop on, and begins the generation of a positive-going linear sweep in the ramp generator. Simultaneously, the "start" pulse sets the gate flip-flop

on and opens the gate between the 1-Mc clock and the accumulator.

If the video present at the comparator input is between 0 and 1.6 v, and changing slowly compared to the ramp, the gate will remain open for a time and the accumulator will count the gated 1-Mc clock. When the ramp passes through the video voltage level, the comparator (a high-gain differential amplifier) switches state and emits a sharp pulse. This pulse signifies equality of the ramp voltage and video voltage, and closes the gate. The greater the video voltage, the longer is the time before the ramp equals this voltage, and thus the longer the gate remains open.

The closure of the gate thus finds the accumulator, which is a binary counter, with a total count proportional to the amplitude of the video signal. If the video exceeds 1.6 v, the ramp-video equality will not occur, and the gate will not close. This would cause the accumulator to overflow, since it has a capacity for only 64 clock pulses. To prevent this from occurring, a "stop" pulse is sent to the gate flip-flop, closing the gate before the accumulator can overflow. The "stop" pulse simultaneously terminates the ramp waveform.

Next, the "transfer" pulse causes the state of each flip-flop in the accumulator to be duplicated, in parallel, in each shift register flip-flop. Since the state of the last (2^5) accumulator flip-flop is transferred to the last shift-register flip-flop, the transfer operation "creates" the first bit at the digital output terminal. This is the most significant bit of the word.

Every 12 μsec thereafter, the shift pulse causes the data to shift to the right in the register. Thus each data bit "exists" at the output for 12μsec and is then replaced by the next most significant bit. Immediately after the transfer operation, the accumulator contents are no longer important, so it is reset to await the next gated clock sequence.

The gate, gate flip-flop, and comparator have a certain minimum time in which they can respond to signals. This time is on the order of two clock pulses. This implies that a minimum video signal, i.e., 0 v, will still allow two pulses to enter the accumulator. To correct this inconvenience, the accumulator is reset to -2, rather than to 0.

There are five shift pulses sent to the shift register during the generation of a word. The "sixth shift pulse" is absent, because during this time the transfer is taking

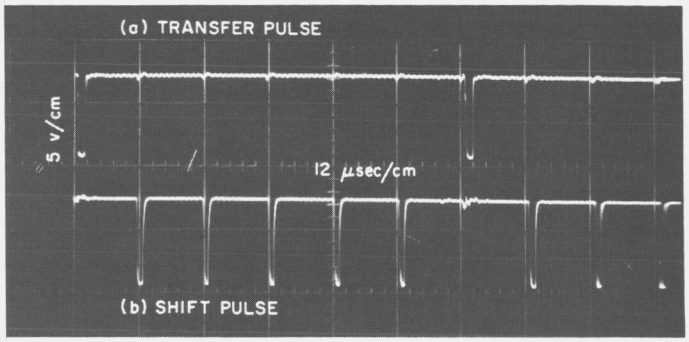

Fig. 56. Shift pulses

place. In order to provide a bit sync pulse, the transfer and shift pulses must be added together (logical "OR") to give a sync pulse for each bit (Fig. 56).

The remainder of the encoder is devoted to the generation of a line rectangle used in the cameras for line sweep synchronization. The operation is similar to that of the programmer. The line rectangle is positive from the first to the 400th word and zero from the 400th to the 512th word, whereupon the cycle repeats.

The encoder uses silicon semiconductors, in some cases multiple devices containing more than one transistor. It has been operated satisfactorily at temperatures from -40 to 80° C ambient. The total power consumption is approximately 1 w.

b. Encoder accuracy. When the output of an analog-to-digital encoder does not exactly represent the input signal, then an encoding error is created. Encoder errors fall into two groups: (1) errors inherent in the digitizing process, and (2) errors common to the particular encoder design.

In the first group are errors caused by a finite sampling rate (frequency response), and the step nature of the output caused by finite resolution.

The second group includes linearity error, encoding delay and changes in gain or drift with temperature.

The linearity of the encoder has been measured by noting the input voltage required to produce each successive word at the output. The deviation of each input voltage from the best straight line fit is shown in Fig. 57. The greatest deviation in all cases is less than 3 mv. Compared to a full-scale input of 1.6 v, this represents an error of approximately $\pm 0.2\%$ in linearity. The linearity of the encoder is dependent chiefly upon the linear

CONFIDENTIAL

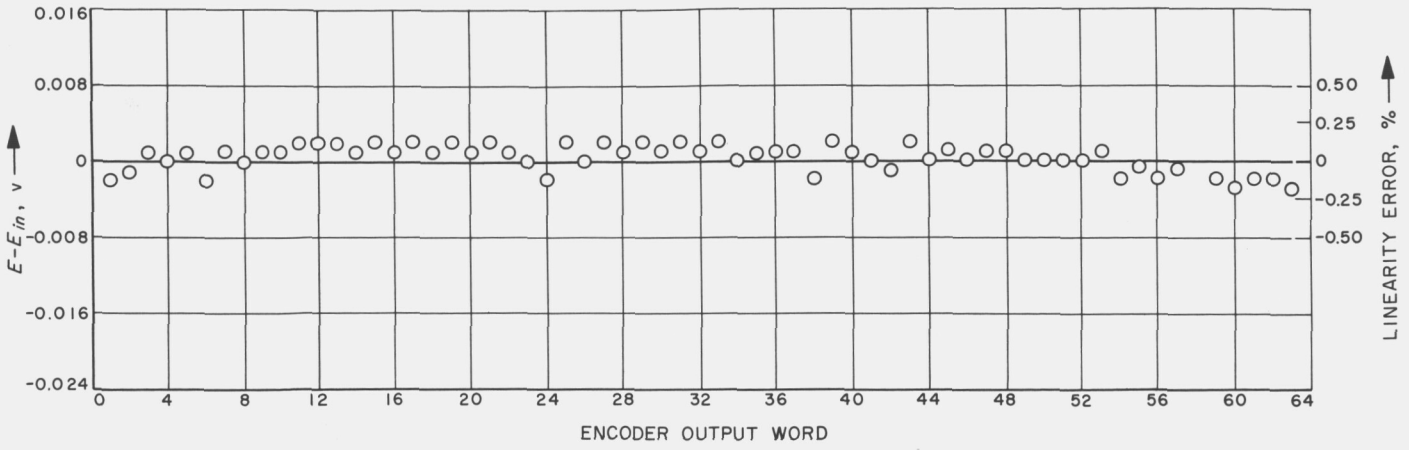

Fig. 57. Encoder linearity curve

sweep from the ramp generator. This non-linearity seems quite acceptable when compared to the encoder resolution of 1.7%.

c. Encoder waveforms. Figures 58 through 62 are photographs of various waveforms existing in the encoder. Figure 57 is the linear sweep and the rectangular wave used to generate this sweep. Figure 59 displays the condition of the gate flip-flop (upper) while the encoder is sampling a fixed dc voltage of 0.225 v, or the ninth video level. Eleven gated clock pulses (center) result in a digital output (lower) of 001001 binary or 9 decimal.

When the digital output of the encoder is connected to a suitable decoder, the decoder output may be compared with the encoder input, as in Figs. 60, 61 and 62. Figure 60 (upper) shows the encoder–decoder response to a 100-cps sinewave (lower).

Figure 61 is a photograph of the response to a 6.9-kc sinewave. The phase of the input signal with respect to one-half the encoder sampling frequency has been adjusted momentarily for maximum response. The encoder is sampling the sinewave close to the peak of each half-cycle. If the encoder were sampling the sinewave at points midway between the peaks, the decoded output would be a straight line. Figure 62 is a display of a typical TV line. The original signal is below and the decoded signal above. The encoder has been set to divide the full analog input into about 60 discrete levels. The time from the beginning to the end of the line is about 28 msec.

4. Electrostatic Camera Tube Considerations

Where power economy and payload weight are of prime concern, as in *Mariner* B, an electrostatically-

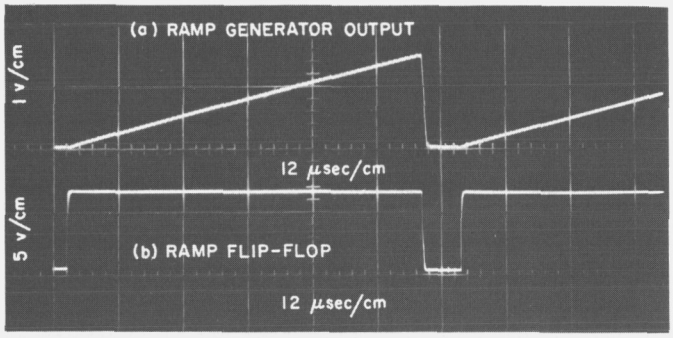

Fig. 58. Ramp generator response to ramp flip-flop

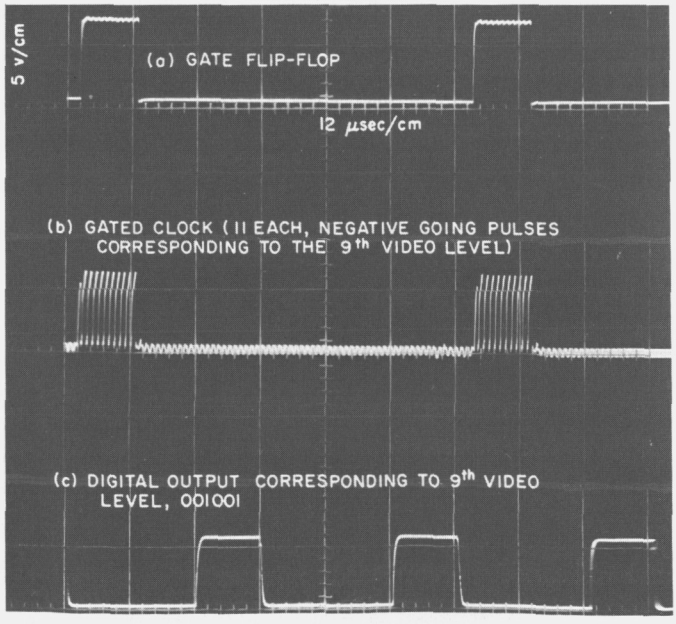

Fig. 59. Gate flip-flop response to gated clock pulses

CONFIDENTIAL

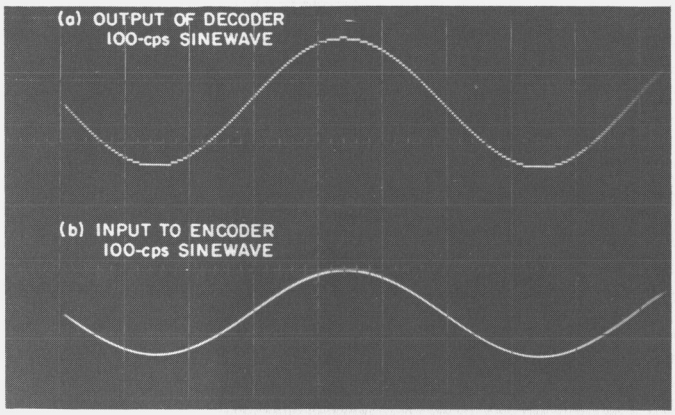

Fig. 60. Encoder–decoder response to 100-cps sinewave

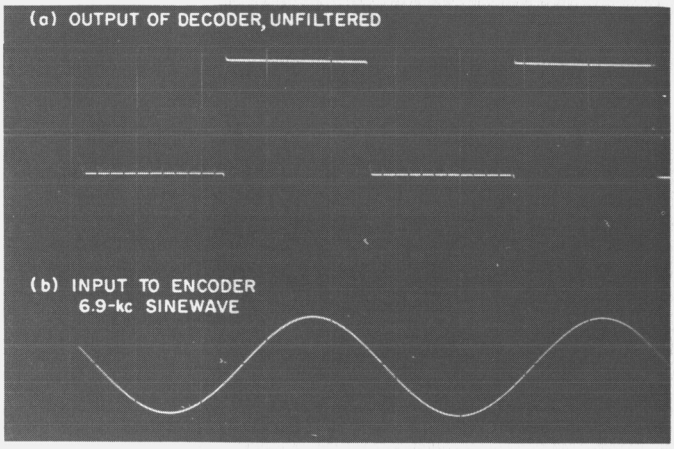

Fig. 61. Encoder–decoder response to 6.9-kc sinewave

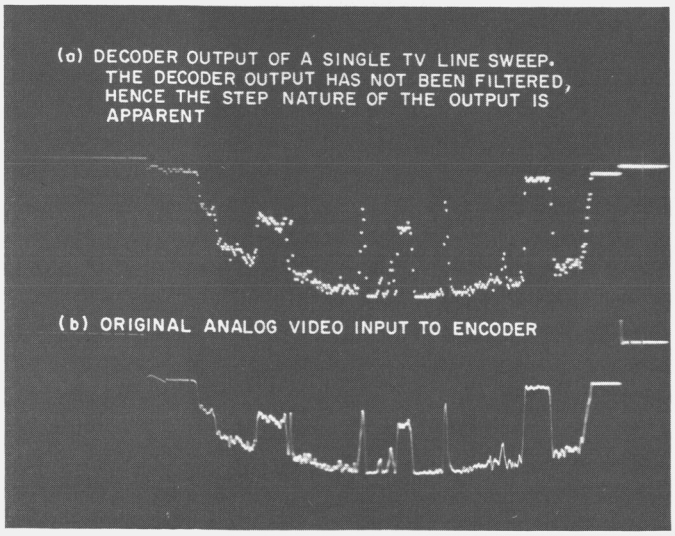

Fig. 62. Encoder–decoder output of typical single TV line sweep

controlled TV camera-tube has irrefutable advantages. Hence, a considerable effort is justified in optimizing the electrostatic camera-tube performance. One of the reasons for magnetic control becoming the *modus operandi* for industry-wide TV cameras is that with electrostatic operation a problem area arises with the scanning beam. The scanning beam in a camera-tube is used to interrogate the photo-charge image for producing the desired electrical output signal. In the case of the vidicon, the charge pattern created on the photoconductive target surface is neutralized by low-velocity electrons abstracted from the scanning beam after deceleration at the mesh electrode. The output signal is then taken directly from the target terminal. If any incidental perturbations are created in the scanning beam during its passage from the cathode the output signal will be directly affected with corresponding picture degradation. An electrostatic tube is particularly sensitive to this problem, as the beam must proceed through a plurality of control electrodes. Hence, two factors emerge for successful electrostatic operation: (1) the electrodes in the tube must be accurately assembled, and (2) the alinement of the electrical fields within these electrodes must be accurately controlled. Use of the deflectron scanning principle in which the x and y planes are scanned simultaneously, utilizing a printed circuit deflection assembly as with the General Electrodynamics Corp. tube, is particularly advantageous in this respect.

The slow-scan operation of *Mariner* B presents additional scanning-field alignment problems. The transistorized deflection circuitry, due to the low scanning frequencies, must be directly coupled to the deflection plates that are required to operate at the high-voltage accelerator potential. As potential gradients between electrodes give rise to undesired defocusing fields, the mean deflection potential must also be accurately centered in order to minimize potential variations between the scanning electrodes and the accelerator electrode. Further alinement problems arise in relating the scan to the black-level stripe deposited on the target. The required twisting to align the scan with the stripe can only be accomplished in an electrostatic tube with an electrical-bridge network. This has, however, a tendency to cause astigmatism in the plane of the image. These alignment problems are in addition to the usual electro-optical alinement required with all TV scanning tubes.

A clean picture with the ability to resolve gray shades is related to the electro-optical characteristics of the photosensitive area. Uniformity of the electrical signal on the photoconductive area with even illumination is dependent on a number of factors. Nonorthogonality of the mesh-

controlled electron-field due to the scanning process, or lateral leakage, produces a charge profile on the signal plate that is highest in the center of the picture and decreases towards the edges. This charge profile becomes superimposed on the target discharge characteristics as the beam slowly traverses the frame. In addition, possible secondary emission from the target may disturb the charge pattern and create regions of higher brightness than that obtained by the primary photoconductive process. An aspect of secondary emission is that the number of secondary electrons may be several times greater than the number of primary electrons even for the low impact energies of a few electron volts that are present with the vidicon. While these factors are essentially problems of tube design, preferred adjustment of circuit parameters can optimize picture quality for a given tube. *Mariner* B is in a particularly fortunate position in that the low video bandwidth permits an extra high-gain amplifier with a correspondingly reduced target potential.

5. Electrostatic Vidicon Evaluation Tests

An evaluation of electrostatic vidicon operation using a provisional *Ranger*-type vidicon has proceeded with the testing of the 400-line TV camera system of *Mariner* B. Satisfactory picture quality of 250-line resolution (limited at this time by the tube focus) has been obtained with a noteworthy freedom from background noise, either from spurious target signals or undesired electrical signal leakage. Operation of the electrostatic vidicon from the electronic control package over a 12-ft cable has proved completely satisfactory.

The measured transfer characteristics of the vidicon transducer, including the video amplifiers, is shown in Fig. 63, which relates high-light illumination to S/N ratio. This corresponds quite closely to the estimated characteristics (*SPS 37-14*). Clear pictures, 26-db S/N ratio, are obtained at the 0.0075-ft-candle/sec illumination level. Figure 64 illustrates the decay characteristics of the ASOS surface. Based on the assumption that the phenomena is related to an RC network, a time constant may be affixed in terms of the exponential. The time constant for this tube is seen to be 38 sec, so that during the 14.8-sec vertical scan the charge may be expected to decrease by 33%. The charge profile for even illumination is illustrated in Fig. 65 for the x-scan direction. A 30% decrease in charge is to be noted toward the edges. The y-scan direction may be expected to have similar characteristics.

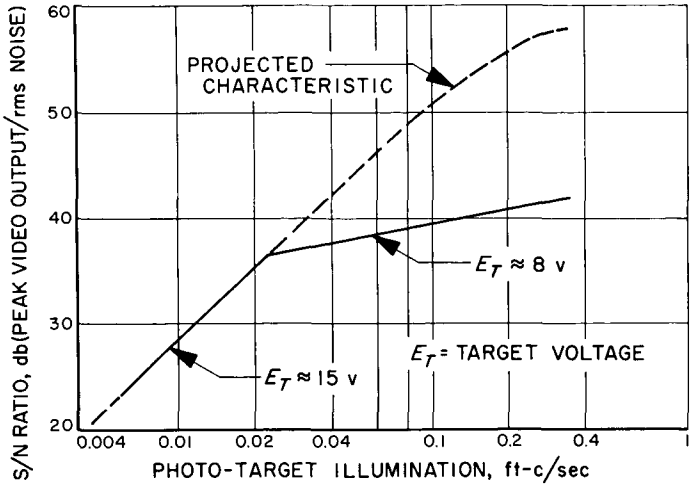

Fig. 63. Measured S/N ratio for *Mariner* developmental camera with gain and target voltage optimized for best picture quality

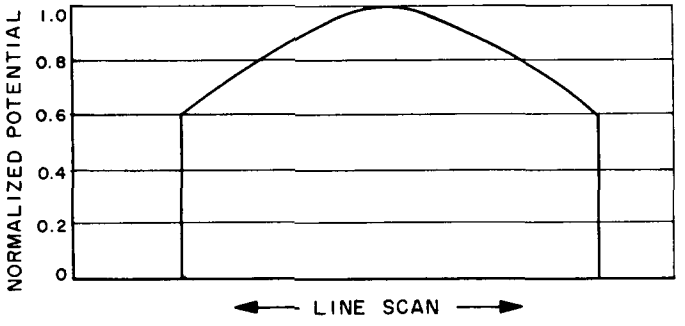

Fig. 64. Charge profile of ASOS vidicon target in x direction

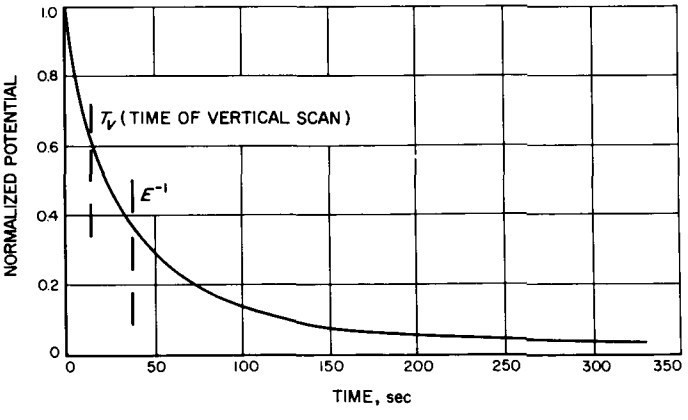

Fig. 65. Charge decay characteristics of ASOS vidicon target

The stability of the electronic circuitry for controlling the vidicon has been evaluated versus temperature and operating potentials. Due to the multiplicity of supply potentials required by an electrostatic tube, electrical stability is most conveniently evaluated in terms of the line input to the power supply. As an intermediary meas-

ure a slightly modified *Ranger* power supply has been used to operate the camera circuitry. In this supply, the critical potentials are electronically regulated, less critical potentials are zener controlled with the remaining potentials of less significance uncontrolled. Observations were made of picture quality and geometrical stability in relation to temperature and power-line changes. No degradation in picture quality was observed with the electronic circuitry ambient ranging from −30 to 65° C. It should be noted that during these tests, the vidicon tube assembly remained at room temperature. No change in picture quality was observed for a 20% drop in the line voltage (the regulated 2400-cps converter did not permit a line voltage increase). The greatest change in picture geometry was a 20% increase in the vertical scan at 65°C. However, as the *Mariner* B camera power supply regulation is expected to be 0.5% or better, against all expected changes, the over-all picture stability should be correspondingly stable.

Misalignment of the scan with the black-level stripe without electrical compensation was measured to be 3.5 deg. This might be compensated by a corresponding twist of the stripe or the electrodes. Even if some residual bridge compensation were still then required, astigmatism would be reduced to negligible proportions.

During the next period in particular, picture quality will be evaluated in relation to the ambient temperature of the vidicon tube assembly. Steps will also be taken to consolidate the position of the electrostatic tube with respect to environment and circuitry, not only for *Mariner* B, but as a useful transducer for planetary photography.

6. Plasma Instrument

The advanced design plasma instrument for *Mariner* B is described in *SPS 37-14*. Its operation is sequenced by a programmer presently being developed to satisfy the more complex requirements of the new design. Although improved in several respects, the basic circuitry of the new programmer remains similar to that found in earlier JPL plasma instruments. The logic functions, however, have been greatly extended to encompass the new requirements.

a. Deflection voltage. Deflection plate voltage is generated by the sweep amplifier in proportion to the current injected at the sweep amplifier input. The programmer injects 16 discrete levels of current, closes a relay contact to change the sweep amplifier's gain, and again injects the 16 levels for a total of 32 discrete voltages at the amplifier output. As seen in Fig. 66, this section of the programmer consists of a four-stage recirculating binary counter coupled to a 4×16 "energy level" matrix. A fifth stage of the counter drives the gain-changing reed relay. A reset or current calibrate pulse sets all states to zero to provide a periodic reference.

To measure electrons, another flip-flop, controlled by a polarity command pulse from the DAS, reverses the polarity of the voltage applied to the deflection plates by use of a special high-voltage reed switch.

b. Cup selection. Any one of seven cups is connected to the electrometer amplifier input by the closure of a corresponding high-impedance relay. A second set of relays remains closed, thereby grounding all idle cups and preventing a build-up of high voltage across their capacitances to ground. A three-stage counter and 3×7 matrix are required for relay control.

c. Electrometer current calibration. As discussed in *SPS 37-14*, one improvement in the new plasma instrument is the addition of an automatic-scale-factor, or linear range compression device, which enables the electrometer amplifier to measure seven decades of current with three linear ranges. To check the electrometer calibration and automatic scaling, one of three standard levels of current is injected at the electrometer amplifier input. A two-stage counter and a 2×3 matrix act to assure that successive calibrations will always be in the middle of an adjacent range. High-impedance relays select resistors to provide the calibration currents, whose levels are known as accurately as the values of the resistors. All cups are disconnected from the amplifier input during current calibrations, when a flip-flop inhibits the cup selection matrix.

d. Relay development. A small reed relay is under development and will have an operating coil power of 10 mw, a minimum open contact resistance of 10^{15} ohms, and a diameter of less than 0.4 in. The coils and switches required to achieve this performance are state-of-the-art devices. The coils, for example, must be bobbinless, optimized in diameter, and wet-wound with epoxy into a special form.

A double-throw reed switch will be utilized for the high-voltage polarity reversing relay, but for low-level circuits, the small single-throw relays prove much superior in power, weight, and size, even though twice

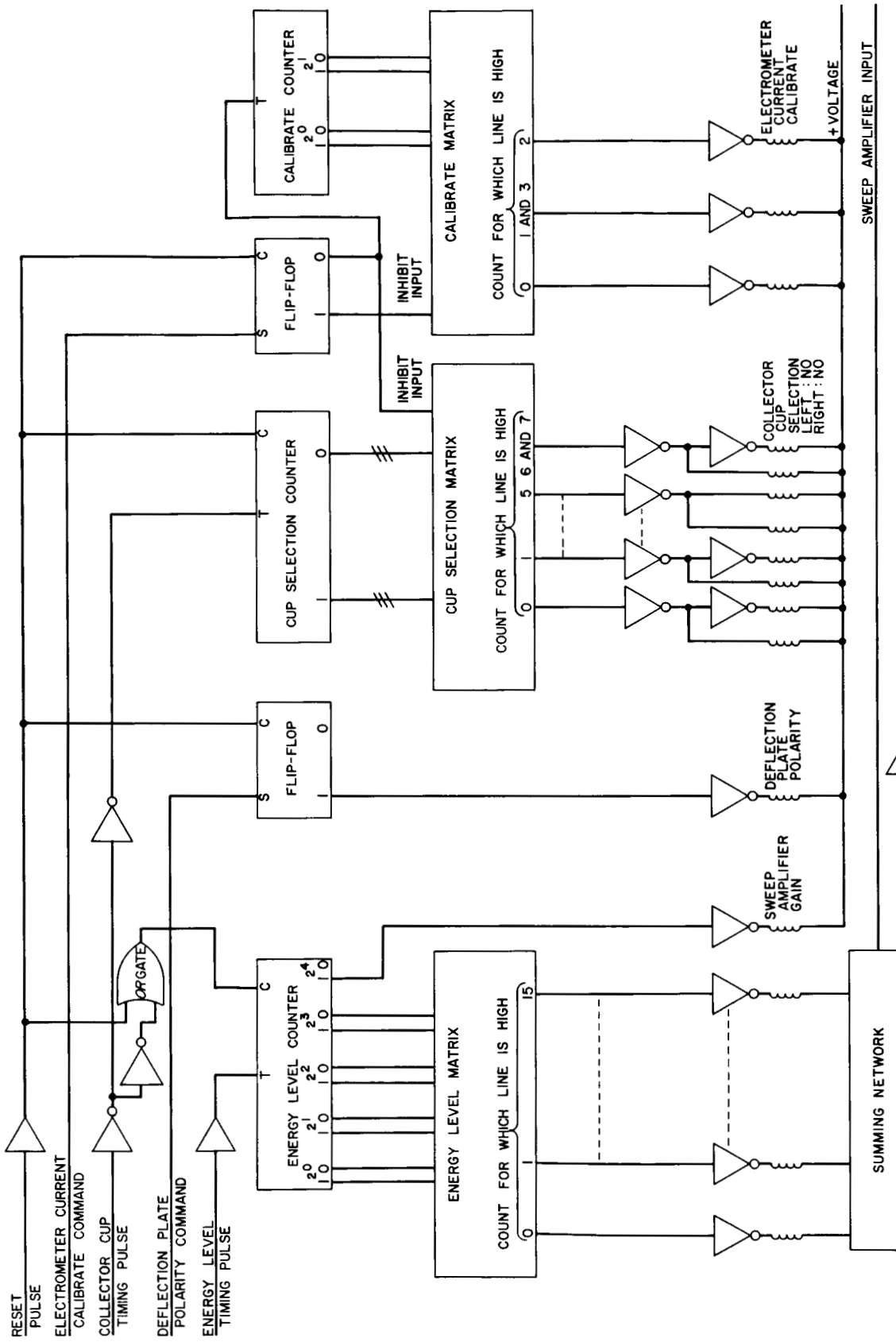

Fig. 66. Plasma experiment programmer block diagram

as many must be used when double-throw configuration is required.

For sweep amplifier gain control, a high-voltage single-throw switch is also being developed.

e. Development status. The programmer breadboard is undergoing temperature tests, and the small relay design is nearly complete. A welded cord-wood module containing all three matrices is being fabricated by Wems, Inc. for inclusion in the programmer of the prototype solar plasma instrument.

F. Propulsion

The primary function of the *Mariner*-B post-injection propulsion system is to remove or reduce injection dispersion errors so that planetary miss parameters on the order of 2000 km (1 σ) after mid-course corrections and 320 km (1 σ) after approach corrections can be realized. This function is performed during the four possible mid-course corrections and the three possible approach corrections during which the spacecraft is directed to turn to a prescribed attitude in space and impart a corrective impulse via the post-injection propulsion system.

A secondary function of the post-injection propulsion system is to provide a post-separation adjustment of the spacecraft trajectory when an entry capsule without propulsion is carried and a bus deflection is desired.

A description of the *Mariner*-B post-injection propulsion system is presented in *SPS 37-15*.

1. Development Program

Since the last report period, work has continued on preliminary design layouts of the propulsion system. The layouts have resulted in finalizing the spacecraft propulsion system interface, the type of structure to be used for the propulsion system, and the method of attaching the propulsion system tankage to the structure. A satisfactory packaging arrangement for the propulsion system components has been completed.

Prototype regulators, check valves, and delay valves have been fabricated. These components are currently undergoing evaluation testing to ensure the adequacy of the design. The design of an eight-start propellant-valve/oxidizer-start-slug combination has been completed and parts are being fabricated. Upon the successful completion of some preliminary component evaluation tests, prototype components will be assembled to form a prototype propulsion system. Water-pumping tests and hot-engine firing will be conducted with the system.

Fabrication has been completed on a riveted prototype structure and finish machining is currently in process on a welded prototype structure. The two structures were fabricated to ascertain the relative structural, dimensional, and fabrication merits of the two fabrication techniques. The fabrication techniques have been compared, and it has been decided that a riveted structure will be used in the flight design of the propulsion system.

Proposals for the design and fabrication of the solenoid control valve have been received from vendors and evaluated. The results of the proposal evaluation led to giving a contract to Whitaker Controls for the design and fabrication of a prototype solenoid valve to be test-evaluated by JPL. A JPL-designed solenoid valve will also be evaluated for possible use in the propulsion system.

Ranger, *Mariner* R, and *Mariner* A post-injection propulsion systems have all had approximately 100% more high-pressure-nitrogen-reservoir volume than was required for mission completion. This excess capacity was provided because neither the leakage loss nor the efficiency of a gas-pressurization system, in pumping propellant, was well established. Storage tests and improvements in seal design have improved definition of leakage loss, and an experimental program was undertaken to determine accurately the expulsion efficiency of a gas-pressurization system in a typical post-injection propulsion system. It has been the practice at JPL to present the results of gas-pressurized-propellant-tank expulsion tests in terms of the dimensionless parameter γ'. This parameter is actually an inverse pumping efficiency parameter and is defined as:

$$\gamma' \equiv \frac{V_R (P_i - P_f) - V_U (P_R - P_U)}{V_P P_R}$$

where V_R is the volume of the high-pressure-gas reservoir, P_i and P_f are the initial and final pressures in the

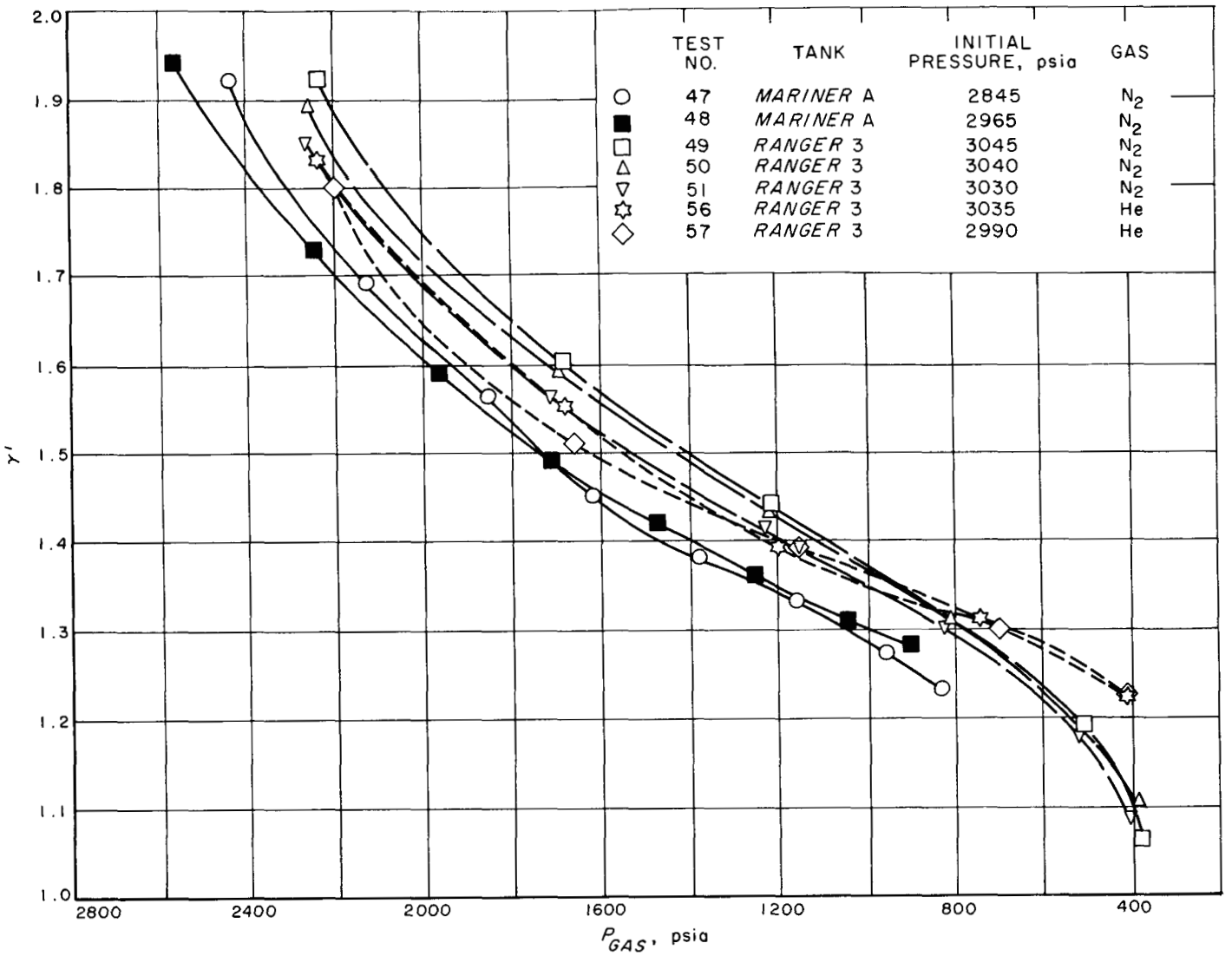

Fig. 67. γ' versus nitrogen tank pressure

high-pressure-gas reservoir, V_U is the initial propellant-tank-ullage volume, P_R is the regulated propellant tank pressure at which the propellant is expelled, P_U is the initial pressure in the propellant tank, and V_P is the volume of propellant expelled. The test system consisted of a *Mariner* A flight-type propellant tank, a *Ranger* or *Mariner* A flight-type nitrogen sphere, a *Mariner* A pressure regulator, and "test" solenoid valves to initiate and terminate gas and propellant flow. An orifice was used in the propellant line to simulate the rocket-engine pressure drop. Water was pumped in lieu of hydrazine. The pumping efficiency of helium, as well as nitrogen gas, was evaluated. The γ' values determined were 1.10 for nitrogen and 1.22 for helium, for complete "blow-downs" (3000 psig initial to 400 psig final, high-pressure-gas pressures). Figure 67 is a plot of the results of the tests from which the values were computed. To develop the curves γ' was calculated for time intervals of 0 to 20 sec, 0 to 40 sec, 0 to 60 sec, etc., (zero time denotes the start of the expulsion). The explanation of the continuous decline in γ' as the expulsion proceeds is as follows: The temperature of the gas in the sphere, and of that leaving the sphere, is continually falling. The temperature of the containing surfaces falls less rapidly, and the difference between the temperature of the walls and the gas bulk temperature increases as the test proceeds. This causes a continual increase in the heat flux to the gas and a decrease in γ' In Fig. 67, the two curves (tests 47 and 48) determined using the *Mariner* A nitrogen reservoir indicate that the greater heat capacity of the shell of the

larger tank yielded slightly lower γ', at comparable pressures, than the smaller *Ranger* nitrogen reservoir (tests 49 to 51). The *Ranger* nitrogen reservoir was used with the *Mariner A* propellant tank because this smaller reservoir (half the volume of the *Mariner A* nitrogen reservoir) sustained a greater pressure drop in emptying the propellant tank, thus extending γ' data to lower pressures than could be attained using the *Mariner* A reservoir.

The weights of the gas-pressurization system for *Mariner* B, for both nitrogen and helium, are shown below.

Gas	γ'	Reservoir weight, lb	Gas weight, lb	Total weight, lb
N_2	1.10	7.78	5.19	12.97
He	1.22	8.54	0.82	9.36

Nitrogen was selected over helium, despite the 3.6-lb weight penalty, for the *Mariner* B post-injection propulsion system because it has a considerably lower rate of leakage loss.

Although the *Mariner*-A program was canceled, a desert storage test of type-approval system No. 2 (described in *SPS 37-11*) was undertaken. The length of the storage period was increased from 4 to 9 months so that storage data applicable to the *Mariner* B Project could be obtained.

Shortly after placing the propulsion system in storage at the Edwards Test Station, a continuous rise in fuel-tank pressure was noted. Calculations had shown that the pressure rise was not due to temperature increase alone, but was apparently a result of slow hydrazine decomposition in the fuel system. A month and a half after the initial storage date, the fuel tank pressure increased suddenly from 350 to 380 psia (pressure at the start of storage was 310 psia). Subsequently, the fuel tank pressure was vented down to 270 psia, after which it remained at this value for the duration of the storage test. It is not known why the pressure in the fuel tank rose constantly during the initial portions of the storage period and then remained constant unless contamination in the fuel tank caused some initial hydrazine decomposition. It was further noted, upon reduction of the data, that the nitrogen system pressure was dropping at the rate of 180 psi a month. This leak was later found to be due to a faulty seal on a special ground-support-equipment nitrogen fill-valve.

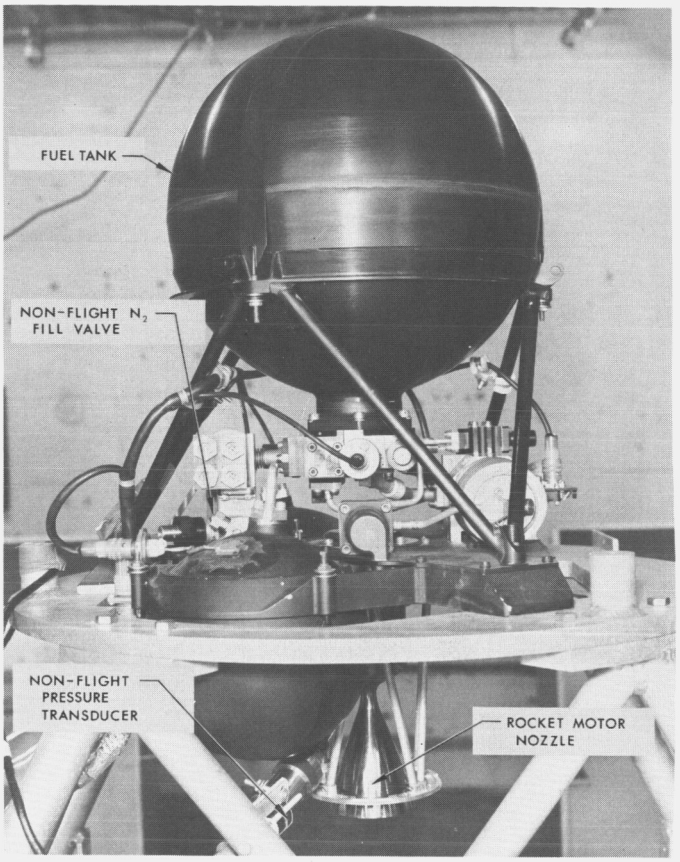

Fig. 68. *Mariner* A mid-course propulsion system prior to restart test

After a storage period of 233 days, the *Mariner*-A mid-course propulsion system was brought back to test cell J at JPL in order to perform system restart tests. A leak test of all gas pressure seals revealed no leakage other than the aforementioned leakage on a nonflight fitting. For the restart tests, no adjustments were made to the propulsion system other than connecting the electrical wiring for energizing the solenoid valve and explosive valves. Figure 68 shows the mid-course propulsion system mounted on its firing stand with a heavy weight (nonflight) chamber pressure transducer attached to the rocket engine. A successful restart test was made with all valving working in a normal manner. The nitrogen delay valve successfully delayed engine start until the tank pressure was at approximately operating level. A second restart of the propulsion system was successfully made 1 hr after the first restart. Each test was of 30-sec duration.

At completion of the two restart tests, the mid-course propulsion system was dismantled and inspected. Fig-

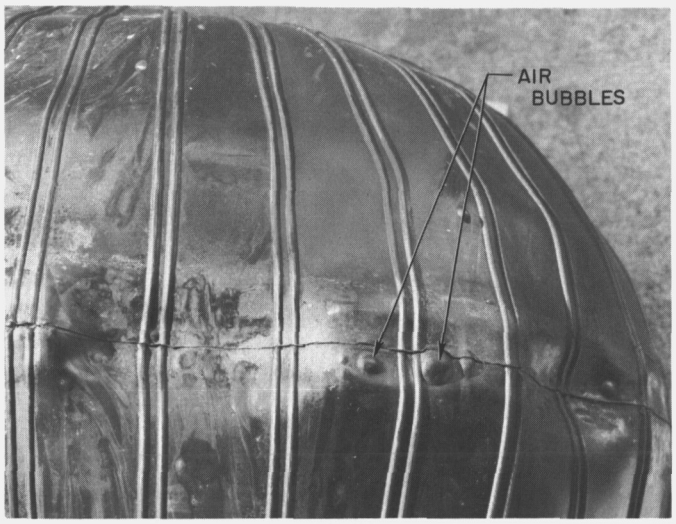

Fig. 69. Fuel tank bladder after storage test

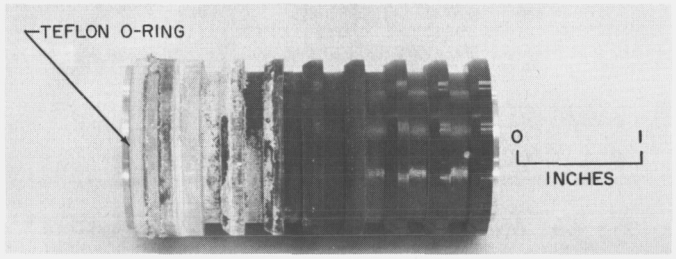

Fig. 70. Oxidizer piston after storage test

ure 69 shows the fuel tank bladder after it was removed from the fuel tank. The blisters on the outside of the tank are thought to be due to air entrapped in the rubber during fabrication and increased in size during the storage period due to osmotic pressure. Approximately 1.5 ml of hydrazine was found in the prepressurization ullage space between the bladder and the tank. This hydrazine apparently permeated through the bladder during the storage test, as a leak test of the bladder mounted on its manifold revealed no leakage. Further disassembly of the system showed good long-term storage capability of the propulsion components, with the exception of aluminum nitrate salts having formed around the oxidizer piston of the propellant valve as shown in Fig. 70. The Teflon O-ring had taken very little permanent set and was still working normally. However, nitrogen tetroxide had permeated through the Teflon O-ring and destroyed the Silastic backup O-ring and formed the aluminum nitrate salts. Although the salt formation did not affect the operation of the propellant valve during the restart tests, it is considered detrimental to the reliability of the valve, and a metallic-type seal is being investigated for use on the valve in the *Mariner*-B program. The pressure and fuel transducers were found to be in good condition and have been turned over to the instrumentation group for their examination.

In general, the results of the storage test were very encouraging and demonstrated the storability of the propulsion system for prolonged periods of time. Considerable storage data applicable to the design of the *Mariner*-B post-injection propulsion system have been obtained.

G. Supporting Activities

1. Optimizing the Aft Configuration of the Mariner B Entry Capsule

It is anticipated that the *Mariner* B entry capsule will passively enter the Martian atmosphere and could assume any attitude during the initial phase of entry. One of the requirements for ensuring that the forward face of the capsule be nominally forward through the heating phase of the entry is that the base configuration must cause the capsule to be statically unstable in the rearward direction. In an endeavor to obtain the optimum aft body configuration which will accomplish this goal, a joint theoretical and experimental study was initiated. The first phase of this work is being reported.

The cross-hatched portion of Fig. 71 depicts the forward section of the entry body used as the foundation for this study (the center-of-gravity was 0.417 diameters aft of the nose). Several families of aft configurations were considered: cones, spherical caps, spherical cap and cones, and truncated cones. For the spherical cap and cones, and truncated cones, the base angle δ was kept at 40 deg. Representative members of each family were chosen using X/Y (ratio of tail distance to radius) as the parameter. Theoretical aerodynamic coefficients versus angle-of-attack were obtained by means of the unmodified Newtonian impact theory. To ensure overturning a condition of instability, $C_{m\alpha} > 0$, is required. The Newtonian pitching moment slopes ($C_{m\alpha}$ per deg) taken about zero angle-of-attack are presented on the plot of Fig. 71.

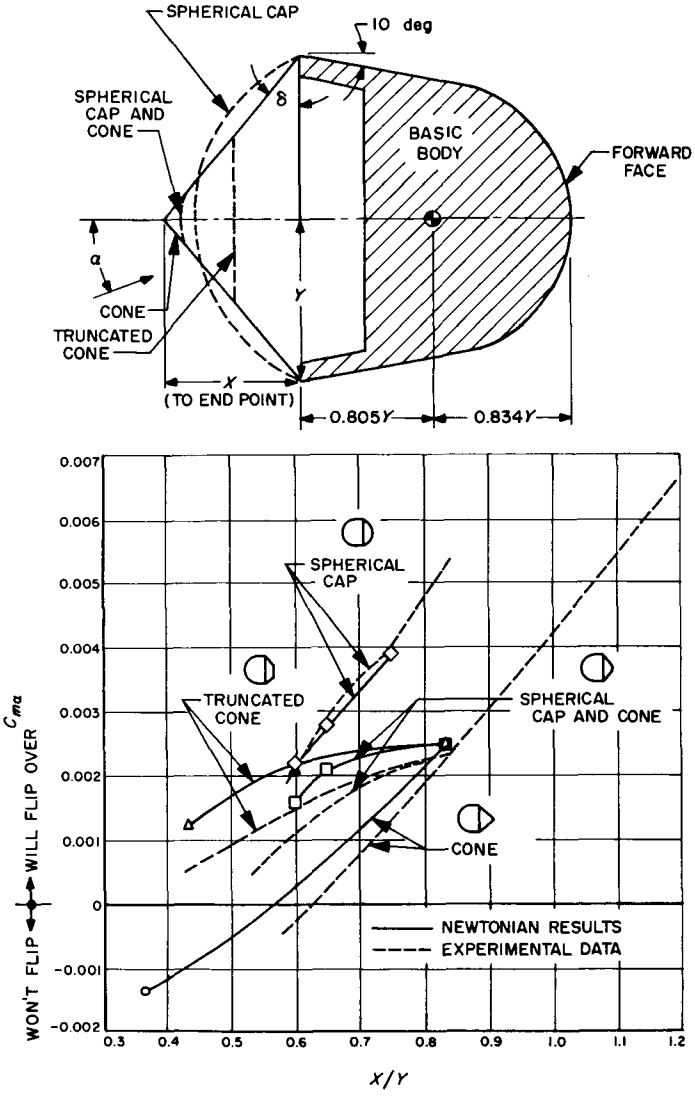

Fig. 71. Pitching slopes for various aft body configurations versus packaging parameter (X/Y)

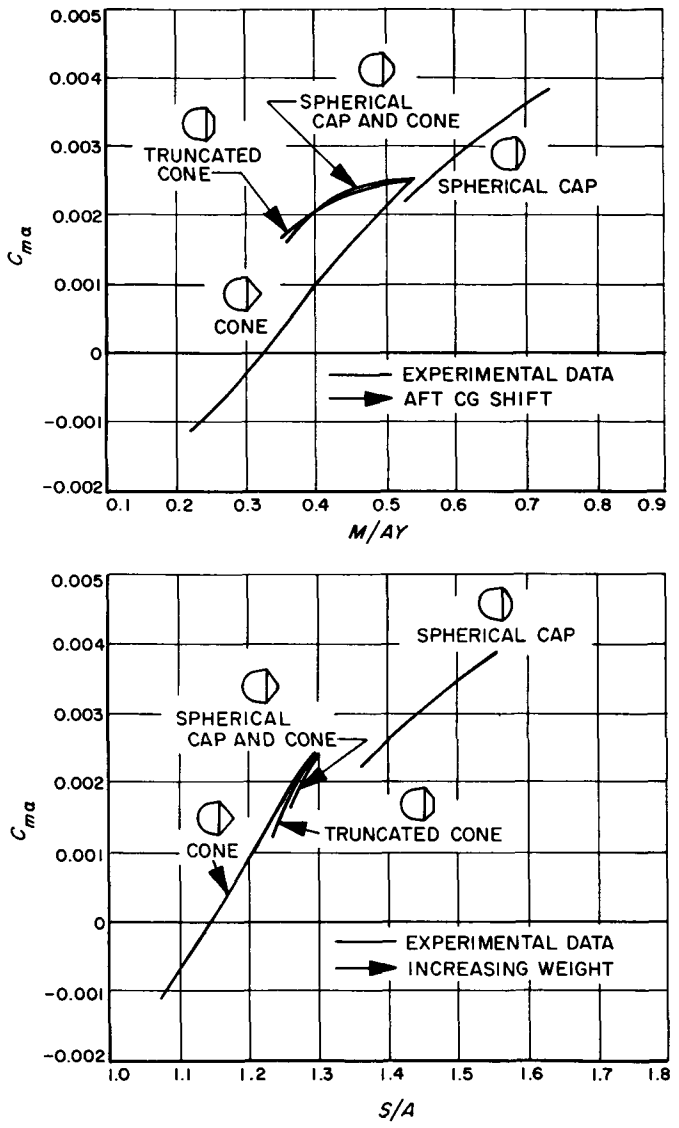

Fig. 72. Pitching slopes versus weight parameter (S/A) and cg shift parameter (M/AY)

Using the Newtonian results as a guide, several models of the previously described configurations were tested in the supersonic wind tunnel at Mach 4.54 and Reynolds numbers ranging from 0.03×10^6/in. to 0.32×10^6/in. These results are included on the plot of Fig. 71. Previous tests on blunt bodies of low fineness ratios in both the supersonic and hypersonic wind tunnels indicate that the aerodynamic coefficients were essentially invariant with Mach numbers above 4. Furthermore, this series of tests at the Reynolds numbers stated, showed negligible variations in aerodynamic coefficients (2 to 3%).

The location of the center-of-pressure along the body centerline was relatively invariant for the rearward angle-of-attack range tested, 0 to 50 deg. Also the experimental pitching moment slopes were quite constant for the range tested. The Newtonian pitching moment slopes, however, became more positive at about 20- to 25-deg angle-of-attack for most of the shapes investigated.

In determining the optimum aft-capsule configuration, three important criteria, in addition to the overturning moment, became apparent: geometric size (packaging considerations), weight, and location of the center-of-gravity. The parameter X/Y became significant when considering packaging criterion. A constant X/Y value indicates capsules of the same total length. As an example, if a maximum X/Y value of 0.7 is allocated for

the capsule, Figure 71 indicates that the cone is least desirable, the spherical cap and cone and truncated cone are about the same, and the spherical cap is by far the most desirable based on the magnitude of the overturning moment. It should be remembered, however, that the spherical cap and cone, and truncated cone data are for base angles of δ equal to 40 deg.

Appropriate parametric indicators were devised for investigating weight and capsule center-of-gravity location by assuming that the aft portion of the body is composed of a uniformly dense thin shell (weight is proportional to the surface area). The parameter S/A, ratio of aft surface area to maximum cross-sectional area, indicates the weight contribution of the aft section. M/AY, the ratio of the afterbody surface area moment (about $X = 0$) to the product of maximum cross-sectional area and maximum radius, is a measure of the rearward shifting of the center-of-gravity due to the weight of the afterbody. Plots of these parameters versus the pitching moment slopes are presented in Fig. 72. Both of these plots indicate that the spherical cap is least desirable while the rank of desirability of the other three shapes is less definite for the smaller overturning moments.

Upon weighing the desirability of the shapes investigated, in light of this study, it appears that the truncated cone is probably the best compromise shape tested with the spherical cap and cone being a second possibility. The high weight contribution and adverse center-of-gravity shift of the spherical cap, and the poor packaging characteristics of the cone make both of these shapes poorer choices. It should be noted, however, that this initial study did not consider either the fabrication or structural integrity of these shapes, nor did it consider other basic body configurations. These and other considerations must be explored before a final conclusion can be made in regard to an optimum configuration.

2. Plasma Probe Space Simulation Testing

The operation of the *Mariner* B low-energy plasma probe was tested under space thermal conditions in the 6-ft space simulator. A specially designed remote control motorized mounting for the probe permitted the distance between the test specimen and the solar source to be changed during the test. Testing lasted 53 hr. Environment: vacuum, 10^{-5} mm Hg; shroud temperatures -300 to $+72$°F; solar simulation, one carbon arc.

IV. *Voyager* Project

Voyager missions are envisioned to evolve to sophisticated orbiters and landing experiments beginning in 1966 or 1967 using *Saturn* vehicles. Planetary orbiters are a necessary part of the evolution and are a logical step in the development of spacecraft technology. Orbiters are probably required to permit sufficient observation of the planet to know how to proceed with the landing missions. Furthermore, orbiters may well constitute an important step in the actual landing experiments. The emphasis on planetary orbiters, therefore, will be to contribute to the successful accomplishment of the landing objective.

The primary programming effort conducted during this reporting period consisted of the organization of an Advanced Planetary Spacecraft Study Committee whose function is to determine possible mission objectives and design concepts of spacecraft for use on the *Saturn* class of vehicle and of advanced propulsion type of spacecraft. The study is scheduled to continue for several months.

Specific efforts directed to accomplishment of the *Voyager* Project were initiated at the start of FY 62. A synopsis of these efforts follows:

The Systems Division is participating with the technical divisions and the Marshall Space Flight Center in the generation of mission objectives and the preparation of preliminary systems design specifications for interplanetary spacecraft to be used as planetary orbiters and landers and out-of-the-plane-of-the-ecliptic probes using the *Saturn* vehicle as the booster.

The Space Sciences Division is conducting *Voyager* scientific feasibility studies, establishing the feasibility of meteorological, biological, and certain adaptations of geological experiments for the *Voyager*, as well as refining knowledge of the Mars and Venus environments as they affect experiments and spacecraft for these flights.

The Guidance and Control Division is continuing its studies of guidance and control requirements, methods, and techniques for advanced planetary missions, both those currently planned and those that become necessary or desirable as a result of discoveries on early planetary exploration missions that require further exploratory operations. The methods to be used include study of possible mission requirements to deduce the general requirements for guidance and control subsystem performance, evolution of subsystem configurations to accomplish the required tasks, and parametric and error analyses of typical missions and operating situations to determine the ranges or parameters and tolerances required.

The Engineering Mechanics Division is performing *Voyager* spacecraft studies, including analytical investigations of configuration, thermal control, entry and landing dynamics, post-landing and roving techniques, booster compatibility, multiple mission or universal design concepts and compromises, and structural design problems.